Excitation and damping mechanisms of geodesic acoustic modes in tokamaks

Ivan Novikau

ULM 2020

Excitation and damping mechanisms of geodesic acoustic modes in tokamaks

Ivan Novikau

Dissertation zur Erlangung des Doktorgrades
Dr. rer. nat.
an der Fakultät für Naturwissenschaften
der Universität ULM

vorgelegt von
Ivan Novikau
aus Minsk, Republik Belarus

ULM, 2020

Dekan: Prof. Dr. Thorsten Bernhardt
Erstgutachter: apl. Prof. Dr. Emanuele Poli
Zweitgutachter: Prof. Dr. Fedor Jelezko
IPP Betreuer: Dr. Alessandro Biancalani
Tag der mündlichen Prüfung: 06.08.2020

To my family.

Abstract

The tokamak is one of the most promising concepts to produce controlled thermonuclear fusion power. In tokamak configuration, deuterium-tritium fuel heated to high temperatures turns into the plasma state that has to be confined for a sufficiently long time to achieve the condition of the self-sustaining burning plasma. However, small scale instabilities driven by plasma temperature and density gradients cause turbulence, which is responsible for enhanced particle and energy losses in the system. This turbulent transport is considered as one of the main phenomena that degrade the plasma confinement.

Turbulence in tokamaks generates nonlinearly large-scale flows (called zonal flows) that deplete the turbulence level and thus play a fundamental role in turbulence regulation and saturation. As part of this dynamics, an oscillatory counterpart of the zonal flows can arise because of the action of the magnetic field curvature. These oscillations, which can also couple directly to the turbulence, are called the geodesic acoustic modes (GAMs) and are the main subject of this thesis. GAMs can be driven unstable also by an anisotropic energetic particle (EP) population leading to the formation of global radial structures, called EGAMs. The EGAMs might play the role of an intermediate agent between the energetic and thermal species by redistributing the EP energy to the bulk plasma through collisionless wave-particle interaction. In such a way, the EGAMs might contribute to plasma heating. Thus, investigation of EGAM properties, especially in velocity space, is necessary for a precise understanding of the transport phenomena in tokamak plasmas.

In this thesis, we numerically investigate different mechanisms of the GAM damping and excitation such as Landau damping, phase mixing and the mode formation by energetic particles and turbulence. While several aspects of the GAM dynamics can be understood in the frame of a fluid model, a quantitative understanding requires a kinetic approach, which can describe the details of the GAM interaction with the plasma particles in phase space and thus capture, for instance, the effect of resonances. The global gyrokinetic particle-in-cell code ORB5 is used here as the primary numerical tool for this study. As a part of this work, additional relevant code diagnostics are developed, such as a Mode-Particle-Resonance (MPR) technique to explore wave-particle interactions in velocity space. This MPR method is employed to study EGAM dynamics in a magnetic configuration typical of the ASDEX Upgrade (AUG) tokamak, by analysing the influence of different species on the time evolution of the mode. It is shown that electrons, which are often not included in the theoretical analyses, significantly contribute to the damping of (E)GAMs in experimentally relevant AUG plasma systems. Moreover, nonlinear EGAM dynam-

ics without considering the mode interaction with turbulence is investigated here to explore energy transfer by the mode from energetic particles to thermal species, including kinetic electron effects. It is shown that the electron dynamics decreases the EGAM saturation amplitude and consequently reduces the plasma heating by the mode, even though the mode transfers its energy to thermal ions much more than to electrons.

Finally, nonlinear GAM excitation by ion-temperature-gradient driven instabilities is numerically simulated for magnetic configurations reflecting the properties of AUG and of the Tokamak à Configuration Variable (TCV). Formation of continuum and global frequency spectra of the geodesic and GAM-like structures is demonstrated in these computations.

Zusammenfassung

Der Tokamak ist eines der vielversprechendsten Konzepte zur Erzeugung kontrollierter Kernfusion. In der Tokamak-Konfiguration wird der Deuterium-Tritium-Brennstoff auf hohe Temperaturen erhitzt, sodass ein Plasmazustand erreicht wird. Das Plasma muss ausreichend lange eingeschlossen werden, damit der Zustand des selbsttragenden brennenden Plasmas erreicht wird. Plasmatemperatur- und Dichtegradienten führen jedoch zu Mikroinstabilitäten. Diese Mikroinstabilitäten verursachen Turbulenzen, die für erhöhte Partikel- und Energieverluste im System verantwortlich sind. Der turbulente Transport wird als eines der Hauptphänomene angesehen, die den Plasmaeinschluss verschlechtern.

Turbulenzen in Tokamaks erzeugen nichtlinear großskalige Flüsse, die als zonale Strömungen oder *Zonal Flows* bezeichnet werden. Diese Flüsse verringern das Turbulenzniveau und spielen eine grundlegende Rolle bei der Turbulenzregulierung. Ein oszillierendes Gegenstück zu den *Zonal Flows* kann aufgrund der Magnetfeldkrümmung entstehen, und kann auch direkt mit den Turbulenzen interagieren. Diese Oszillationen werden als geodätische akustische Moden (GAM) bezeichnet und sind das Hauptthema dieser Arbeit. GAMs können auch von einer anisotropen energetischen Partikelpopulation (EP) angeregt werden. Die resultierende globale radiale Struktur heißt EGAM. Die EGAM kann die Rolle eines Mediators zwischen den energetischen und thermischen Spezies spielen. Dieser Moden verteilt die EP-Energie durch kollisionsfreie Welle-Partikel-Wechselwirkung auf das Bulk-Plasma. Auf diese Weise können die EGAMs zur Plasmaheizung beitragen. Daher ist die Untersuchung der EGAM-Eigenschaften, insbesondere im Geschwindigkeitsraum, erforderlich, um die Transportphänomene im Tokamak zu verstehen.

In der vorliegenden Arbeit werden verschiedene Mechanismen der GAM-Dämpfung und GAM-Anregung wie Landau-Dämpfung, Phasenmischung und Modenbildung durch energetische Partikel und Turbulenzen numerisch untersucht. Einige Aspekte der GAM-Dynamik können im Rahmen eines Fluidmodells verstanden werden. Ein quantitatives Verständnis erfordert jedoch einen kinetischen Ansatz. Dieser Ansatz kann die Details der GAM-Wechselwirkung mit den Plasmapartikeln im Phasenraum beschreiben und so beispielsweise den Effekt von Resonanzen erfassen. Der globale gyrokinetische *Particle-In-Cell* Code ORB5 wird hier als primäres numerisches Werkzeug für diese Untersuchung verwendet. Im Rahmen dieser Arbeit werden zusätzliche relevante Codediagnosen entwickelt, beispielsweise eine Moden-Partikel-Resonanz (MPR)-Technik. Sie wird verwendet, um Wellen-Teilchen-Wechselwirkungen im Geschwindigkeitsraum zu untersuchen und um den Einfluss verschiedener Spezies auf die Zeitentwicklung der Moden zu analysieren. Die MPR-Methode wird verwendet, um

die EGAM-Dynamik in einer für das ASDEX Upgrade (AUG)-Tokamak typischen magnetischen Konfiguration zu untersuchen. Es wird gezeigt, dass Elektronen, die in den theoretischen Analysen häufig nicht enthalten sind, wesentlich zur (E)GAM-Dämpfung in experimentell relevanten AUG-Plasmasystemen beitragen. Die nichtlineare EGAM-Dynamik ohne Berücksichtigung der Wechselwirkung der Moden mit Turbulenzen wird ebenfalls analysiert. Insbesondere wird die Energieübertragung durch die Moden von energetischen Partikeln auf thermische Spezies einschließlich kinetischer Elektroneneffekte untersucht. Es zeigt sich, dass die Mode seine Energie viel mehr auf thermische Ionen als auf Elektronen überträgt. Trotzdem verringert die Elektronendynamik die EGAM-Sättigungsamplitude erheblich und folglich die Plasmaheizung durch die Mode.

Schließlich wird die nichtlineare GAM-Anregung durch Ionen-Temperaturgradienten-Instabilitäten für magnetische Konfigurationen numerisch simuliert, die Eigenschaften von AUG und vom *Tokamak à Configuration Variable* (TCV) widerspiegeln. Die Bildung von Kontinuums- und globalen Frequenzspektren der GAM-ähnlichen Strukturen wird in diesen Berechnungen demonstriert.

Acronyms

AE	Adiabatic Electrons (or an ES simulation with adiabatic electrons)
ASDEX Upgrade	Axially Symmetric Divertor Experiment, a divertor tokamak at the Max Planck Institute of Plasma Physics, Garching near Munich
AUG	ASDEX Upgrade
CHEASE	name of an ideal MHD equilibrium code
DW	Drift Wave
EGAM	Energetic particle driven Geodesic Acoustic Mode
EM	Electromagnetic
EP	Energetic Particle
ES	Electrostatic
GAM	Geodesic Acoustic Mode
GENE	name of an Eulerian GK code
GK	GyroKinetic
ITG	Ion Temperature Gradient instability
KE	drift-Kinetic Electrons (or an EM simulation with drift-kinetic electrons)
MPR	Mode-Particle-Resonance (diagnostic)
NL	Non-Linear
ORB5	name of a particle-in-cell gyrokinetic code mostly used in this thesis
PIC	Particle-In-Cell
TCV	Tokamak à Configuration Variable, tokamak in Swiss Plasma Center of the École Polytechnique Fédérale de Lausanne

ZF or ZFZF	zero-frequency (stationary) Zonal Flow
zonal	flux-surface averaged
ZS	Zonal Structure (ZF or/and GAM)

List of symbols

e	Absolute electron charge
$Z_{sp}e$	Species charge ($Z_e = -1$)
c	Speed of light
m_{sp}	Species mass
T_{sp}	Species temperature
$v_{T,sp} \equiv v_{th,sp} = u_{th,sp} \cdot 2^{-0.5} = \sqrt{T_{sp}/m_{sp}}$	Species thermal temperature
$c_s = (T_e/m_i)^{0.5}$	Sound speed
a_0	Minor radius of a tokamak
R_0	Major radius of a tokamak
B_0	Magnetic field value at the magnetic axis
q	Safety factor
κ	Plasma elongation
$\varepsilon = a_0/R_0$	Inverse aspect ratio
$\omega_{c,sp} = Z_{sp}eB_0/(m_{sp}c)$	Species cyclotron frequency
$\omega_s = c_s/R_0$	Sound frequency
$\rho_{sp} = \sqrt{2}v_{th,sp}/\omega_{c,sp}$	Species Larmor radius
$\rho_s = c_s/\omega_{ci}$	Sound Larmor radius
$\rho^* = \rho_s/a$	Inverse normalised minor radius
$L_x = 2/\rho^*$	Normalised size of a plasma system
ψ	Poloidal flux coordinate
$s = \sqrt{\psi/\psi_{edge}}$	Standard ORB5 radial coordinate
$\tau_e = 1/\tau_i = T_e/T_i$	Electron-ion temperature ratio
$\langle n_e \rangle$	Volume-averaged electron density
$\beta_e = 4\pi\langle n_e \rangle T_e/B_0^2$	Ratio of electron plasma and magnetic pressures
$\mu_{sp} = (m_{sp}v_{\perp,sp}^2)/(2B)$	Species magnetic moment

Contents

Contents **xiii**

1 Introduction **1**
1.1 Nuclear fusion 1
1.2 The tokamak 3
1.3 Plasma confinement and the geodesic acoustic mode (GAM) 6
1.4 GAM damping and EGAM excitation 13
1.5 Drift instabilities and the excitation of zonal structures 16
1.6 Contribution and outline of the thesis 19

2 Numerical gyrokinetic model **23**
2.1 Hamiltonian formulation 24
2.2 The Particle-In-Cell (PIC) code 29
2.3 Power balance 33

3 Gyrokinetic theory of GAMs **37**
3.1 Gyrokinetic equation 37
3.2 GAM dispersion relation 41

4 GAM damping **49**
4.1 Landau damping 49
4.2 Phase mixing 55
4.3 Collisional damping 59
4.4 GAM linear frequency and damping spectra in ASDEX Upgrade . . . 60
4.5 Chapter summary 61

5 Mode-Particle-Resonance diagnostic **63**
5.1 Implementation 63
5.2 Post-processing: application to a simplified GAM case 65

5.3 Analytical verification 69
5.4 Chapter summary 71

6 Linear dynamics of Energetic particle driven GAMs 73
6.1 ASDEX Upgrade plasma configuration 73
6.2 Role of the wave-particle interaction in the EGAM linear dynamics . 76
6.3 Comparison with GENE 81
6.4 Chapter summary 83

7 Nonlinear EGAM dynamics in ASDEX Upgrade 85
7.1 Plasma heating by EGAMs 87
7.2 EGAM frequency chirping 96
7.3 Some remarks on EGAMs in ITER 98
7.4 Chapter summary 101

8 Nonlinear GAM excitation by turbulence 103
8.1 Global frequency spectrum of a GAM-like zonal signal in TCV magnetic configuration 104
8.2 Staircase GAM frequency spectrum in the AUG discharge 109
8.3 Discussion and chapter summary 114

9 Conclusions and outlook 117

A Evaluation of the Plasma Dispersion Function 121

Bibliography 123

Acknowledgement 137

Declaration 139

List of publications 141

Chapter 1

Introduction

1.1 Nuclear fusion

Nowadays, a significant effort is put into the development of a new type of nuclear reactors to produce energy from thermonuclear fusion reactions. The basic idea that lies behind this process can be explained in the following way. When a nucleus of *deuterium* and one of *tritium* approach at a distance where nuclear forces take place, they start attracting each other via the strong forces and can combine into a nucleus of helium-4 (α-particle) with the emission of a high energy neutron:

$$D + T \rightarrow \alpha(3.5MeV) + n(14.1MeV). \tag{1.1}$$

The energy release (in a form of kinetic energies of α and neutron particles) is explained by the attracting nature of the strong forces. Since nucleons are bound within a nucleus, its mass is less than the system of the separate nucleons. This difference is numerically expressed in a so-called binding energy:

$$B(A, Z) = (Zm_p + Nm_n)c^2 - M(A, Z)c^2, \tag{1.2}$$

which is positive for a stable nucleus. Here, m_p, m_n, $M(A, Z)$ are proton, neutron and nucleus masses, Z, N are a number of protons (charge number) and neutrons, $A = N + Z$ is the mass number, c is the speed of light. If a nuclear reaction leads to nuclei with higher binding energy, the reaction is exothermic, i.e. some energy Q is released from nuclear bonds. By using data from Table 1.1, one can find the energy produced during the DT reaction

$$Q_{DT} = M_D c^2 + M_T c^2 - M_\alpha c^2 - m_n c^2 = B_\alpha - B_D - B_T = 17.589\ MeV. \tag{1.3}$$

Nuclide ${}^A_Z X$	Mass (amu)	Binding energy (MeV)
D	2.01410177811	2.225
T	3.01604928199	8.482
α (${}^4_2 H_e$)	4.00260325413	28.296
${}^3_2 H_e$	3.01602932007	7.718

Table 1.1: Nuclear masses and binding energies [1]. Atomic mass unit 1 amu = 931.494 MeV/c^2 (see [2]), neutron mass $m_n = 1.0086649158$ amu and proton mass $m_p = 1.00782503224$ amu (see [1]).

Because of the momentum conservation, it is the lighter neutron that takes most of the released energy. Since the hydrogen isotope, tritium, T is unstable with a half-life around 12.32 years, it is rare on Earth and should be produced in nuclear reactors. In principle, there are other possible fusion reactions such as

$$D + D \rightarrow T + p + 4.033\ MeV, \tag{1.4}$$

$$D + D \rightarrow {}^3He + n + 3.269\ MeV \tag{1.5}$$

that actually do not require the rare and expensive tritium. The problem is that the nuclei have to overcome repulsive electrostatic (ES) forces to approach close enough so that the strong force becomes the dominant one. Because of that, the DT or DD mixture has to be heated to a very high temperature, where it turns into a *plasma state*, and the DT reaction has the largest reaction rate at temperatures of the order of $T = 10\ keV$ [1] [2]. On the other hand, the DD reaction rate remains much smaller. In particular, at $T = 10.3\ keV$ the DT reaction rate is around $1.34 \cdot 10^{-22}\ m^3/s$, while it is $5.93 \cdot 10^{-25}\ m^3/s$ for the DD reaction [3, 4].

The α-particles produced in Reaction 1.1 should remain confined during a significantly long time period within a thermonuclear reactor so that they can transfer their energy to deuterium and tritium nuclei via collisions. The condition for a so-called ignited plasma, when the produced α particles can maintain the required plasma temperature, and no external heat sources are required to compensate power losses such as radiation and heat transport in a thermonuclear reactor, is known as *Lawson criterion* [5]

$$nT\tau_e \geq 10^{21} \quad keV \cdot s/m^3. \tag{1.6}$$

[1] The Boltzmann constant $k_B = 1.380\ 649 \cdot 10^{-23}\ J/K$ is set to 1, and the temperatures are treated in energy units (J or eV).

[2] $T[eV] = T[K]k_B[J/K]/e[J/eV] = T[J]/e[J/eV] = T[K] \cdot 8.617\ 333 \cdot 10^{-5}$,
where $e = 1.602\ 176\ 634 \cdot 10^{-19}\ J/eV$ is the elementary charge.

It states that the DT plasma has to be maintained with a high enough density n and temperature T during a sufficiently long time interval τ_e. Here, τ_e is the so-called energy *confinement time*, a characteristic time period during which the temperature of the DT mixture inside of a fusion reactor reduces by a factor of $\exp(-1)$ when all heat sources (including the heating due to the DT reactions) are turned off. Nowadays, most of the research in the fusion plasma field is focused on increasing the triple product on the left hand side of Eq. 1.6 avoiding at the same time operational limits, for example, on the plasma pressure beyond which strong instabilities are developed.

Neutrons released in the DT reactions impinge on reactor walls, where their kinetic energy will be collected by a heat transfer fluid (for example, cooled helium). The neutrons can also be used to maintain the level of tritium in a thermonuclear reactor by adding lithium in designed modules mounted on the wall of the machines and exploiting the reaction

$$^6Li + n \rightarrow {}^4He + T. \tag{1.7}$$

The fusion nuclear reactions described above cannot lead to an uncontrolled regime causing a nuclear explosion as it might happen in fission nuclear reactors because of the chain reactions. The DT reactions do not produce radioactive waste. Neutrons produced in the fusion reactions activate materials only in the reactor walls. Apart from that, fusion has much higher energy release per unit fuel mass than even fission. More precisely, around 200 MeV per one ^{235}U nucleus is produced in a fission nuclear reactor, which is $\sim 82\ TJ/kg$. In a fusion DT reaction, 14.1 MeV per one DT pair is generated, where we assume that 3.5 MeV of α-particle kinetic energy is used to sustain the plasma, and it corresponds to $\sim 270\ TJ/kg$. As a result, reactors based on the fusion nuclear principle might provide a significantly cleaner, safer, and more efficient source of energy.

1.2 The tokamak

In a fusion reactor, the DT mixture is heated to a temperature around 10 keV. Under such conditions, it turns into a hot plasma that must be kept inside of the reactor without touching the walls. One of the possible options to achieve this is the magnetic confinement that is based on the Larmor rotation of charged particles around a magnetic field line restricting their perpendicular motion. A toroidal axisymmetric configuration of the magnetic field is implemented in the *tokamak* concept (Fig. 1.1). The machine size is characterized by a *major radius* R_0 and *minor radius* a_0 that

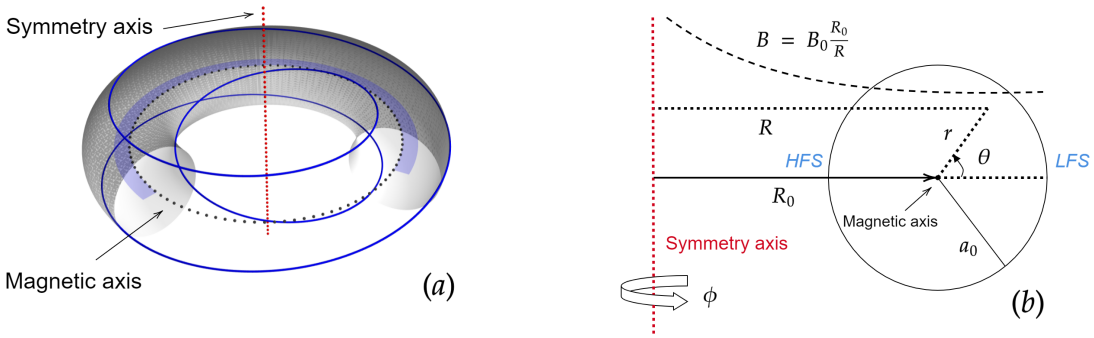

Figure 1.1: Toroidal magnetic configuration (Fig. 1.1a), where a passing particle trajectory for a case with a safety factor $q = 3$ (blue line), and a Σ plane (light blue area, Eq. 1.10) are shown. Fig. 1.1b: a circular poloidal cross-section of a tokamak with a major radius R_0 of the magnetic axis and a minor radius a_0. LFS is a Low Field Side of a torus, where B_ϕ achieves its minimum inside of the plasma, while HFS is a High Field Side. The toroidal angle ϕ and poloidal angle θ are periodic coordinates, and the corresponding Fourier expansion of any plasma quantity in these coordinates is associated with the *toroidal number* n and *poloidal number* m respectively.

define the *inverse aspect ratio* $\varepsilon = a_0/R_0$ of the tokamak. The poloidal cross-section of the background field can be circular or, for example, vertically elongated that is numerically defined by the parameter called *elongation* $\kappa \geq 1$. The magnetic field is represented as a superposition of a dominant toroidal component B_ϕ produced by external coils, and a poloidal part $B_\theta \ll B_\phi$, generated by an induced toroidal plasma current. It is simple to show from Ampère's law that the toroidal magnetic field produced by the external coils scales with R^{-1} (Fig. 1.1b). The inner part of the tokamak ($R < R_0$) is thus called the *High-Field Side* (HFS), while the outer part ($R > R_0$) is called the *Low-Field Side* (LFS). The superposition of toroidal and poloidal fields leads to helical field lines connecting LFS and HFS, and defining so-called *magnetic surfaces* (Fig. 1.1a). The magnetic field configuration is characterised by a radial profile of a *safety factor* q, which is related to the rotation angle of the field lines at different radial points. Loosely speaking, if a field line moves more slowly in the poloidal direction than in the toroidal one (in other words, rotates several times toroidally while doing only one poloidal rotation) then $q > 1$. For a large aspect ratio tokamak ($\varepsilon^{-1} \gg 1$) with a circular cross-section, the safety factor

can be approximated as [6]

$$q = \frac{rB_\phi}{RB_\theta}. \tag{1.8}$$

In a realistic non-circular geometry, a precise q-profile is calculated numerically that usually involves solving the so-called Grad-Shafranov equation. This equation defines an ideal (without taking into account resistivity) equilibrium between the plasma pressure p and the magnetic-field "cage" in an axisymmetric plasma system. In such a system, the field lines lie on nested toroidal surfaces (magnetic surfaces). The equilibrium condition is expressed by the magnetohydrodynamic (MHD) force balance (compare to Eq. 1.16 below)

$$\frac{\mathbf{j} \times \mathbf{B}}{c} = \boldsymbol{\nabla} p, \tag{1.9}$$

where $\mathbf{j}$ is the plasma current density. Since clearly $\mathbf{B} \cdot \boldsymbol{\nabla} p = 0$, the magnetic surfaces become surfaces of constant pressure. For this reason, the pressure becomes a function of only a radial coordinate, while the magnetic field has also a poloidal dependence. It is convenient to introduce the *poloidal magnetic flux* function ψ

$$\psi = \frac{1}{2\pi} \int_\Sigma \mathbf{B} \cdot \mathrm{d}\mathbf{S} \tag{1.10}$$

as a radial coordinate in a tokamak geometry, since this function is constant on the magnetic surfaces. Here, Σ is a circular area between the magnetic axis and a chosen magnetic surface (Fig. 1.1a), which is perpendicular to the poloidal component of the background magnetic field $\mathbf{B}$. By setting predefined $B_\phi(\psi)$ and $p(\psi)$ profiles in the Grad-Shafranov equation mentioned above, one gets as a solution a poloidal profile of the ψ function in a form of nested surfaces $\psi = constant$.

It is important to understand how charged particles move in the magnetic configuration of a tokamak. When a particle moves along a magnetic field line, it explores the poloidal variation of the magnetic field (Fig. 1.2b). As a result, certain particles can be trapped due to the so-called magnetic mirror effect. By considering for the sake of simplicity a static electromagnetic (EM) field, one can find that the total energy of a particle $\mathcal{E}_{tot}$ and its *magnetic moment* μ are conserved along the particle trajectory:

$$\mathcal{E}_{tot} = \frac{1}{2} m_p v^2 + Ze\Phi = const, \tag{1.11}$$

$$\mu = \frac{m_p v_\perp^2}{2B} = const. \tag{1.12}$$

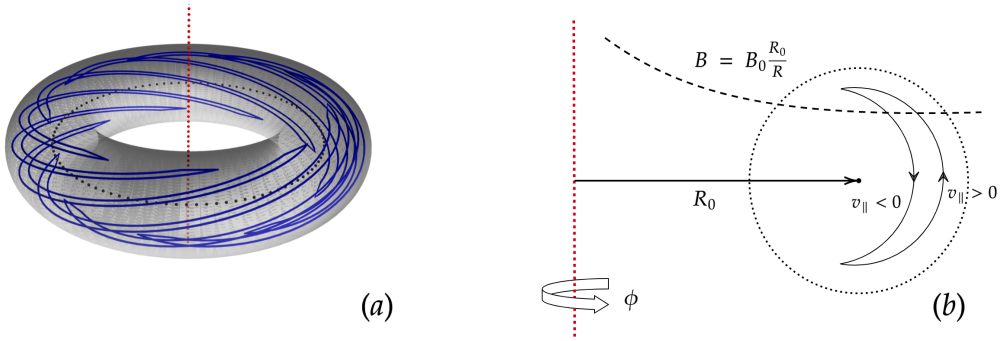

Figure 1.2: Cartoon of trapped particle trajectories in a torus (Fig. 1.1a) and their poloidal projection (Fig. 1.1b).

Here, m_p, Ze are a particle mass and charge ($Z = -1$ for electrons), Φ is an electrostatic potential, which is assumed farther to be zero. From these equations, the parallel component of the particle velocity can be found:

$$v_\parallel^2 = \frac{2}{m_p}(\mathcal{E}_{tot} - B\mu). \tag{1.13}$$

This means that a particle can be reflected from the HFS if its parallel kinetic energy is not high enough (Fig. 1.2), and be trapped in a magnetic well. The trapping condition at the radial point r can be estimated in the following way

$$\left.\frac{v_\parallel}{v_\perp}\right|_{\theta=0,r} \leq \sqrt{2\varepsilon(r)}, \tag{1.14}$$

and it is the so-called *passing-trapped boundary*, where the particle velocity components $v_\parallel, v_\perp$ and a local inverse aspect ratio $\varepsilon(r) = r/R$ are taken at a radial point r on the low-field side ($\theta = 0$) of the torus. Here, the particles localised near this boundary are called *barely trapped* (or *barely passing*).

1.3 Plasma confinement and the geodesic acoustic mode (GAM)

One of the remaining key physics problems on the way to the realization of an efficient fusion reactor based on the described toroidal magnetic confinement is the thorough understanding and reliable prediction of the so-called anomalous transport of heat,

momentum, and particles across the magnetic surfaces. It is by now commonly attributed to turbulence which is driven by various plasma microinstabilities such as drift waves (DWs) which extract free energy from the background temperature and density gradients. They are known to self-organize to form mesoscopic (around $0.1a_0$) structures [7]. These structures take the form of a radial electric field which depends spatially only on the radial coordinate. $E \times B$ poloidal flows associated with this electric field are referred to as *zonal flows* (ZFs) [8, 9, 10, 11]. For a simple physical picture of the $E \times B$ drift see e.g. [6].

The action of the toroidal magnetic field curvature on the ZFs gives rise to oscillations of the radial electric field. These ZF oscillations are called *Geodesic Acoustic Modes* (GAMs). The importance of the zonal structures (ZSs), both ZFs and GAMs, is that they can regulate the drift-wave turbulence [12] and possibly can play a vital role in the transition from the low to the high confinement regime (L-H transition) [13]. The turbulence suppression by the ZFs was observed, for example, in experiments described in [14]. The geodesic modes can also be directly driven by the drift waves [15, 16, 17] through the three-waves coupling. In this sense, the GAMs as well as the stationary zonal flows can be considered as a sink of the turbulent energy. On the other side, the *geodesity* (magnetic field curvature due to the toroidal geometry) by itself, independently on the GAM presence, transfers energy from the zonal flows back to the turbulence as it was demostrated in [18, 19]. A good overview of the zonal structures, both stationary and oscillatory, is given in [10], and some recent kinetic theories of the GAMs are described in [20].

The GAMs are the main subject of this thesis. The underlying physics is summarized in this section, while the interaction of the zonal structures with the drift-wave turbulence is discussed in Sec. 1.5. We first consider a simple derivation of the GAM oscillation based on the equations of ideal MHD [21]. Later in this section, a physical interpretation of these results is discussed and illustrated through the results of direct numerical simulations.

To estimate the GAM frequency, one can use the ideal MHD model that considers the plasma as a single neutral fluid [22] if the plasma satisfies a set of specific assumptions (one can see [23] for more details). The ideal MHD couples hydrodynamics

$$\frac{\partial \rho}{\partial t} + \boldsymbol{\nabla} \cdot (\rho \boldsymbol{v}) = 0, \quad \textit{Continuity equation} \tag{1.15}$$

$$\rho \left(\frac{\partial \boldsymbol{v}}{\partial t} + \boldsymbol{v} \cdot \boldsymbol{\nabla} \boldsymbol{v} \right) = -\boldsymbol{\nabla} p + \frac{\mathbf{j} \times \mathbf{B}}{c}, \quad \textit{Momentum equation} \tag{1.16}$$

$$\frac{\partial p}{\partial t} + (\mathbf{v} \cdot \boldsymbol{\nabla}) p + \Gamma p \boldsymbol{\nabla} \cdot \boldsymbol{v} = 0, \quad \textit{Adiabatic energy equation} \tag{1.17}$$

with Maxwell's equations

$$\frac{\partial B}{\partial t} = -c\boldsymbol{\nabla} \times \boldsymbol{E}, \quad \textit{Induction equation } (\textit{Faraday's law}) \tag{1.18}$$

$$\mathbf{E} + \frac{\boldsymbol{v} \times \mathbf{B}}{c} = 0, \quad \textit{Ideal Ohm's law} \tag{1.19}$$

$$\mathbf{j} = \frac{c}{4\pi}\boldsymbol{\nabla} \times \mathbf{B}, \quad \textit{Ampère's law} \tag{1.20}$$

$$\boldsymbol{\nabla} \cdot \mathbf{B} = 0. \quad \textit{Divergence constraint} \tag{1.21}$$

to describe the macroscopic dynamics of highly conducting (with a zero resistivity) plasma fluid. In the following we linearise these equations by splitting every quantity in a background and a perturbation part. Hence, $p = p_0 + \delta p$ is the plasma pressure, $\rho = \rho_0 + \delta\rho$ is the plasma density, $\boldsymbol{v}$ is the plasma velocity perturbation (we assume here there is not any background velocity), Γ is the ratio of the specific heats. The field is represented by the electric perturbation $\mathbf{E}$ (again, no background electric field), and the background magnetic field $\mathbf{B} = \mathbf{B}_0$. The perturbations evolve in time and space. On the other hand, we assume that the background density ρ_0 and pressure p_0 are stationary and have flat profiles. The background magnetic field is approximated as[3]

$$B = B_0(1 - r/R_0 \cos\theta + \mathcal{O}(\varepsilon^2)) \tag{1.22}$$

for the local cylindrical coordinate θ. The magnetic field curvature is defined as

$$\boldsymbol{K} = \mathbf{b} \cdot \boldsymbol{\nabla}\mathbf{b} = \frac{\boldsymbol{\nabla}_\perp B}{B} + \frac{4\pi}{c}\frac{\mathbf{j} \times \mathbf{B}}{B^2}, \tag{1.23}$$

where $\nabla_\perp$ is the space derivative perpendicular to the field unit vector $\mathbf{b} = \mathbf{B}/B$. We are going to consider a low-pressure plasma system where one can neglect the $|\boldsymbol{j} \times \boldsymbol{B}| \ll 1$ term in the above equation (compare to Eq. 1.9). In such a system, the field curvature becomes

$$\boldsymbol{K} \approx \frac{\boldsymbol{\nabla}_\perp B}{B} = \frac{1}{R_0}(-\cos\theta \boldsymbol{e}_r + \sin\theta \boldsymbol{e}_\theta), \tag{1.24}$$

where

$$K_G = \frac{\sin\theta}{R_0} \tag{1.25}$$

[3]Here, the poloidal angle θ starts from the low-field-side.

is the *geodesic curvature* of the system.

The order of magnitude of the GAM frequency can be derived in ideal MHD (see also [24]) starting with the linearised momentum and energy equations:

$$\rho_0 \frac{\partial \boldsymbol{v}}{\partial t} = -\boldsymbol{\nabla}\delta p, \tag{1.26}$$

$$\frac{\partial \delta p}{\partial t} = -\Gamma p_0 \boldsymbol{\nabla}\cdot\boldsymbol{v}. \tag{1.27}$$

Here and in the following, we are going to consider only the electric field perturbation that is enough to describe essential GAM dynamics (see also Chapter 3). Therefore, we don't include here the terms like $\delta\boldsymbol{j}\times\boldsymbol{B}_0$ and $\boldsymbol{j}_0\times\delta\boldsymbol{B}$. An initial zero-frequency zonal flow described by an electric zonal potential $\overline{\phi}$ is assumed to be present in our plasma system. Here and farther in this work, under the term "zonal" we understand a *flux-surface averaged quantity* (averaged or constant along both toroidal and poloidal directions), which is characterized by a toroidal $n = 0$ and poloidal $m = 0$ Fourier components, while other n and m components are equal to zero. Due to the presence of the zonal flow, one observes a plasma flow perpendicular to the background magnetic field $\mathbf{B}$ along the magnetic surface

$$\boldsymbol{v}_\perp = \frac{c}{B^2}\boldsymbol{B}\times\boldsymbol{\nabla}_\perp\overline{\phi}, \tag{1.28}$$

which is the so-called $E\times B$ drift. Here and in the following, we will consider only the electrostatic contribution to the electric field, consistently with the low frequency of these oscillations. Since the zonal signal $\overline{\phi}$ does not depend on the poloidal coordinate θ, the perpendicular derivative is reduced to that along the radial coordinate r:

$$\boldsymbol{\nabla}_\perp\overline{\phi} = \boldsymbol{e_r}\partial_r\overline{\phi}. \tag{1.29}$$

Now, we are going to consider only the transverse plasma motion $\boldsymbol{v}\to\boldsymbol{v}_\perp$, which is related to the GAM formation due to the inhomogeneity of the background magnetic field. We take the time derivative of the momentum equation (Eq. 1.26), and then apply to it the operator $\boldsymbol{\nabla}\cdot(\boldsymbol{B}/B^2\times ...)$ with the assumption of a small inverse aspect ratio $\varepsilon \ll 1$. Finally, by taking into account the time derivative of the pressure from Eq. 1.27, we obtain the following equation for the zonal potential

$$-\frac{\rho_0}{B_0^2}\frac{\partial^2}{\partial t^2}\nabla_\perp^2\overline{\phi} = \Gamma p_0\left(\boldsymbol{\nabla}\cdot\frac{\mathbf{B}}{B^2}\times\boldsymbol{\nabla}\right)^2\overline{\phi}. \tag{1.30}$$

The expression in the brackets on the right hand side can be evaluated in the following way

$$\boldsymbol{\nabla}\cdot\left(\frac{\boldsymbol{B}}{B^2}\times\boldsymbol{\nabla}\right) = \left(\boldsymbol{\nabla}\left(B^{-2}\right)\times\boldsymbol{B} + \frac{\boldsymbol{\nabla}\times\boldsymbol{B}}{B^2}\right)\cdot\boldsymbol{\nabla} = \frac{2}{B}\boldsymbol{b}\times\boldsymbol{K}\cdot\boldsymbol{\nabla}, \tag{1.31}$$

where we have used again the low-pressure approximation and Eq. 1.24[4]. Since the zonal potential $\overline{\phi}$ depends only on the radial coordinate (and time), we take into account only the radial component of the vector product

$$(\boldsymbol{b} \times \boldsymbol{K}) \cdot \boldsymbol{e}_r = -\frac{\sin\theta}{R_0} = -K_G \tag{1.34}$$

and we finally obtain that

$$\boldsymbol{\nabla} \cdot \left(\frac{\boldsymbol{B}}{B^2} \times \boldsymbol{\nabla} \right) = -2 \frac{K_G}{B_0} \nabla_\perp. \tag{1.35}$$

By using this expression and by flux-averaging Eq. 1.30 to eliminate the dependence on the poloidal angle θ, one gets

$$\left(\frac{\partial^2}{\partial t^2} + \omega_{GAM}^2 \right) \partial_r^2 \overline{\phi} = 0, \tag{1.36}$$

where the oscillatory dynamics of the GAM appears due to the geodesic curvature

$$\omega_{GAM} = 2\sqrt{\overline{K_G^2} \frac{\Gamma p_0}{\rho_0}} = \sqrt{2} \frac{v_s}{R_0}, \tag{1.37}$$

$$\overline{K_G^2} = \frac{1}{2R_0^2},\ v_s = \sqrt{\frac{\Gamma p_0}{\rho_0}}. \tag{1.38}$$

Here, v_s is the sound speed known from basic mechanics. The fluid model provides an approximation of the GAM frequency, while the GAM damping due to the wave-particle interaction can be calculated only in the kinetic framework, which is presented in Chapter 3.

Now, by considering the linearised continuity equation

$$\frac{\partial \delta\rho}{\partial t} = -\rho_0 \boldsymbol{\nabla} \cdot \boldsymbol{v}_\perp, \tag{1.39}$$

one can investigate how the plasma density changes in time during the GAM evolution. By substituting the $E \times B$ drift (Eq. 1.28) into Eq. 1.39, using the vector

[4]Here, the following equations are applied as well

$$\boldsymbol{b} \times \boldsymbol{\nabla} B = \boldsymbol{b} \times \boldsymbol{\nabla}_\perp B, \tag{1.32}$$

$$\boldsymbol{\nabla} \times (f\boldsymbol{A}) = \boldsymbol{\nabla} f \times \boldsymbol{A} + f \boldsymbol{\nabla} \times \boldsymbol{A}, \tag{1.33}$$

where f is some scalar value, while $\boldsymbol{A}$ is a vector.

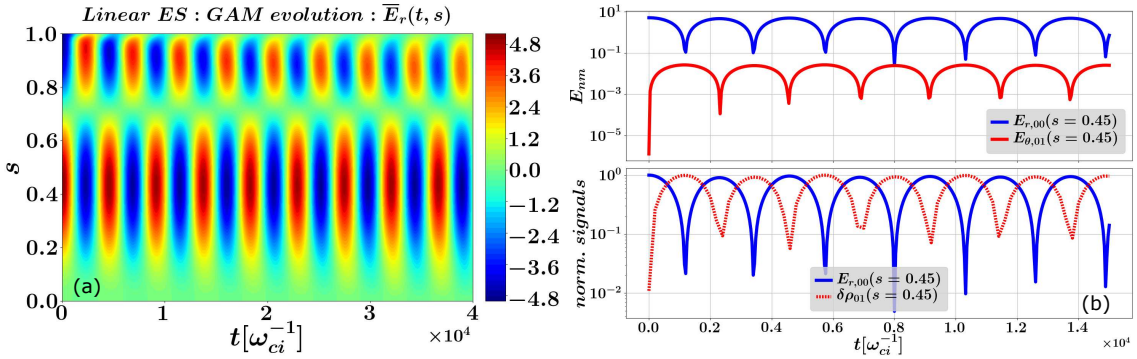

Figure 1.3: Linear electrostatic simulations of GAMs in ORB5. Here, s is a radial normalised coordinate, t is a time normalised to a deuterium cyclotron frequency $\omega_{ci} = eB_0/(m_d c)$. Fig. 1.3a: radial structure of the zonal $(n = 0, m = 0)$ radial electric field $\overline{E}_r$. Fig. 1.3b, upper plot: time evolution at $s = 0.45$ of the zonal radial electric field, and of the $n = 0, m = 1$ component of poloidal electric field, where $E_{r,00}$ is equivalent to $\overline{E}_r$. Fig. 1.3b, bottom plot: time evolution at $s = 0.45$ of the zonal radial electric field and of the $n = 0, m = 1$ component of the deuterium density, where the signals are normalised to their maximums.

expression Eq. 1.35, and finally, taking time Fourier transformation, one obtains the GAM density perturbation

$$\delta\rho = -i\frac{2\rho_0 c}{\omega_{GAM} R_0 B_0}\nabla_r\overline{\phi}\sin\theta. \tag{1.40}$$

Due to the poloidal dependence $\sin\theta$, which arises from the geodesic curvature (Eq. 1.25), the zonal field is accompanied by poloidally asymmetric $(m = 1)$ density perturbations, so-called sidebands. In other words, GAMs are characterized by a zonal electric field that couples through the geodesic curvature (also called *toroidicity* or *geodesity*) with the plasma density resulting in the rise of up-down poloidally asymmetric density sidebands. Apart from that, one can see from Eq. 1.40 that the field perturbation is shifted in time with respect to the density perturbation by $\pi/2$, which is mathematically expressed by the presence of the imaginary unit i.

Further physical insight can be gained through the analysis of a numerical simulation of the GAM oscillation (simulations of this kind will play a fundamental role in the present thesis). Here, let us consider a linear gyrokinetic electrostatic (ES)[5]

[5]In electrostatic simulations, the Ampère equation is not taken into account. That is why, the

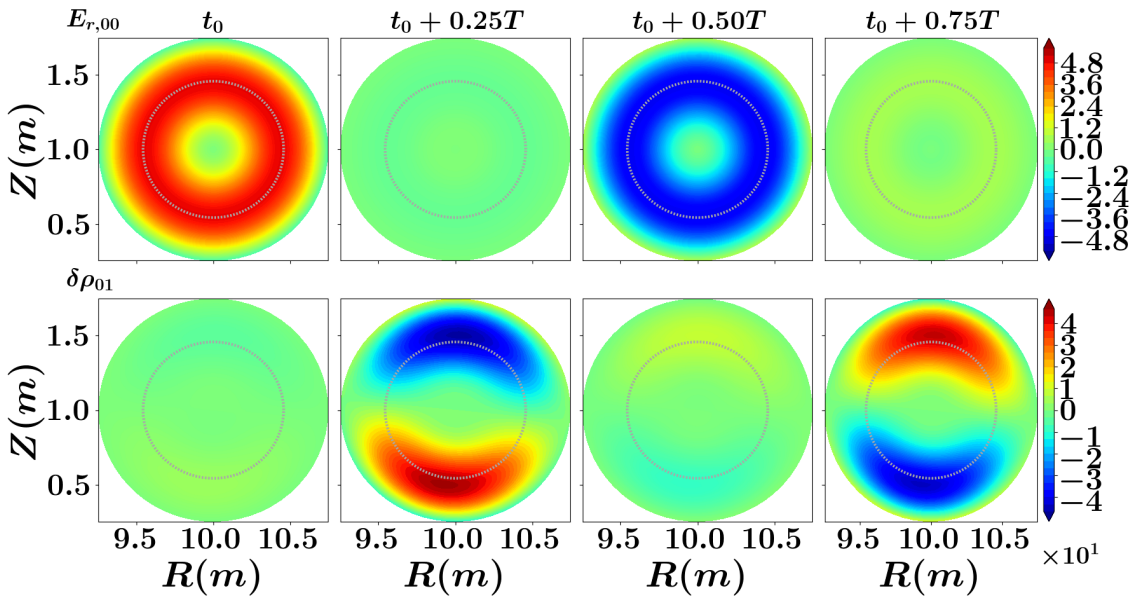

Figure 1.4: Electrostatic linear simulations of the GAMs in ORB5. Poloidal cross-sections of the zonal electric field $E_{r,00}$ (upper row), and of the sideband ($n = 0, m = 1$) of the deuterium density perturbation $\delta\rho_{01}$ (lower row) are shown at different time moments of the GAM period T. The radial domain is reduced up to $s = 0.75$ to make the plots clearer. The grey line indicates the radial point $s = 0.45$, around which the GAM is localised.

simulation of a GAM in a tokamak magnetic geometry with a circular poloidal cross-section with a minor radius $a_0 = 1\ m$ and major radius $R_0 = 10\ m$. Species density and temperature profiles are taken flat as well as the safety factor profile. Values of the plasma temperature and safety factor ($T_d = T_e = 14.1\ keV$, $q = 4.0$) are taken in such a way to guarantee a small damping rate of the geodesic mode. This simplified modelling is performed with the global GK code ORB5 [25, 26, 27] that is described in Chapter 2. In this simulation, the plasma consists of deuterium (with a mass m_d and charge e) and adiabatic electrons.[6] To excite GAMs in the studied plasma system, we impose an initial zonal deuterium density perturbation with a radial wavelength $\lambda \sim a_0$. Results of these simulations are presented in Fig. 1.3 and

evolution of the magnetic field is not considered, and only the electric potential perturbations can be investigated.

[6]This means that there is not any phase shift between the electron density and the electric potential, the electrons react immediately to the field perturbation (see Eq. 3.12).

Fig. 1.4.

First of all, according to Fig. 1.3a, a GAM, which emerges due to the imposed initial density perturbations, is localised around a normalised radial coordinate $s \sim 0.45$[7]. The bottom plot in Fig. 1.3b shows that the oscillations of the zonal electric field $\overline{E}_r = -\nabla_r \overline{\phi}$ during the GAM evolution are accompanied by a poloidally asymmetric ($m = 1$) density perturbation, which is shifted in time by $\pi/2$ with respect to the electric field. This is consistent with Eq. 1.40. From Fig. 1.4, it can be seen that these perturbations are up-down asymmetric in the poloidal cross-section, and the mentioned shift is observed as well. Because of the density sidebands, a poloidally asymmetric component $n = 0, m = 1$ of the GAM electric field arises (Fig. 1.3b, upper plot) to compensate the poloidal density gradient, but its amplitude is more than two orders of magnitude smaller than that of the zonal component.

Now, we can sketch a picture of the GAM time evolution. At the beginning of a GAM period T, the zonal electric field produces the $v_{E\times B}$ plasma drift (Eq. 1.28), whose amplitude is higher at the low-field side of the poloidal cross-section than that on the high field side due to the radial gradient of the background magnetic field. Therefore, there is an accumulation of the plasma density with an up-down asymmetry, which achieves its maximum at a quarter of the GAM oscillation, while the zonal electric field turns to zero. Rise of the density sidebands leads to the appearance of the poloidally asymmetric electric field perturbation that creates a plasma current and, as a result, removes the density perturbation. At a half GAM period, the zonal electric field again achieves its maximum value but in the opposite direction, which results in a reversed $E \times B$ plasma drift. Due to that, the density sidebands swap their maximums and minimums, and the process repeats starting a new GAM period.

1.4 GAM damping and EGAM excitation

One of the leading linear damping mechanisms for stationary ZFs is collisional processes [9]. At the same time, for the GAM, it is a collisionless wave-particle interaction, namely the *Landau damping* [28, 29, 30], and collisional damping at the very edge of the plasma, where equilibrium temperatures drastically decrease[8] [31]. The wave-particle interaction takes place when a particle velocity is close to the phase

[7]Here, $s \sim \sqrt{\psi}$ (Eq. 1.10), and $s = 0.0$ refers to the plasma center, while $s = 1.0$ refers to the plasma edge.

[8]The collision frequency decreases in a hot plasma with increasing temperature as $T^{-3/2}$ (Eq. 4.15).

velocity of a wave. More precisely, if a particle speed is slower than the phase velocity of the considered wave, then the particle takes energy from the wave and gets accelerated. In the opposite case, it is the wave that gets energy from the particle.

To outline an algorithm for the damping rate derivation, we consider the simplest one-dimensional (in both real and velocity spaces) plasma system described by linearised Vlasov and Poisson equations:

$$\frac{\partial \delta f}{\partial t} + v\frac{\partial \delta f}{\partial x} - \frac{Z_i e}{m}\frac{\partial \Phi}{\partial x}\frac{\partial f_0}{\partial v} = 0, \tag{1.41}$$

$$-\frac{\partial^2 \Phi}{\partial x^2} = 4\pi Z_i e \int \delta f \, \mathrm{d}v. \tag{1.42}$$

Here, only the ion (deuterium, $Z_i = 1$) density is perturbed, and the perturbation is described by the δf, while the equilibrium ion and electron charge densities are equal to each other ($Z_i e \int f_0 \, \mathrm{d}v - e \int f_{0,e} \, \mathrm{d}v = 0$, where $n_0 = \int f_0 \, \mathrm{d}v$). To get rid of the dimensional parameters, the following normalisation can be employed

$$\hat{t} = t\omega_p, \ \hat{x} = \frac{x}{\lambda_D}, \ \hat{v} = \frac{v}{v_{th}}, \ \hat{f} = f\frac{v_{th}}{n_0}, \ \hat{\Phi} = \Phi\frac{e}{T}, \tag{1.43}$$

where the ion plasma frequency ω_p, the Debye length λ_D and the thermal velocity v_{th} are used for the normalisation:

$$\lambda_D = \sqrt{\frac{T}{4\pi n_0 e^2}}, \ v_{th} = \sqrt{\frac{T}{m}}, \ \omega_p = \frac{v_{th}}{\lambda_D}. \tag{1.44}$$

Farther in this section, we are going to omit the hat for simplicity. As a result, we obtain the normalised Vlasov-Poisson system, and after Fourier transform in space and Laplace transform in time

$$\delta f \to \delta f \exp(ikx - i\omega t), \tag{1.45}$$

$$\Phi \to \Phi \exp(ikx - i\omega t) \tag{1.46}$$

with the wavenumber k and the complex frequency $\omega = \omega_r + i\gamma$, the system turns into

$$(\omega - kv)\delta f + k\Phi\frac{\partial f_0}{\partial v} = 0, \tag{1.47}$$

$$k^2\Phi = \int \delta f \, \mathrm{d}v. \tag{1.48}$$

By combining these two equations, one can get the following dispersion relation

$$\mathcal{D}(k,\omega) = k^2 + \int_{-\infty}^{+\infty} \frac{k\partial_v f_0}{\omega - kv}\,\mathrm{d}v = 0, \tag{1.49}$$

It can be analytically continued by deforming the integration contour along v into the complex plane to keep the resonance $\omega = kv$ inside the contour (such an analytical continuation for the Plasma Dispersion Function is described in Appendix A):

$$\mathcal{D}(k,\omega) = \mathcal{D}_r(k,\omega) + i\mathcal{D}_i(k,\omega) = 0, \tag{1.50}$$

$$\mathcal{D}_i(k,\omega) = -\pi\partial_v f_0|_{v=\omega_r/k}. \tag{1.51}$$

Finally, by assuming a smallness of the wave damping ($|\gamma| \ll \omega_r$), and by decomposing the dispersion relation in the Taylor series with respect to γ, one obtains

$$\gamma = -\frac{\mathcal{D}_i(k,\omega_r)}{\partial_\omega \mathcal{D}_r(k,\omega)|_{\omega=\omega_r}} \sim \partial_v f_0|_{v=\omega_r/k}. \tag{1.52}$$

Here, one can see that the sign in front of the velocity derivative of the equilibrium distribution function defines whether the wave is going to grow (+) or decay (−).

In case of the GAM, its phase speed is close to the parallel velocity of thermal ions. Since the thermal ions have a Maxwellian distribution function in velocity space, the number of particles with smaller parallel velocity than the GAM phase speed is higher than the number of particles with higher velocities, and in this case we are dealing with the Landau damping of the wave. Because of that, the thermal ions take energy from the GAM, and the wave energy is damped.

Speaking about thermal electrons, we should note that their parallel velocity generally is much higher than that of the ions. That is why it was believed during a long time that the role of the electrons is negligible in the GAM damping. However, the passing and trapped electrons, which are localised near the passing-trapped boundary (Eq. 1.14), have much smaller velocities and can resonate with the geodesic modes. This interaction was shown for the first time in [32] and was investigated later in [33, 34, 35, 36]. In this work, the GAM damping by electrons is calculated in a magnetic configuration of *ASDEX Upgrade* (AUG) tokamak in Chapter 4.

If energetic particles are injected in the plasma system, we can observe an inverse Landau damping that excites Energetic particle driven Geodesic Acoustic Modes (EGAMs) [37, 38]. The energetic (or fast) particles can be described by a Maxwellian distribution function shifted in parallel velocity. If the phase velocity of the GAM is localised on a positive slope of the shifted Maxwellian, the number of fast particles with higher velocity than the wave phase velocity is higher than that of lower velocity

particles. As a result, the EGAM energy grows due to the interaction with the energetic particles. On the other hand, the mode still transfers its energy to the thermal species. In Chapters 6 and 7, linear and nonlinear EGAM dynamics and the mode interaction with thermal and energetic species are studied in an AUG discharge.

Due to the so-called *phase mixing* effect, considered in Chapter 4, the GAM damping rate increases in the presence of a temperature or safety factor gradients [16, 39, 40, 41]. This effect arises when the wave damping rate depends on its wavenumber. In the case of the GAM, the damping rate increases with the mode radial wavenumber. Since the GAM frequency depends on the temperature and safety factor, the GAM oscillates with different frequencies at different radial points. Distorting the GAM radial structure and creating higher radial wavenumbers, the phase mixing process can sharply increase the GAM damping rate [16, 41].

1.5 Drift instabilities and the excitation of zonal structures

So far in this introduction, we did not discuss how the zonal structures can arise in toroidal systems. This issue is addressed in this section. Tokamak plasma exhibits a high variety of microinstabilities among which the so-called drift instabilities largely control plasma transport across magnetic surfaces [42]. In a tokamak, one of the dominant types of the drift instability is the *Ion Temperature Gradient* (ITG) instability (more precisely, a toroidal ITG [43]), which is driven by temperature gradient of thermal ions, and is characterized by a poloidal wavelength $k_\theta^{ITG}\rho_i \sim 0.5$, where ρ_i is the ion thermal Larmor radius

$$\rho_i = \frac{u_{th,i}}{\omega_{ci}}, \quad u_{th,i} = \sqrt{\frac{2T_i}{m_i}}, \quad \omega_{ci} = \frac{Z_i e B}{m_i c}. \tag{1.53}$$

Here, $u_{th,i}$ is the ion thermal velocity, ω_{ci} is the ion cyclotron frequency. The temperature driven mode is characterised by a threshold behaviour. It becomes unstable when the temperature gradient overcomes a critical value. When it happens, the nonlinear dynamics of the fluctuating unstable field produces turbulence, which causes a plasma convection across magnetic surfaces.

Fig. 1.5 shows a cartoon of ITG destabilization on the low-field side plasma domain [43]. In a toroidal plasma, a particle drift due to the magnetic field nonuni-

formity arises, which can be approximated as (see Eq. 3.19)

$$\boldsymbol{v}_d = \frac{v_\parallel^2 + v_\perp^2/2}{\omega_{ci} B^2} \boldsymbol{B} \times \boldsymbol{\nabla} B. \tag{1.54}$$

Taking into account the negative direction of the background magnetic field gradient and direction of the **B** field itself as depicted in Fig. 1.5, one can see that the resulting drift velocity is directed upwards, which means counter-clockwise on the low-field side. Let us assume that an initial ion temperature perturbation with a small poloidal extension appears in the plasma system. Since the plasma drift velocity Eq. 1.54 depends on the plasma temperature ($v_\parallel^2 + v_\perp^2/2 \sim v_{th,i}^2$), the ions move faster within the domains with higher temperature than within the colder ones. It results in ion density perturbations localised between the hot and cold spots. Due to the quasi-neutrality, the ion density perturbation produces an electric field, directed poloidally from higher ion density to the lower density areas. As a consequence, a radial $E \times B$ drift appears to be directed outward within the higher temperature spots.

In the low field side area, the $E \times B$ drift shifts hotter plasma outward, heating the plasma at the edge and amplifying there the initial temperature perturbation. In such a way an ITG instability develops in this area. On the contrary, at the high field side, the $E \times B$ moves colder plasma towards the core, suppressing in such a way the initial temperature perturbation.

Stability of the temperature gradient driven modes are affected by the development of the zonal structures, which act as a sink of the turbulent energy and can increase the temperature gradient threshold of the toroidal ITG mode excitation. Mutual development of the ITG and ZS can be demonstrated by using so-called reduced models (0-D models), where the ITG-ZS interaction is considered as a predator-prey system [44, 45, 46]. More precisely, the ITG mode, which develops due to the presence of the background temperature gradient, plays the role of the prey, while the ZS acts as a predator by taking energy from the unstable ITG mode. As a result, the presence of the ZS leads to the ITG stabilisation, lowering the turbulence level and reducing radial plasma transport, improving in such a way the plasma confinement.

Nonlinear excitation of zero-frequency zonal flows by ITG modes can be described by using the principle of a modulational instability [45, 47, 46], which is a variant of the parametric instability (Chapter 8 in [48]), but with a four-waves coupling instead of the three-waves one. In case of the modulation instability, a pump wave with a high frequency is modulated by a low-frequency wave. Because of the coupling of the primary modes, two beat (or also called sideband) modes are excited, and by the interaction with the pump fast varying wave, the sidebands amplify the initial

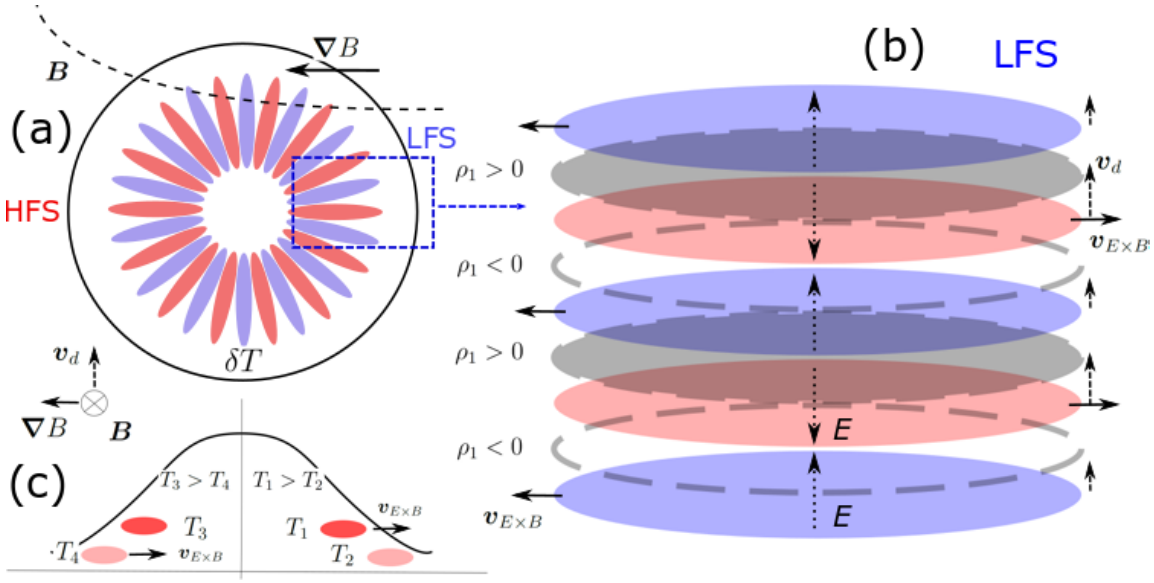

Figure 1.5: Cartoon of a toroidal ITG excitation. Plot (a): a poloidal plasma cross-section with an initial temperature perturbation. The red spots are domains with a higher temperature, while the blue ones are with a lower temperature. Plot (b): zoom of the low field side. Different amplitudes of the drift velocity v_d in the hot (red) and cold (blue) spots cause density ion perturbation ρ_1, which in its turn leads to the outward $E \times B$ drift $v_{E\times B}$ of the hotter plasma. Plot (c): $E \times B$ drift amplifies the initial temperature perturbation at the LFS, and suppresses it at the HFS.

modulation, which is the slow varying wave. If an ITG-ZF system is considered, an ITG with a toroidal mode number n, a radial wavenumber $k_{r,DW}$ and a frequency ω_{DW} plays the role of a pump wave. A ZF, which has a zero toroidal mode $n = 0$, a higher radial wavenumber $k_{r,ZF} > k_{r,DW}$ and a much lower frequency $\omega_{ZF} \ll \omega_{DW}$, modulates the ITG mode. As a result, two sidebands $(n, k_{r,DW} - k_{r,ZF}, \omega_{DW} \pm \omega_{ZF})$ are excited. According to [45], the ZF growth rate in this process is linearly proportional to the amplitude of the pump ITG:

$$\gamma_{ZF} \sim \Phi_{ITG}. \tag{1.55}$$

The excited sidebands are just other ITG modes with the same toroidal mode number, a similar frequency, but with an increased radial wavenumber, since $k_{r,ZF} > k_{r,DW}$. In other words, the ZF reduces the radial wavelength of the initial ITG. Since the electric potential related to the ITG has a finite poloidal wavenumber, there is a significant poloidal component of the electric field $\mathbf{E}_{pol}$. Due to the $\mathbf{E}_{pol} \times \mathbf{B}_{tor}$

drift and a long radial wavelength of the ITG, plasma vortices appear, where particles can move from the core of the toroidal plasma system close to the edge of the tokamak. Excitation of the ZF shears these eddies and decreases in such a way the radial correlation length of the radial transport.

Geodesic acoustic modes can be driven by ITG modes through the parametric instability, which deals with a three-waves coupling. In this process, there is again one pump mode (the ITG) and a modulation (the GAM). The main difference is that due to the finite GAM frequency, the pump mode can couple with only one sideband. However, according to this theory [16, 17], the GAM growth rate is also linearly proportional to the amplitude of the initial ITG mode (Eq. 1.55).

1.6 Contribution and outline of the thesis

The zonal structures, and in particular the geodesic acoustic modes, play an essential role in the plasma self-organisation and energy transfer between different modes, and between plasma particles and the electromagnetic fields. The development of these phenomena might significantly depend on the plasma regimes, including magnetic field geometry and electron kinetic effects. It is challenging to describe such a complex system by using only analytical theories. For this reason, one has to use numerical methods based on gyrokinetic models, to study the wave evolution in the tokamak plasma. One can include background magnetic field configuration, species density and temperature profiles reconstructed directly from an investigated experimental discharge. Moreover, one can include or eliminate different pieces of plasma physics, such as magnetic field perturbations, kinetic electrons, or ion finite Larmor radius effects. By providing up-to-date results from the numerical simulations, one can contribute to the development of comprehensive theoretical models of the geodesic modes. A good example is the development of the analytical theory of the GAM damping by trapped electrons [35]. This phenomenon was mentioned and analysed for the first time in [32], while the significance of the electron Landau damping in experimentally relevant configurations was confirmed numerically in the code ORB5 in the framework of this thesis [34], and consequently, in other European GK codes as well (see, for example, [36]).

For a better understanding of the material presented in this work, the analytical derivation of the GAM dispersion relation is shown in Chapter 3. However, the central part of this thesis is based on results obtained from gyrokinetic simulations in the global particle-in-cell (PIC) code ORB5 described in Chapter 2.

The main goal of this thesis is the numerical investigation of the damping and excitation mechanisms of the geodesic acoustic modes in simplified and realistic mag-

netic configurations. The use of the simplified geometry allows performing a comparison with analytical theories, while the realistic configurations are simulated for the comparison with experimental measurements. Several main lines of this work can be defined: (E)GAM damping by electrons in ASDEX Upgrade (Chapter 4 and Chapter 6), implementation of a power balance diagnostic in velocity space to localise the mode - particle resonances (Chapter 5), investigation of plasma heating by the geodesic modes driven by energetic particles in AUG magnetic configuration (Chapter 7), and finally, a numerical study of the nonlinear GAM excitation by ITG instabilities in AUG and TCV magnetic configurations (Chapter 8).

The geodesic modes are observed predominantly in the edge region of the tokamak plasmas (this is because the GAM damping scales proportionally to $\exp(-q^2)$ and the safety factor q is the largest at the plasma edge, see Eq. 4.2) with a characteristic frequency of the order of the sound frequency $\sim c_s/R$, where $c_s = \sqrt{T_e/m_i}$ is the sound speed, T_e is the electron temperature. However, the mode frequency depends also on the safety factor profile, the mode radial wavenumber, the shape of the magnetic configuration (elongation), the electron-ion temperature ratio to name a few. The GAM frequency and damping rate are numerically investigated in Chapter 4. The main part of this chapter is dedicated to the Landau damping of the GAMs due to the mode interaction with the electrons. It is shown that the inclusion of the electron dynamics can significantly increase the mode damping rate in a realistic AUG magnetic configuration (Sec. 4.1). Contribution of the phase mixing is presented in Sec. 4.2, while the collisional damping is discussed in Sec. 4.3. The GAM linear frequency and damping rate spectra in AUG are numerically estimated in Sec. 4.4.

To illustrate that the electron damping of the geodesic modes takes place mainly due to the wave interaction with barely trapped electrons, we implement a *Mode-Particle-Resonance* (MPR) diagnostic in the code ORB5 and analytically verify it by the GAM dispersion relation, as it is described in Chapter 5. The diagnostic is used to analyse EGAM excitation by energetic particles (EPs) and damping by thermal species in AUG discharge in Chapter 6. It is demonstrated that the electrons localised near the passing-trapped boundary have sufficiently low characteristic velocities to resonate with the geodesic mode (Sec. 6.2).

The second part of this work is dedicated to the study of the nonlinear EGAM dynamics in AUG without considering the mode interaction with turbulence (Chapter 7). One of the most prominent phenomena related to the nonlinear EGAM evolution in tokamak plasmas is the mode chirping, where the evolution of the mode frequency in time is observed. In a chosen AUG discharge, the experimental EGAM spectrogram exhibits a clear mode up-chirping. Numerical simulations of the EGAM

chirping is a demanding task since the mode dynamics depends not only on the imposed thermal plasma configuration but on the EP parameters as well. Despite the approximation taken here on the EP distribution function, a clear EGAM up-chirping is obtained in the GK simulation, discussed in Sec. 7.2, where the relative change of the mode frequency is comparable to the experimental results.

Plasma heating by EGAMs is analysed in the same AUG plasma system in Sec. 7.1. During this process, the EGAM plays the role of an intermediate agent between energetic and thermal particles by transferring kinetic energy from the EPs to the bulk (thermal) plasma. It is demonstrated that by varying the EP parameters, one can enhance the plasma heating by the EGAM, keeping the mode amplitude at the same level. By performing simulations with drift-kinetic electrons, it is discussed in Sec.7.1 that the EGAMs transfer the EP energy directly to the thermal ions. At the same time, it is known that the EP-plasma collisional processes lead mainly to the electron plasma heating if the EPs are not enough slowed down (Sec. 7.3). On the other hand, it is shown that although electrons are not the primary recipients of the EGAM energy, they can significantly reduce the mode amplitude and, in such a way, decrease the plasma heating by the mode.

The final part of this work is dedicated to the nonlinear GAM excitation by the ITG drift instabilities. The GAMs can have different kinds of the frequency spectrum: continuum, or global one (Chapter 8). In linear and generally in nonlinear systems, the mode has a continuum frequency spectrum. In other words, because of the radial temperature and magnetic field profiles, the mode oscillates with different frequencies at different radial positions. Such kind of GAM spectrum is predicted by linear analytical theories [28, 29, 30] and is obtained here in Sec. 4.4. However, the global GAM spectrum was observed experimentally, for example, in AUG discharges [49], and in the DIII-D tokamak [50]. In this regime, the mode can have a constant frequency within a significant radial interval disregarding the change of the plasma temperature and magnetic field radial profiles. It was discussed in [51] that the toroidal plasma rotation might give rise to the global GAM spectrum. In [52], it was numerically shown that the transition from the continuum to the global regime might be subject to a combination of different plasma parameters such as species profiles, collisionality, magnetic field configuration, and kinetic electron effects. A global spectrum of a GAM-like structure was also numerically investigated in the TCV magnetic field configuration [53], where the transition takes place with the increase of the plasma temperature gradient at the edge of the tokamak. However, since the resulting global frequency extended in a long radial interval was significantly smaller than the GAM frequency predicted by linear analytical theories, the nature of the observed mode is still under investigation. Nonlinear gyrokinetic simulations

of the GAM spectra in AUG and TCV magnetic configurations are presented in Chapter 8. It is shown that the non-zonal modes with high toroidal mode numbers are crucial for the formation of the global zonal structures, and for the numerical computation of the nonlinear GAM frequency spectrum in general. This proves that the generation of global GAM structures is a nonlinear process.

Chapter 2

Numerical gyrokinetic model

Gyrokinetic (GK) codes have recently become standard tools for the investigation of waves and instabilities in the tokamak plasmas, with frequencies well below the ion cyclotron frequency [54]. Although they have been traditionally considered numerically heavy, in comparison to lighter hybrid models, in the last years GK codes have become capable of providing global electromagnetic (EM) predictions of the nonlinear plasma dynamics, thanks to smart schemes improving the numerical performance [55, 56], and to the access to high-performance computers. One advantage of using GK codes is that their model includes kinetic effects such as wave-particle resonances, which are neglected in fluid descriptions.

The gyrokinetic simulations presented in this work are performed with the code ORB5 [25, 26, 27], which is a nonlinear gyrokinetic multi-species global particle-in-cell (PIC) code. It solves the gyrokinetic Vlasov-Maxwell system described below in the electrostatic or electromagnetic limit, and has a capability of handling true MHD equilibrium for the axisymmetric toroidal plasma. In this chapter, we are going to consider different numerical and theoretical aspects of this code. The physical model of ORB5 is derived from a variational principle [26, 57] to provide exact energy and momentum conservation, and is discussed in Sec. 2.1. The particle-in-cell method, which is presented in Sec. 2.2, consists of the coupling of a particle-based algorithm for the Vlasov equation with a grid-based method for the computation of the self-consistent electromagnetic fields. Finally, due to the variational formulation, one can implement a power balance diagnostic to investigate the wave-particle interaction in the code [26, 57] that is discussed in Sec. 2.3. This diagnostic is extended in this work [58] to localise resonances of the wave-particle interaction in velocity space, and its implementation is described in Chapter 5.

2.1 Hamiltonian formulation

The GK Vlasov-Maxwell model implemented in ORB5 is derived from a variational principle. This approach directly provides a weak form of the GK Poisson and Ampère equations, which is used in the code for the finite element representation of the electromagnetic fields with the B-spline basis functions [27]. According to the ORB5 model, all the geometrical effects due to the non-uniformity of the background magnetic field are considered one order smaller than the relative fluctuations of the fields as it is explained in [57]. The corresponding parameter of smallness for the background magnetic field non-uniformity is

$$\varepsilon_B = \frac{\rho_{th,i}}{L_B}, \tag{2.1}$$

where L_b is the characteristic length of the background magnetic field gradient. Another small parameter

$$\epsilon_\delta = (k_\perp \rho_{th,i}) \frac{e\Phi}{T_i}, \tag{2.2}$$

is related to the field perturbations, where Φ is the electric potential perturbation ($\mathbf{E} = -\boldsymbol{\nabla}\Phi$), $k_\perp \rho_{th,i}$ is the normalised perpendicular (to the magnetic field) wavenumber, T_i is the thermal ion temperature. Due to the chosen approximation, we have $\varepsilon_B \sim \epsilon_\delta^2$, which is currently a common approach in most GK codes.

To derive the GK Vlasov-Maxwell system of equations, first of all, one has to decouple the fast dynamics associated with the gyrorotation of particles from the low-frequency dynamics of interest. This procedure, called phase space reduction or gyrokinetic dynamical reduction, restores to all considered orders the conservation of the adiabatic invariant μ_{sp} related to the fast gyromotion, broken by the effects of the magnetic field non-uniformity and electromagnetic perturbations (see, for example, [59]). As a result, the phase space coordinates are reduced from six to $4+1$, where the plasma system dynamics is restricted to the surface $\dot{\mu}_{sp} = 0$.

The field-particle action obtained after the phase space reduction is accurate up to $\mathcal{O}(\epsilon_\delta^2)$:

$$\begin{aligned} \mathcal{A} \;=\; & \int \mathrm{d}t \mathcal{L} = \\ & \sum_{sp} \int \mathrm{d}t\, \mathrm{d}V\, \mathrm{d}W_{sp} \left(\frac{Z_{sp}e}{c} \mathbf{A}^* \cdot \dot{\mathbf{R}} + \frac{m_{sp}c}{Z_{sp}e} \mu_{sp} \dot{\theta} - H_{0,sp} - H_{1,sp} \right) f_{sp} \\ & - \sum_{sp} \int \mathrm{d}t\, \mathrm{d}V\, \mathrm{d}W_{sp} f_{0,sp} H_{2,sp} - \int \mathrm{d}t\, \mathrm{d}V \frac{|\nabla_\perp A_\parallel|^2}{8\pi} \end{aligned} \tag{2.3}$$

Here, the velocity variables are the magnetic moment

$$\mu_{sp} = \frac{m_{sp} v_{\perp,sp}^2}{2B}, \tag{2.4}$$

the canonical parallel momentum $p_{z,sp}$ (see Eq. 2.10) and the gyroangle θ_{sp} of the particle species. For the sake of clearness, farther in the text, we omit the subindex sp, where it is possible. The equilibrium magnetic field is $\boldsymbol{B} = \nabla \times \boldsymbol{A}$, m is the species mass. The integration is performed over the real V and velocity W spaces. The volume element of the velocity space is

$$\mathrm{d}W \equiv (2\pi/m^2) B_\parallel^* \, \mathrm{d}p_z \, \mathrm{d}\mu \tag{2.5}$$

with

$$B_\parallel^* = \boldsymbol{B^*} \cdot \boldsymbol{b}, \tag{2.6}$$

$$\boldsymbol{b} = \boldsymbol{B}/B, \tag{2.7}$$

$$\boldsymbol{B^*} = \boldsymbol{\nabla} \times \mathbf{A}^* = \boldsymbol{B} + \frac{p_z c}{Ze} \nabla \times \boldsymbol{b}, \tag{2.8}$$

$$\mathbf{A}^* = \mathbf{A} + \frac{c}{Ze} p_z \mathbf{b}. \tag{2.9}$$

$\mathrm{d}V$ denotes the volume element in the real space. $f(\mathbf{r}, p_z, \mu, t) = f_0(\mathbf{r}, p_z, \mu) + \delta f(\mathbf{r}, p_z, \mu, t)$ is the species distribution function, where we assume it is only the perturbed part that depends on the time. However, no direct assumptions on the amplitude of the perturbation are applied. The action $\mathcal{A}$ is derived using the p_z-formulation, also called *Hamiltonian formulation*, where we take

$$p_z = m v_\parallel + \frac{Ze}{c} J_0 A_\parallel \tag{2.10}$$

as a canonical momentum coordinate, J_0 is the gyroaverage operator (see Eq. 2.16). Due to that, the magnetic potential perturbation $A_\parallel$ is transferred from the symplectic part of the particle action (part of the action in front of the $\dot{\boldsymbol{R}}$ and $\dot{\theta}$) to the Hamiltonian one (see, for example, Section 2.D in [57], or Section 2 in [59]). In such a way, one avoids the explicit dependence of the particle momentum characteristic $\dot{p}_z$ on the partial time derivative of the magnetic potential perturbation $\partial_t A_\parallel$, and due to that, the code can use an explicit time solver. The trade-off is the appearance of the so-called *cancellation problem*, which takes place due to the incomplete cancellation of non-physical terms in the Ampère equation. During long time, this problem has constrained electromagnetic simulations to low beta cases $\beta_e < \sqrt{m_e/m_i}$ with

$$\beta_e = \frac{4\pi \langle n_e \rangle T_e}{B_0^2}, \tag{2.11}$$

being the ratio between the electron plasma and magnetic pressures, and where $\langle n_e \rangle$ is the volume-averaged electron density, B_0 is the magnetic field at the magnetic axis. Currently, this problem can be mitigated either by the enhanced control variates procedure [55] or by the so-called pullback method [60].

The system Hamiltonian contains up to $\mathcal{O}(\epsilon_\delta^2)$ terms

$$
\begin{aligned}
H &= H_0 + H_1 + H_2 && (2.12)\\
H_0 &= \frac{p_z^2}{2m} + \mu B, && (2.13)\\
H_1 &= Ze(J_0\Phi - \frac{p_z}{mc} J_0 A_\parallel), && (2.14)\\
H_2 &= \frac{(Ze)^2}{2mc^2}(J_0 A_\parallel)^2 - \frac{mc^2}{2B^2}|\nabla_\perp \Phi|^2. && (2.15)
\end{aligned}
$$

The first two integrals in the total Lagrangian define the charged particle Lagrangian as in [61]. The third one is the electromagnetic field Lagrangian, in which the electric field component is neglected in comparison to the $E \times B$ energy from H_2 (the quasi-neutrality approximation, see [26] for details). Finally, the perpendicular magnetic potential perturbation is considered one order smaller than the parallel component and is omitted from the GK modelling. In other words, the magnetic compressibility is not taken into account, which however might be important in high beta systems.

The gyroaveraging (Hermitian) operator J_0, applied to an arbitrary function ψ in configuration space, is defined by

$$
(J_0\psi)(\mathbf{R}, \mu) = \frac{1}{2\pi} \int_0^{2\pi} \psi(\mathbf{R} + \boldsymbol{\rho}(\theta))\, \mathrm{d}\theta, \tag{2.16}
$$

where $\boldsymbol{R}$ is the position of the guiding center, and $\boldsymbol{\rho}$ is the vector going from the guiding center to the particle position. In the so-called *drift-kinetic approximation*, the potential perturbation is taken at the space point $\boldsymbol{R}$, where the guiding center of a considered numerical particle is localised, and the field is not gyro-averaged around the guiding center position as it is done in Eq. 2.16. In other words, the drift-kinetic approximation applies $J_{0,sp} = 1$. In the simulations presented in this thesis, ORB5 treats thermal and fast (energetic) ions either gyro-kinetically or drift-kinetically, while the electrons are calculated drift-kinetically or adiabatically.

The gyrokinetic equations for the particle distribution function and the GK field equations are derived from the GK Lagrangian using a variational principle. In gen-

eral, by taking a functional derivative of the system Lagrangian $\mathcal{L} = \int \mathrm{d}V\,\mathrm{d}W L(\eta, \delta\eta)$

$$\frac{\delta\mathcal{L}}{\delta\eta}\chi = \frac{\mathrm{d}}{\mathrm{d}\nu}\int L(\eta+\nu\chi, \nabla\eta+\nu\nabla\chi)\,\mathrm{d}V\,\mathrm{d}W\big|_{\nu=0} = \tag{2.17}$$

$$\int \frac{\delta L}{\delta\eta}\chi\,\mathrm{d}V\,\mathrm{d}W + \int \frac{\delta L}{\delta\nabla\eta}\cdot\nabla\chi\,\mathrm{d}V\,\mathrm{d}W = \tag{2.18}$$

$$\int\left(\frac{\delta L}{\delta\eta} - \nabla\cdot\frac{\delta L}{\delta\nabla\eta}\right)\chi\,\mathrm{d}V\,\mathrm{d}W + \int\nabla\cdot\left(\frac{\delta L}{\delta\nabla\eta}\chi\right)\mathrm{d}V\,\mathrm{d}W, \tag{2.19}$$

one gets a weak form (Eq. 2.18) of a physical equation, which is used for the finite element representation of the EM field potentials. Apart from that, one can obtain a strong form of the equation (Eq. 2.19). It has a dynamical term (first integral), which gives the equations of motion, and a Noether term (second integral), which is used to get conservation laws of the system. By taking the electric potential perturbation Φ as the test function χ, one gets the polarization (Poisson) equation in the long wave-length limit

$$\sum_i \int \mathrm{d}W_i Z_i e J_{0,i} f_i - \int \mathrm{d}W_e e f_e = -\sum_i \nabla\cdot\left(\frac{n_{0,i}m_i c^2}{B^2}\nabla_\perp\Phi\right). \tag{2.20}$$

By taking $A_\parallel$ as the test function, one gets the Ampère equation

$$\sum_i \int \mathrm{d}W_i \frac{4\pi Z_i e}{m_i c} p_{z,i} J_{0,i} f_i - \int \mathrm{d}W_e \frac{4\pi e}{m_e c} p_{z,e} f_e = \tag{2.21}$$

$$\frac{1}{d_e^2}A_\parallel - \nabla_\perp^2 A_\parallel + \sum_i\left(\nabla\cdot\frac{\pi n_{0,i}T_i}{B^2}\nabla_\perp A_\parallel + \frac{1}{d_i^2}A_\parallel\right),$$

where n_0 is the density associated with the equilibrium Maxwellian f_0. The skin depth is defined by $d^{-2} = 4\pi n_0 (Ze)^2/(mc^2)$, and it appears on the right-hand-side of the Ampère's law because of the choice of the velocity space variables (p_z, μ) instead of the usual $(v_\parallel, \mu)$, and causes the cancellation problem mentioned before. The indexes i and e indicate ions and electrons respectively.

First of all, one can notice on the right hand sides of the both field equations that the polarization and magnetization terms are calculated through the equilibrium plasma density n_0. Such kind of linearisation follows from the approximation made in the second integral of the field-particle action Eq. 2.3, where the second order Hamiltonian H_2 is considered together with only the equilibrium distribution function f_0[1]. Moreover, since we take the equilibrium distribution function in the Maxwellian

[1] In fluid theory this is called the Boussinesq approximation. It assumes that density variations are small, and they are neglected to reduce the nonlinearity of the problem.

form, the field equations are decoupled. These assumptions might get invalid if the magnitude of the distribution perturbation becomes comparable with that of the equilibrium distribution function. Moreover, if we want to consider a realistic energetic particle distribution function, which is asymmetric in velocity space, the Poisson and Ampère equations can become coupled in this case as well.

By taking the particle reduced phase space coordinates $\mathbf{Z} = (\mathbf{R}, p_z, \mu)$ as the test functions, one gets particle equations of motion, also called *particle characteristics*:

$$\dot{\mathbf{R}} = \frac{c\mathbf{b}}{ZeB_{\parallel}^{*}} \times \boldsymbol{\nabla}(H_0 + H_1) + \frac{\partial(H_0 + H_1)}{\partial p_z}\frac{\mathbf{B}^{*}}{B_{\parallel}^{*}}, \tag{2.22}$$

$$\dot{p}_z = -\frac{\mathbf{B}^{*}}{B_{\parallel}^{*}} \cdot \boldsymbol{\nabla}(H_0 + H_1), \tag{2.23}$$

$$\dot{\mu} = 0. \tag{2.24}$$

Again, due to the $f_0 H_2$ approximation, one gets rid of the H_2-dependence in the particle characteristics. In the electrostatic case, the characteristics can be split in the following terms:

$$\dot{\mathbf{R}} = \boldsymbol{v}_{\parallel} + \boldsymbol{v}_{\nabla B} + \boldsymbol{v}_{curvB} + \boldsymbol{v}_{\nabla p} + \boldsymbol{v}_{E\times B}, \tag{2.25}$$

$$\dot{p}_z = -\frac{m}{p_z}(\boldsymbol{v}_{\parallel} + \boldsymbol{v}_{\nabla p} + \boldsymbol{v}_{curvB}) \cdot \boldsymbol{\nabla}(\mu B + Ze(J_0\Phi)), \tag{2.26}$$

with

$$\boldsymbol{v}_{\parallel} = \frac{p_z}{m}\mathbf{b}, \tag{2.27}$$

$$\boldsymbol{v}_{\nabla B} = \frac{c\mu B}{ZeB_{\parallel}^{*}}\mathbf{b} \times \frac{\boldsymbol{\nabla} B}{B}, \tag{2.28}$$

$$\boldsymbol{v}_{curvB} = \left(\frac{p_z}{m}\right)^2 \frac{cm}{ZeB_{\parallel}^{*}}\mathbf{b} \times \frac{\boldsymbol{\nabla} B}{B}, \tag{2.29}$$

$$\boldsymbol{v}_{\nabla p} = -\left(\frac{p_z}{m}\right)^2 \frac{cm}{ZeB_{\parallel}^{*}}\mathbf{b} \times \left(\mathbf{b} \times \frac{\boldsymbol{\nabla} \times \mathbf{B}}{B}\right), \tag{2.30}$$

$$\boldsymbol{v}_{E\times B} = -\frac{c\boldsymbol{\nabla}(J_0\Phi) \times \mathbf{b}}{B_{\parallel}^{*}}, \tag{2.31}$$

where $\mathbf{b} \times (\boldsymbol{\nabla} \times \mathbf{B})/B = -4\pi\boldsymbol{\nabla} p/B^2$ (obtained by using Eqs. 1.20, 1.9) in Eq. 2.30 indicates the dependence on the pressure gradient. Here, $\boldsymbol{v}_{\parallel}$ is the parallel velocity term, which is responsible, for example, for the magnetic mirror effect mentioned in

Sec. 1.2 (Eq. 1.14). The $\boldsymbol{v}_{\nabla B}$ and $\boldsymbol{v}_{curvB}$ can be combined into the magnetic drift velocity (Eq. 1.54) associated with the corresponding frequency indicated in Eq. 3.19. The diamagnetic drift $\boldsymbol{v}_{\nabla p}$ gives rise to the drift waves due to the temperature and density gradients [42]. Finally, the $\boldsymbol{v}_{E\times B}$ term is one of the main nonlinear terms of the particle characteristics. Using these particle equations of motion, the code can reconstruct the gyrokinetic Vlasov equation:

$$\frac{\mathrm{d}f}{\mathrm{d}t} = \frac{\partial f}{\partial t} + \dot{\boldsymbol{R}} \cdot \nabla f + \dot{p}_z \frac{\partial f}{\partial p_z} = 0. \tag{2.32}$$

Despite all the approximations made here, this model is highly physically relevant and it can be used to describe not only the ZS dynamics, but also a large class of microinstabilities excited by the density and temperature gradients, like Ion Temperature Gradient (ITG) driven modes, Trapped Electron Modes (TEM) or Kinetic Ballooning Modes (KBM). It also contains the reduced MHD model as a subset (see, among other, [62]).

2.2 The Particle-In-Cell (PIC) code

ORB5 is the particle-in-cell (PIC) code, where the Vlasov equation is solved using the Monte Carlo algorithm, and the Maxwell equations are solved using the finite-element method. According to the PIC method, the particle distribution function is discretized with macroparticles, known as *markers*. The motion of the markers is calculated using the particle characteristics (Eqs. 2.22, 2.23) of the gyrokinetic model while the electromagnetic fields are evolved on the spatial grid using the two decoupled field equations (Eqs. 2.20, 2.21). The charge and current densities on the left hand sides of the field equations are calculated by projecting the marker weights on the spatial grid. After that, the fields are calculated using the finite element method. The code is based on the straight-field-line coordinate system (s, χ, ϕ)[2]. Here, the radial coordinate is $s = \sqrt{\psi/\psi_{edge}}$ (where ψ is the poloidal flux coordinate, Eq. 1.10), $\chi = \dfrac{1}{q(s)} \displaystyle\int_0^{\Theta} \frac{\mathbf{B}\cdot\nabla\phi}{\mathbf{B}\cdot\nabla\Theta_1} d\Theta_1$ is the straight-field-line coordinate (where Θ_1 is the poloidal angle), and ϕ is the toroidal angle. Two different kinds of magnetic equilibria are available to use: analytical equilibria with circular concentric magnetic surfaces and ideal MHD realistic equilibria. For the latter case, the ORB5 code is coupled with the CHEASE code [64], which solves the Grad-Shafranov equation with a fixed plasma boundary.

[2]The magnetic field lines appear as straight lines in this system of coordinates (one can see Chapter 6 in [63] for more details).

Now, we are going to consider the discretization of the plasma distribution function in the code that will be necessary later on to describe the numerical implementation of the Mode-Particle-Resonance diagnostic (Chapter 5). At the beginning of every simulation, a finite collection of initial positions in phase space is sampled by a set of numerical markers [26]. Every marker has a particular magnetic moment μ, a position in real space $\mathbf{R}$, a canonical momentum p_z and it is moving in a background magnetic field $\mathbf{B} = \mathbf{b}B$. Taking the phase-space position $\boldsymbol{Z} = (\mathbf{R}, p_z, \mu)$ of a species marker as a random variable, the code distributes the markers in the phase space according to the initial particle distribution function f_0. This means that every marker is the realisation of the random variable Z. For simplicity, the marker is considered as a particle that is moving along a particular orbit defined by the set of equations of motion shown in Eqs. 2.22, 2.23, 2.24. In the gyrokinetic approximation, the code deals with the dynamics of the guiding centres, whose orbits are perturbed by the field potentials, averaged along the Larmor orbit, around the marker position. The time evolution of the plasma distribution function f is described by the Vlasov equation presented in Eq. 2.32. Considering perturbations of the distribution function and of the particle orbits up to the first order, one can linearize the Vlasov equation:

$$\begin{aligned}\frac{\mathrm{d}\delta f}{\mathrm{d}t} &= \frac{\partial \delta f}{\partial t} + \dot{\mathbf{R}}_{\mathbf{0}} \cdot \boldsymbol{\nabla}\delta f + \dot{p}_{0,z}\frac{\partial \delta f}{\partial p_z} = \\ &- \left(\frac{\partial f_0}{\partial t} + \dot{\mathbf{R}}_{\mathbf{0}} \cdot \boldsymbol{\nabla} f_0 + \dot{p}_{0,z}\frac{\partial f_0}{\partial p_z}\right) \\ &- \left(\dot{\mathbf{R}}_{\mathbf{1}} \cdot \boldsymbol{\nabla} f_0 + \dot{p}_{1,z}\frac{\partial f_0}{\partial p_z}\right). \end{aligned} \tag{2.33}$$

Assuming that f_0 is the equilibrium distribution function, it should be conserved along unperturbed particle trajectories $(\dot{\mathbf{R}}_{\mathbf{0}}, \dot{p}_{0,z})$ according to the Liouville's theorem:

$$\left.\frac{\mathrm{d}f_0}{\mathrm{d}t}\right|_0 = \frac{\partial f_0}{\partial t} + \dot{\mathbf{R}}_{\mathbf{0}} \cdot \boldsymbol{\nabla} f_0 + \dot{p}_{0,z}\frac{\partial f_0}{\partial p_z} = 0. \tag{2.34}$$

In other words, the first bracket on the right hand side of Eq. 2.33 is equal to zero. Finally, the evolution in time of the perturbation of the species distribution function in linear simulations is described in the following way:

$$\frac{\mathrm{d}\delta f}{\mathrm{d}t} = \left.\frac{\mathrm{d}\delta f}{\mathrm{d}t}\right|_0 = -\left.\frac{\mathrm{d}f_0}{\mathrm{d}t}\right|_1, \tag{2.35}$$

where $\Big|_1$ indicates that it is necessary to take derivatives along the perturbed parts of the species orbits $(\dot{\mathbf{R}}_{\mathbf{1}}, \dot{p}_{1,z})$. Thermal species have an equilibrium distribution

function in a form of the Maxwellian one:

$$f_0^{therm} = \frac{n(\psi)}{(2\pi)^{3/2} v_{th}^3(\psi)} \exp\left[-\frac{m}{T(\psi)}\left(\frac{1}{2}\left(\frac{p_z}{m}\right)^2 + \frac{\mu B}{m}\right)\right], \tag{2.36}$$

$$v_{th}(\psi) = \sqrt{\frac{T(\psi)}{m}}, \tag{2.37}$$

where $n(\psi)$, $T(\psi)$ are species density and temperature profiles along the radial coordinate ψ. On the other hand, to describe energetic particles we are going to use a symmetric two-bumps-on-tail distribution function as in [65, 38]. This distribution assumes a flat temperature profile of the energetic species:

$$f_0^{EP} = A(\psi) \exp\left[-\frac{m}{T_H}\left(\frac{1}{2}\left(\frac{p_z}{m}\right)^2 + \frac{\mu B}{m}\right) - \frac{u_H^2}{2T_H}\right] \cosh\left(\frac{p_z}{m}\frac{u_H}{T_H}\right), \tag{2.38}$$

$$A(\psi) = \frac{n(\psi)}{(2\pi)^{3/2} T_H^{3/2}}, \tag{2.39}$$

where u_H, T_H are constant input parameters, which specify a shift and width of the energetic bumps respectively in velocity space. Typical thermal and energetic ion distribution functions are shown in Fig. 7.2[3]. A distribution function with two symmetric bumps-on-tail, instead of a single bump, is used to avoid input of additional momentum into the plasma system, which can change the EGAM frequency, and as a result, shift the position of the resonance between the EGAM and fast species.

The perturbation δf is discretized in the $Z = (\mathbf{R}, p_z, \mu)$ phase space by N markers. Apart from its location Z, every marker has a particular weight $w_p(t)$, which should evolve consistently with the GK Vlasov equation Eq. 2.32. Here, we use the index p, indicating that a variable is related to a particular marker. Detailed derivation of the weight time evolution can be found in [25, 26, 27, 66]. A marker weight can be associated to a phase space volume Ω_p and correspondent averaged distribution function perturbation $\langle \delta f \rangle_{\Omega_p}$:

$$\langle \delta f \rangle_{\Omega_p} = \frac{1}{\Omega_p} \int_{\Omega_p} \delta f \, \mathrm{d}\Omega_p = \frac{1}{\Omega_p} \int_{\Omega_p} w_p \delta(\mathbf{R} - \mathbf{R}_p) \delta(p_z - p_{p,z}) \, \mathrm{d}\Omega_p, \tag{2.40}$$

$$w_p(t) = \langle \delta f \rangle_{\Omega_p} \Omega_p, \tag{2.41}$$

$$\lim_{\Omega_p \to 0} \langle \delta f \rangle_{\Omega_p} \to \delta f(\boldsymbol{R}_p, v_{p,\parallel}, \mu_p). \tag{2.42}$$

[3]Note that these distribution functions are not strictly equilibrium distribution functions. This means they do not satisfy Eq. 2.34 because of the radial dependence of the density and temperature (and because of the $v_\parallel$-dependence in the case of the bump-on-tail distribution function). However, this radial (and velocity) variation is slow, and can be neglected as compared to the fast δf evolution (see, for example, Sec. 3.2 in [38]).

Considering uniform spreading of the markers in real space and Maxwellian distribution in the velocity space, it can be shown, according to [66], that the phase space volume Ω_p, associated to a marker p, is

$$\Omega_p = \frac{B^*_{\parallel,p}}{B} v_{\perp,p} (\pi \kappa_v v_{th}(s))^2 \int_0^1 \bar{J}(s)\, \mathrm{d}s, \tag{2.43}$$

where $\bar{J}(s)$ is the flux-surface-averaged Jacobian, κ_v defines maximum value of the species parallel and perpendicular velocities, normalised to a species thermal speed $v_{th}(s) = \sqrt{T(s)/m}$, at every radial point s.

The meaning of the variable Ω_p can be explained proceeding directly from the Monte Carlo integration [26]. The expectation value of an arbitrary function $\zeta(\tilde{Z})$ is

$$E[\zeta(\tilde{Z})] = \int \zeta(z) f(z) dz, \tag{2.44}$$

where $\tilde{Z}$ is a random variable, distributed according to the function f. To minimize the variance of the function ζ, one can chose another distribution function $g(\tilde{Z})$, which does not vanish in the support of the distribution function f (the so-called importance sampling):

$$E[W(Z)\zeta(Z)] = \int \zeta(z) \frac{f(z)}{g(z)} g(z) dz. \tag{2.45}$$

In this case, speaking in terms of marker weights and using random variable Z, distributed with density g, the expectation value of the function $\zeta(\tilde{Z})$ is calculated as

$$E[\zeta(\tilde{Z})] = E[W(Z)\zeta(Z)] = \frac{1}{N} \sum_{p=1}^{N} w(Z_p)\zeta(Z_p), \tag{2.46}$$

$$w(Z_p) = \frac{f(Z_p)}{g(Z_p)} = f(Z_p)\Omega(Z_p), \tag{2.47}$$

that is consistent with Eq. 2.41. In other words, if we have a small amount of markers in a finite phase space volume, their weights will be increased in comparison to a domain where there are higher number of markers at the same phase space volume. More details can be found in [26]. Finally, the marker weights are normalised in the following way:

$$\frac{1}{N} \sum_{p=1}^{N} w_p = 1, \tag{2.48}$$

where the sum is performed over all markers in a working phase space domain VW of a species.

2.3 Power balance

By considering the Noether term in Eq. 2.19, in the ES limit, the total GK energy has the following form

$$\mathcal{E} = \sum_{sp} \int \mathrm{d}W \, \mathrm{d}V \, (f(H_0 + H_1) + f_0 H_2) \,, \tag{2.49}$$

where the kinetic part of the energy is

$$\mathcal{E}_k = \sum_{sp} \int \mathrm{d}W \, \mathrm{d}V (f H_0), \tag{2.50}$$

while the 'field' energy is

$$\mathcal{E}_f = \sum_{sp} \int \mathrm{d}W \, \mathrm{d}V (f H_1 + f_0 H_2) \tag{2.51}$$

Evaluating the time derivative of the kinetic energy $\mathcal{E}_k$, the energy transfer between the plasma and the field can be found as

$$\mathcal{P} = \frac{\mathrm{d}\mathcal{E}_k}{\mathrm{d}t} = -\sum_{sp} Ze \int \mathrm{d}V \, \mathrm{d}W f \dot{\mathbf{R}}_{\mathbf{0}} \cdot \boldsymbol{\nabla}(J_0 \Phi), \tag{2.52}$$

where $\dot{\mathbf{R}}_{\mathbf{0}}$ is the species unperturbed equation of motion. To obtain this equation, first of all, one writes explicitly the full time derivative of the kinetic energy:

$$\frac{\mathrm{d}\mathcal{E}_k}{\mathrm{d}t} = \sum_{sp} \int \mathrm{d}W \, \mathrm{d}V f \left(\frac{p_z}{m} \dot{p}_z + \mu \dot{\boldsymbol{R}} \cdot \boldsymbol{\nabla} B \right), \tag{2.53}$$

where we have taken into account the Vlasov equation $\mathrm{d}_t f = 0$, and the expression for the background Hamiltonian H_0 of a particle moving in the background magnetic field (Eq. 2.13). Using explicit expressions for the particle characteristics (Eqs. 2.25 and 2.26), and the following mathematical transformations

$$(\boldsymbol{\nabla}(J_0 \Phi) \times \boldsymbol{B}) \cdot \boldsymbol{\nabla} B = (\boldsymbol{B} \times \boldsymbol{\nabla} B) \cdot \boldsymbol{\nabla}(J_0 \Phi), \tag{2.54}$$

$$\boldsymbol{\nabla} \cdot \boldsymbol{b} = -\frac{\boldsymbol{b} \cdot \boldsymbol{\nabla} B}{B}, \tag{2.55}$$

one can combine two terms in Eq. 2.53 to get Eq. 2.52. Such a direct implementation of the particle characteristics leads to the cancellation of the field perturbations

in the particle orbits, and the resulting expression 2.52 is evaluated through the unperturbed particle orbit $\dot{\mathbf{R}}_\mathbf{0}$. The detailed derivation of the GK energy and the plasma-field energy transfer signal can be found in [26, 57]. It should be noted that the splitting on the 'kinetic' and the 'field' parts is in some sense arbitrary. In this work, we keep terms, which depend on the species characteristics, in the 'kinetic' part, and the rest of the total energy is taken as the 'field' component. More precisely, in the ES limit, using the GK Poisson equation, the total energy Eq. 2.49 can be transformed into the following form [26]

$$\mathcal{E} = \sum_{sp} \int \mathrm{d}W\, \mathrm{d}V \left(\frac{p_z^2}{2m} + \mu B + \frac{1}{2} Z e J_0 \Phi \right) f \tag{2.56}$$

Here, the first two terms correspond to Eq. 2.50, while the last term is related to Eq. 2.51.

The derived energy exchange and field energy signals can be used to estimate a field linear growth rate. Using Eq. 2.52 and the energy conservation, we obtain

$$\mathcal{P} = \sum_{sp} \mathcal{P}_{sp} = -\frac{\mathrm{d}\mathcal{E}_f}{\mathrm{d}t}, \tag{2.57}$$

$$\mathcal{E}_f = \sum_{sp} \frac{mc^2}{2B^2} \int \mathrm{d}V |\nabla_\perp \Phi|^2. \tag{2.58}$$

Here, the expression for the electric field energy $\mathcal{E}_f$ is obtained from Eq. 2.51 and the GK Poisson equation, by treating particles drift-kinetically (J_0 is equal to 1). Considering a general case of a propagating eigenmode and starting from the evolution of the electric field $\mathbf{E} = -\nabla\Phi$

$$\begin{gathered} \mathbf{E}(\mathbf{r}, t) = Re\left[\mathbf{E}(\mathbf{r}) \exp(-i\omega t) \exp(\gamma t)\right] = \\ (\cos(\omega t) Re[\mathbf{E}(\mathbf{r})] + \sin(\omega t) Im[\mathbf{E}(\mathbf{r})]) \exp(\gamma t) \end{gathered} \tag{2.59}$$

where ω, γ are the frequency and damping/growth rate of the field, we get an expression for the field energy integrated in real space:

$$\mathcal{E}_f(t) = (A^2 + C\cos^2(\omega t)) \exp(2\gamma t), \tag{2.60}$$

with a constant C and non-zero constant A^2. Its time derivative is

$$\frac{\mathrm{d}\mathcal{E}_f}{\mathrm{d}t} = 2\gamma \mathcal{E}_f - \omega C \sin(2\omega t) \exp(2\gamma t). \tag{2.61}$$

Using the above equations, we can find the damping/growth rate of the field energy in the following way:

$$\frac{1}{2\mathcal{E}_f}\frac{\mathrm{d}\mathcal{E}_f}{\mathrm{d}t} = \gamma - \frac{\omega\sin(2\omega t)}{2A^2/C + 1 + \cos(2\omega t)}. \tag{2.62}$$

Due to the field energy oscillations that take place in the case of the GAMs and EGAMs, the above expression includes a term, which depends on the field frequency. To exclude this term, one should perform the time averaging on several periods of the field oscillations:

$$\int_0^{n_w T_w} \frac{\sin(2\omega t)}{2A^2/C + 1 + \cos(2\omega t)}\,\mathrm{d}t = 0, \tag{2.63}$$

where T is the period of the field oscillations, and n_w is the number of the periods. Due to that, the damping/growth rate of the field can be calculated using the following expression:

$$\gamma = -\frac{1}{2}\frac{1}{n_w T_w}\int_0^{n_w T_w} \frac{\mathcal{P}}{\mathcal{E}_f}\,\mathrm{d}t. \tag{2.64}$$

A negative rate $\gamma < 0$ corresponds to a positive signal $\mathcal{P}$, indicating the energy transfer from the wave to the plasma particles. On the other hand, a positive rate $\gamma > 0$ corresponds to a growth of the wave. It should be noted that the GAMs or EGAMs can take the form of a standing wave, which is a limiting case of the propagating wave, where $2A^2/C \to \varepsilon$ with a positive infinitesimally small value $\varepsilon > 0$:

$$\int_0^{n_w T_w} \frac{\sin(2\omega t)}{(1+\varepsilon) + \cos(2\omega t)}\,\mathrm{d}t = 0. \tag{2.65}$$

Finally, note that in the case of a non-zonal mode with a non-zero toroidal number, the field energy would be a purely growing function that would simplify the problem by exempting us from the time integration in Eq. 2.64. In other words, by considering, for example, the ITG evolution, one does not have to perform the time averaging to calculate the growth rate of the non-zonal mode. The results presented in this section are used in Chapter 5, where the Mode-Particle-Resonance technique based on the presented power balance diagnostic is described.

Chapter 3

Gyrokinetic theory of GAMs

In this chapter, we would like to discuss in detail some aspects of the GAM dynamics introduced previously in Chapter 1. More precisely, we are going to derive a basic GAM dispersion relation in *deuterium* plasma ($Z_i = 1$) with *adiabatic electrons* in the so-called *electrostatic limit* ($A_\parallel = 0$, $p_z = mv_\parallel$), where only the electric potential perturbation is taken into account. The derivation is based on [67, 16, 24], and the results of this chapter will be used later in Sec. 5.3 for the analytical verification of the Mode-Particle-Resonance diagnostic.

3.1 Gyrokinetic equation

We start from a standard linear gyrokinetic equation assuming flat background density and temperature profiles (the corresponding gradients are equal to zero). In this section, we are going to omit the species subindex, since the derivation is the same for electrons and ions. To derive the GK equation, we consider the particle characteristics (Eqs. 2.25, 2.26)

$$\dot{\mathbf{R}} = \dot{\mathbf{R}}_0 + \dot{\mathbf{R}}_1, \quad \dot{p}_z = \dot{p}_{z,0} + \dot{p}_{z,1}, \tag{3.1}$$

$$\dot{\mathbf{R}}_0 = \boldsymbol{v}_\parallel + \boldsymbol{v}_{\nabla B} + \boldsymbol{v}_{curvB}, \tag{3.2}$$

$$\dot{\mathbf{R}}_1 = \boldsymbol{v}_{E\times B}, \tag{3.3}$$

$$\dot{p}_{z,0} = -\frac{\mu}{v_\parallel}(\boldsymbol{v}_\parallel + \boldsymbol{v}_{curvB}) \cdot \boldsymbol{\nabla} B, \tag{3.4}$$

$$\dot{p}_{z,1} = -\frac{Ze}{v_\parallel}(\boldsymbol{v}_\parallel + \boldsymbol{v}_{curvB}) \cdot \boldsymbol{\nabla} J_0 \Phi, \tag{3.5}$$

where J_0 is the gyroaveraging operator (see Eq. 2.16). The starting point is the Vlasov equation

$$\frac{\mathrm{d}\delta f}{\mathrm{d}t} = -\frac{\mathrm{d}f_0}{\mathrm{d}t} \tag{3.6}$$

with $f = f_0 + \delta f$, where the equibrium Maxwellian distribution function normalised to 1 (density $n = 1$) is taken as a function of the particle kinetic energy ϵ_{kin} (compare with Eq. 2.36)

$$f_0 = \frac{1}{(2\pi)^{3/2} v_{th}^3} \exp\left(-\frac{\epsilon_{kin}}{T}\right), \quad \epsilon_{kin} = \frac{p_z^2}{2m} + \mu B. \tag{3.7}$$

In this case, we obtain the following linearised Vlasov equation

$$\frac{\partial \delta f}{\partial t} + \dot{\boldsymbol{R}}_0 \cdot \boldsymbol{\nabla} \delta f + \dot{\epsilon}_{kin,0} \frac{\partial \delta f}{\partial \epsilon_{kin}} = -\dot{\epsilon}_{kin} \frac{\partial f_0}{\partial \epsilon_{kin}}, \tag{3.8}$$

where the full time derivative of the kinetic energy is

$$\dot{\epsilon}_{kin} = v_{\parallel} \dot{p}_z + \mu \dot{\boldsymbol{R}} \cdot \boldsymbol{\nabla} B. \tag{3.9}$$

The particle kinetic energy is conserved along the unperturbed particle trajectories. In other words, $\dot{\epsilon}_{kin,0} = 0$ that can be easily checked by inserting Eqs. 3.2, 3.4 into Eq. 3.9, and using the following expression

$$\boldsymbol{v}_{\nabla B} \cdot \boldsymbol{\nabla} B = 0. \tag{3.10}$$

As a result, the Vlasov equation is simplified to

$$\frac{\partial \delta f}{\partial t} + \dot{\boldsymbol{R}}_0 \cdot \boldsymbol{\nabla} \delta f = -\frac{\partial f_0}{\partial \epsilon_{kin}} v_{\parallel} \dot{p}_{z,1} - \frac{\partial f_0}{\partial \epsilon_{kin}} \mu \dot{\boldsymbol{R}}_1 \cdot \boldsymbol{\nabla} B, \tag{3.11}$$

To eliminate the terms on the right hand side of the above equation, we split the distribution perturbation function up into the adiabatic[1] and non-adiabatic[2] parts

$$\delta f = Ze\frac{\partial f_0}{\partial \epsilon_{kin}} J_0 \Phi + h, \tag{3.12}$$

and the Vlasov equation is transformed into

$$\begin{aligned} &\frac{\partial h}{\partial t} + \dot{\boldsymbol{R}}_0 \cdot \boldsymbol{\nabla} h + Ze\frac{\partial f_0}{\partial \epsilon_{kin}} \frac{\partial J_0 \Phi}{\partial t} = \\ &-\frac{\partial f_0}{\partial \epsilon_{kin}} \left[Ze\dot{\boldsymbol{R}}_0 \cdot \boldsymbol{\nabla} J_0 \Phi + v_\parallel \dot{p}_{z,1} + \mu \dot{\boldsymbol{R}}_1 \cdot \boldsymbol{\nabla} B \right]. \end{aligned} \tag{3.13}$$

By using Eqs. 3.2, 3.3, 3.5 for the particle charactestics, Eq. 2.28 for $\boldsymbol{v}_{\nabla B}$ (assuming that $B^*_\parallel \approx B_0$), and Eq. 2.31 for $\boldsymbol{v}_{E\times B}$, one can show straightforwardly that the expression in the square brackets on the right hand side of the above equation is equal to zero. The unperturbed characteristics can be written as

$$\dot{\boldsymbol{R}}_0 = v_\parallel \boldsymbol{b} + \frac{cm}{ZeB_0} \left(\frac{v_\perp^2}{2} + v_\parallel^2 \right) \boldsymbol{b} \times \boldsymbol{\kappa}, \tag{3.14}$$

where Eq. 1.24 is used. By performing Laplace transformation in time, as well as Fourier transformation in radial and toroidal directions

$$h \to h \exp(ik_r r + ik_\phi \phi - i\hat{\omega} t), \tag{3.15}$$

$$\Phi \to \Phi \exp(ik_r r + ik_\phi \phi - i\hat{\omega} t), \tag{3.16}$$

where r is the coordinate normal to the magnetic surfaces, ϕ is the toroidal angle ($k_\phi = 0$ for zonal modes), $\hat{\omega}$ is the complex GAM frequency, one derives the following

[1]The adiabatic part of the distribution function indicates the particles that immediately respond to the field perturbation. The adiabatic response does not have any phase shift with respect to the field perturbation and cannot lead to any instabilities (see, for example, Chapter II.A in [42]). For example, the adiabaticity of electrons due to their low inertia is a widely used approximation in GK analytical and numerical models. Such a kind of splitting is a common approach in the GK derivation based on the asymptotic expansion of the Vlasov equation. One can see for more details Eq. (20) for a general case and Eq. (25) for the axisymmetric geometry in [68]; Eqs. (21), (23) in [69]; Eqs. (31), (43) and final expression (48) in [70]; Eq. (26) with the corresponding adiabatic part Eq. (27) and non-adiabatic part Eq. (42) in [71] to name a few.

[2]The so-called Finite-Orbit-Width effect is not taken into account here since it is not crucial for the GAM description at this introductory level. Mathematically, this effect would be expressed as a $\exp(ik_r \delta \cos\theta)$ term in front of the non-adiabatic perturbation h in Eq. 3.12, with δ being a particle orbit width.

GK equation:

$$\omega_{tr}\partial_\theta - i(\hat{\omega} + \omega_d)h = -i\frac{Ze\hat{\omega}}{T} f_0 J_0(k_\perp \rho)\Phi, \tag{3.17}$$

$$\omega_{tr} = \frac{v_\parallel}{qR_0}, \tag{3.18}$$

$$\omega_d = \hat{\omega}_d \sin\theta = \frac{k_r cm}{ZeB_0R_0}\left(\frac{v_\perp^2}{2} + v_\parallel^2\right)\sin\theta. \tag{3.19}$$

Here, we take the common assumption for tokamak plasmas that the most unstable modes are whose with a long parallel (along magnetic field lines) wavelength and a short perpendicular one (see, for example, [72]). This means that $k_\parallel \ll k_r$ and leads to the presence only of the $\sin\theta$ component in ω_d (see Eq. 1.24), since we take into account only the term $(\boldsymbol{b}\times\boldsymbol{\kappa})_r k_r$ and neglect the poloidal component $(\boldsymbol{b}\times\boldsymbol{\kappa})_\theta\partial_\theta$. The magnetic drift frequency ω_d can also have dependence on the magnetic field elongation as $\sim 1/\kappa$ (see Eq. (6) in [30]), but we do not include it here. The transit frequency ω_{tr} is obtained from the poloidal derivative in the cylindrical coordinate system, and by using Eq. 1.8 for the safety factor q:

$$v_\parallel \frac{b_\theta}{r}\partial_\theta = v_\parallel \frac{B_\theta}{rB_0}\partial_\theta = \frac{v_\parallel}{qR_0}\partial_\theta. \tag{3.20}$$

After the Fourier transformation, the gyroaveraging operator J_0 can be expressed as the Bessel function of the first kind $J_0(k_\perp\rho)$. Here, $k_\perp\rho$ is the normalised wavenumber perpendicular to the magnetic lines, and it is approximated by the radial wavenumber $k_r\rho$. The Larmor radius ρ is defined in Eq. 1.53.

The final step here is to split the non-adiabatic part of the distribution function into the zonal (small k_θ in general case) $\overline{h}$ and non-zonal (high k_θ) δK components:

$$h = \overline{h} + \delta K. \tag{3.21}$$

The same splitting can be done for the potential perturbation:

$$\Phi = \overline{\Phi} + \widetilde{\Phi}. \tag{3.22}$$

Taking into account that $\omega_{tr} \gg \omega_d$, one can obtain from the GK equation 3.17 after the flux-surface averaging that

$$\overline{h} = \frac{Ze}{T} f_0 J_0(k_\perp\rho)\overline{\Phi}. \tag{3.23}$$

Using the above expression, we obtain the desired GK equation:

$$\left[\frac{\omega_{tr,sp}}{\hat{\omega}}\partial_\theta - i\left(1+\frac{\omega_{d,sp}}{\hat{\omega}}\right)\right]\delta K_{sp} = \\ -i\frac{Z_{sp}e}{T_{sp}}f_{0,sp}\left(J_0(k_\perp\rho)\widetilde{\Phi} - \frac{\omega_{d,sp}}{\hat{\omega}}J_0(k_\perp\rho)\overline{\Phi}\right), \tag{3.24}$$

where the perturbation of the species distribution function takes the following form

$$\delta f_{sp} = -\frac{Z_{sp}e}{T_{sp}}f_{0,sp}J_0(k_\perp\rho)\widetilde{\Phi} + \delta K_{sp}. \tag{3.25}$$

Here, we have restored the species subindex sp, since in the next Section we are going to consider electrons and ions (deuterium) separately.

The GK equation should be coupled with the quasi-neutrality (Poisson) equation (Eq. 2.20). It states that for plasma structures larger than the electron Debye length[3] (Eq. 1.44), the fractional charge separation allowed by the Poisson equation has to be small. The gyroagering operator in Eq. 2.20 indicates the transition of the species distribution function from the guiding-center coordinate system to the real one. By using the expression 3.25 for species distribution perturbations, one gets from the Poisson equation the following quasi-neutrality condition:

$$-\frac{e^2}{T_i}\left(1+\frac{1}{\tau_e}\right)\widetilde{\Phi} + e\langle J_0\delta K_i\rangle = \frac{m_ic^2}{B_0^2}k_r^2\overline{\Phi}, \tag{3.26}$$

where we neglect the gyroaveraging of the ion background distribution function and take into account that the background densities satisfy $\langle f_{0,i}\rangle = \langle f_{0,e}\rangle = 1$ due to the normalisation taken in Eq. 3.7. Apart from that, we have expanded $\langle J_0^2 f_{0,i}\widetilde{\Phi}\rangle$ as

$$\langle J_0^2 f_{0,i}\widetilde{\Phi}\rangle = \widetilde{\Phi} - \frac{(k_r\rho_i)^2}{2}\widetilde{\Phi}. \tag{3.27}$$

Here, J_0 is the Bessel function of the $k_r v_\perp/\omega_{ci}$ argument, $\langle . \rangle$ denotes the integration in velocity space, and $\tau_e = T_e/T_i$.

3.2 GAM dispersion relation

We shall now introduce the ordering that will be used in the derivation of the GAM dispersion relation. First of all, we assume that the radial wavenumber is a small

[3]The charge separation leads to enormous restoring electric forces. At the same time, the restoring force decreases with a decreasing separation distance. The Debye length is a fundamental characteristic distance at which the kinetic plasma energy still can sustain the charge separation.

value ($k_r\rho \ll 1$). In this case, the gyroageraging operator can be expanded as $J_0(k_r\rho) = 1-(k_r\rho)^2/4$. To keep only terms of the smallest order, we take $J_0(k_r\rho) = 1$. Since the GAMs are sound oscillations, we have $Re[\hat{\omega}] \sim u_{th,i}/R$. Here, τ_e is assumed to be close to one. We are going to use the ratio $\omega_{d,i}/\hat{\omega} \sim k_r\rho_i$ as the smallness parameter ϵ. The ordering of the drift frequency $\omega_{d,sp}$ is the same for all species, since the drift frequency does not depend on the species mass (in Eq. 3.19 squared velocities $(v_{\perp,sp}^2/2 + v_{\parallel,sp}^2)$ are proportional to m_{sp}^{-1}). The non-zonal component $\widetilde{\Phi}$ is considered to be much smaller than the zonal one $\overline{\Phi}$ as discussed in Sec. 1.3, and the ratio $\widetilde{\Phi}/\overline{\Phi}$ is of the order of ϵ (more precisely, $e\overline{\Phi}/T \sim \mathcal{O}(1)$, while $e\widetilde{\Phi}/T \sim \mathcal{O}(\epsilon)$). From Eq. 3.23 follows that $\overline{h}_{sp}/f_{0,sp} \sim \mathcal{O}(1)$. Correspondingly, we assume that the non-zonal component of the distribution function $\delta K_{sp}/f_{0,sp}$ is of the order of ϵ. The electrons have a high speed along the magnetic field due to their small mass, leading to the domination of the electron transit frequency (Eq. 3.18) over all other frequencies. On the other hand, it is known that the ion transit frequency $\omega_{tr,i}$ is of the order of the sound frequency. This means that it is of the order of the GAM frequency. To sum up, the ordering of the system is the following one:

$$\frac{\omega_{d,sp}}{\hat{\omega}} \sim \mathcal{O}(\epsilon), \ \frac{\omega_{tr,e}}{\hat{\omega}} \sim \mathcal{O}(\epsilon^{-1}), \ \frac{\omega_{tr,i}}{\hat{\omega}} \sim \mathcal{O}(1), \tag{3.28}$$

$$\frac{e\overline{\Phi}}{T} \sim \mathcal{O}(1), \quad \frac{e\widetilde{\Phi}}{T} \sim \mathcal{O}(\epsilon), \tag{3.29}$$

$$\frac{\delta K_{sp}}{f_{0,sp}} \sim \mathcal{O}(\epsilon). \tag{3.30}$$

Now, we are going to consider the GK equation separately for different species. We start from the case of electrons. For the lowest order of Eq. 3.24 we have

$$\frac{\omega_{tr,e}}{\hat{\omega}}\partial_\theta \delta K_e = 0. \tag{3.31}$$

The above expression indicates that $\delta K_e = 0$ since it has to be non-zonal (has the dependence on the poloidal angle). This means that we are dealing with adiabatic electrons, as it was mentioned at the beginning of this chapter, whose distribution perturbation function does not have the non-adiabatic component.

Next, we are going to work with the ion GK equation. Considering only the $\mathcal{O}(\epsilon)$ terms, we get for deuterium

$$\left(\frac{\omega_{tr,i}}{\hat{\omega}}\partial_\theta - i\right)\delta K_i = -i\frac{f_{0,i}e}{T_i}\left(\widetilde{\Phi} - \frac{\omega_{d,i}}{\hat{\omega}}\overline{\Phi}\right), \tag{3.32}$$

where only the dynamics of deeply-passing particles are taken into account (in other words, $\omega_{tr,i} = \text{const}$ in poloidal direction). Now, we are splitting the non-zonal

distribution and field perturbations on the $\cos\theta$ and $\sin\theta$ components:

$$\widetilde{\Phi} = \widetilde{\Phi}_c \cos\theta + \widetilde{\Phi}_s \sin\theta, \tag{3.33}$$

$$\delta K_i = \delta K_{i,c} \cos\theta + \delta K_{i,s} \sin\theta, \tag{3.34}$$

where the functions in front of the $\sin\theta$ and $\cos\theta$ are assumed to be independent on the poloidal angle. Considering separately the $\cos\theta$ and $\sin\theta$ terms, and taking into account Eq. 3.19, one gets the following system of equations:

$$\begin{pmatrix} i\hat{\omega} & -\omega_{tr,i} \\ \omega_{tr,i} & i\hat{\omega} \end{pmatrix} \begin{pmatrix} \delta K_{i,c} \\ \delta K_{i,s} \end{pmatrix} = \frac{i f_{0,i} e \hat{\omega}}{T_i} \begin{pmatrix} \widetilde{\Phi}_c \\ \widetilde{\Phi}_s - \hat{\omega}_{d,i} \overline{\Phi}/\hat{\omega} \end{pmatrix}. \tag{3.35}$$

From this system, one can find the non-zonal distribution perturbation for the ions:

$$\delta K_{i,c} = \frac{i f_{0,i} e}{T_i} \frac{\hat{\omega}}{\omega_{tr,i}^2 - \hat{\omega}^2} \left(i\hat{\omega}\widetilde{\Phi}_c + \omega_{tr,i}\widetilde{\Phi}_s - \omega_{tr,i} \frac{\hat{\omega}_{d,i}}{\hat{\omega}} \overline{\Phi} \right), \tag{3.36}$$

$$\delta K_{i,s} = \frac{i f_{0,i} e}{T_i} \frac{\hat{\omega}}{\omega_{tr,i}^2 - \hat{\omega}^2} \left(-\omega_{tr,i}\widetilde{\Phi}_c + i\hat{\omega}\widetilde{\Phi}_s - i\hat{\omega}_{d,i}\overline{\Phi} \right). \tag{3.37}$$

Here, it is necessary to find the electric potential. To do that, we need the quasi-neutrality equation 3.26, where we take into account that

$$\langle J_0 \delta K_i \rangle \approx \langle \delta K_i \rangle - \frac{(k_r \rho_i)^2}{4} \langle \delta K_i \rangle. \tag{3.38}$$

Since we consider here only the terms of the lowest order with respect to $k_r \rho_i$, we get the following quasi-neutrality condition:

$$\left(1 + \frac{1}{\tau_e} \right) \widetilde{\Phi} = \frac{T_i}{e} \langle \delta K_i \rangle, \tag{3.39}$$

where $\delta K_e = 0$ because of the electron adiabaticity. By rewriting Eq. 3.39 using Eqs. 3.33, 3.34, one obtains:

$$\left(1 + \frac{1}{\tau_e} \right) (\widetilde{\Phi}_c \cos\theta + \widetilde{\Phi}_s \sin\theta) = \frac{T_i}{e} \left(\langle \delta K_{i,c} \rangle \cos\theta + \langle \delta K_{i,s} \rangle \sin\theta \right). \tag{3.40}$$

First of all, one should notice that $f_{0,i}$ (Eq. 2.36) and $\hat{\omega}_{d,i}$ (Eq. 3.19) are even functions of the parallel speed $v_{\parallel,i}$, while the $\omega_{tr,i}$ is an odd one. Therefore, the terms proportional to $\omega_{tr,i}$ in Eqs. 3.36, 3.37 disappear after the velocity integration $\langle . \rangle$.

During the velocity integration, we are going to use the expression of the Plasma Dispersion Function (PDF) [73]:

$$\mathcal{Z}(z) = \frac{1}{\sqrt{\pi}} \int_{-\infty}^{+\infty} \frac{\exp(-y^2)}{y - z}\, \mathrm{d}y = -\sqrt{\pi}\exp(-z^2)(\mathrm{Erfi}(z) + i), \tag{3.41}$$

where $Im(z) < 0$, $\mathrm{Erfi}(z)$ is the Imaginary Error Function, and the following integrals can be evaluated using the PDF:

$$\frac{1}{\sqrt{\pi}} \int_{-\infty}^{+\infty} \frac{\exp(-y^2)}{y^2 - z^2}\, \mathrm{d}y = \frac{\mathcal{Z}(z)}{z}, \tag{3.42}$$

$$\frac{1}{\sqrt{\pi}} \int_{-\infty}^{+\infty} \frac{y^2\exp(-y^2)}{y^2 - z^2}\, \mathrm{d}y = 1 + z\mathcal{Z}(z), \tag{3.43}$$

$$\frac{1}{\sqrt{\pi}} \int_{-\infty}^{+\infty} \frac{y^4\exp(-y^2)}{y^2 - z^2}\, \mathrm{d}y = \frac{1}{2} + z^2 + z^3\mathcal{Z}(z). \tag{3.44}$$

Derivation of Eq. 3.41 is considered in Appendix A. We start from the first term on the right hand side in Eq. 3.40:

$$\langle \delta K_{i,c} \rangle = -\frac{e\widetilde{\Phi}_c}{T} \frac{\hat{\omega}^2}{u_{th}^3 \pi^{3/2}} \left\langle \frac{\exp\left(-(v_\parallel^2 + v_\perp^2)/u_{th}^2\right)}{\omega_{tr}^2 - \hat{\omega}^2} \right\rangle, \tag{3.45}$$

where we skip for simplicity the ion subindex on the right hand side of the equation. Integration on velocity space is performed in cylindrical coordinates

$$\int_{-\infty}^{+\infty} \mathrm{d}^3 v = 2\pi \int_0^{+\infty} v_\perp\, \mathrm{d}v_\perp \int_{-\infty}^{+\infty} \mathrm{d}v_\parallel. \tag{3.46}$$

Therefore, the integration on the perpendicular velocity gives

$$\left\langle \frac{\exp(-(v_\parallel^2 + v_\perp^2)/u_{th}^2)}{\omega_{tr}^2 - \hat{\omega}^2} \right\rangle = \pi u_{th}^2 \int_{-\infty}^{+\infty} \frac{\exp(-v_\parallel^2/u_{th}^2)}{\omega_{tr}^2 - \hat{\omega}^2}\, \mathrm{d}v_\parallel, \tag{3.47}$$

and by applying the following change of variables

$$y = \frac{v_\parallel}{u_{th}},\ z = \frac{\hat{\omega}}{\omega_0},\ \omega_0 = \frac{u_{th}}{qR_0}, \tag{3.48}$$

one can perform the integration on the parallel velocity by using Eq. 3.42:

$$\int_{-\infty}^{+\infty} \frac{\exp(-v_\parallel^2/u_{th}^2)}{\omega_{tr}^2 - \hat{\omega}^2}\, \mathrm{d}v_\parallel = \frac{u_{th}}{\omega_0^2} \int_{-\infty}^{+\infty} \frac{\exp(-y^2)}{y^2 - z^2}\, \mathrm{d}y = \sqrt{\pi}\frac{u_{th}}{\omega_0^2}\frac{\mathcal{Z}(z)}{z}. \tag{3.49}$$

Combining Eqs. 3.47, 3.49, and by inserting the result into Eq. 3.45, one gets

$$\langle \delta K_{i,c} \rangle = -\frac{e\widetilde{\Phi}_c}{T} z \mathcal{Z}(z). \tag{3.50}$$

Now, we are going to consider the second term on the right hand side of Eq. 3.40:

$$\langle \delta K_{i,s} \rangle = -\frac{e\hat{\omega}^2}{T} \left\langle \frac{f_0}{\omega_{tr}^2 - \hat{\omega}^2} \right\rangle \widetilde{\Phi}_s + \frac{e\hat{\omega}}{T} \left\langle \frac{f_0 \hat{\omega}_d}{\omega_{tr}^2 - \hat{\omega}^2} \right\rangle \overline{\Phi}. \tag{3.51}$$

The first term is evaluated in the same way as it has been done above:

$$-\frac{e\hat{\omega}^2}{T} \left\langle \frac{f_0}{\omega_{tr}^2 - \hat{\omega}^2} \right\rangle \widetilde{\Phi}_s = -\frac{e\widetilde{\Phi}_s}{T} z \mathcal{Z}(z). \tag{3.52}$$

The integration on the perpendicular velocity of the second term gives

$$\left\langle \frac{f_0 \hat{\omega}_d}{\omega_{tr}^2 - \hat{\omega}^2} \right\rangle = \frac{k_r cm}{eB_0 R_0} \frac{1}{u_{th}\sqrt{\pi}} \int_{-\infty}^{+\infty} \mathrm{d}v_\parallel \frac{\left(u_{th}^2/2 + v_\parallel^2\right) \exp\left(-v_\parallel^2/u_{th}^2\right)}{\omega_{tr}^2 - \hat{\omega}^2}. \tag{3.53}$$

The first part of this integral can be found by using again Eq. 3.42. The second part is evaluated to

$$\int_{-\infty}^{+\infty} \mathrm{d}v_\parallel \frac{v_\parallel^2 \exp\left(-v_\parallel^2/u_{th}^2\right)}{\omega_{tr}^2 - \hat{\omega}^2} = \sqrt{\pi} \frac{u_{th}^3}{\omega_0^2} (1 + z\mathcal{Z}(z)) \tag{3.54}$$

using Eq. 3.43. Using the above equations, we transform Eq. 3.51 into

$$\langle \delta K_{i,s} \rangle = \frac{e}{T_i} \left(-z\mathcal{Z}(z)\widetilde{\Phi}_s + \frac{k_r cm}{eB_0 R_0} \frac{u_{th}^2}{\omega_0} N(z) \overline{\Phi} \right), \tag{3.55}$$

$$N(z) = z + \left(\frac{1}{2} + z^2\right) \mathcal{Z}(z). \tag{3.56}$$

Now, by substituting Eqs. 3.50, 3.55 into Eq. 3.40, and considering separately the terms in front of $\cos\theta$ and $\sin\theta$, we can find expressions for the non-zonal components of the electric potential:

$$\widetilde{\Phi}_c = 0, \tag{3.57}$$

$$\widetilde{\Phi}_s = \frac{k_r cm}{eB_0 R_0} \frac{u_{th}^2}{\hat{\omega}} \frac{N(z)}{D(z)} \overline{\Phi}, \tag{3.58}$$

$$D(z) = \frac{1}{z} \left(1 + \frac{1}{\tau_e}\right) + \mathcal{Z}(z). \tag{3.59}$$

To get the GAM dispersion relation, one has to consider one order higher terms (more precisely, the terms of the second order of smallness). In particular, we are going to consider the flux-surface-averaged quasi-neutrality condition 3.26, and ion gyrokinetic equation 3.24 multiplied by J_0:

$$e\overline{\langle J_0 \delta K_i \rangle} = \frac{m_i c^2}{B_0^2} k_r^2 \overline{\Phi}, \tag{3.60}$$

$$\hat{\omega}\overline{\langle J_0 \delta K_i \rangle} + \overline{\langle \omega_{d,i} J_0 \delta K_i \rangle} = 0, \tag{3.61}$$

where the integration on velocity space is performed. From this system we immediately obtain the following equation

$$\hat{\omega}\frac{m_i c^2}{e B_0^2} k_r^2 \overline{\Phi} = -\overline{\langle \omega_{d,i} J_0 \delta K_i \rangle}. \tag{3.62}$$

After that, we consider only the terms of the second order of smallness, and by applying Eqs. 3.19, 3.34, one gets the following flux-surface-averaged vorticity equation:

$$\frac{2m}{B_0^2}\hat{\omega} k_r^2 \overline{\Phi} = -\frac{e}{c^2}\left\langle \hat{\omega}_{d,i} \delta K_{i,s} \right\rangle. \tag{3.63}$$

Finally, by using Eq. 3.44 to integrate the term $\langle \hat{\omega}_{d,i} \delta K_{i,s} \rangle$, one gets the GAM dispersion relation

$$z + q^2 \left(F(z) - \frac{N^2(z)}{D(z)} \right) = 0, \tag{3.64}$$

$$F(z) = z(z^2 + \frac{3}{2}) + (z^4 + z^2 + \frac{1}{2})\mathcal{Z}(z), \tag{3.65}$$

where z is the sought for normalised complex GAM frequency (Eq. 3.48). By taking the species temperatures and the safety factor at a particular radial point s, one can numerically solve Eq. 3.64 (it is more convenient to find poles of the inverse expression) to estimate the wave frequency and damping rate for a small radial wavenumber $k_r \rho_i \ll 1$ in the case of a circular magnetic configuration.

The dispersion relation 3.64 is similar to that obtained in Eq. (2) in [28] (or Eq. (2.7) in [74]). The main difference is that the dispersion relation in [28, 74] includes a term proportional to $(k_r \rho_i q)^2 \exp(-Re[\hat{\omega}]^2/4)$, $\rho_i = u_{th,i}/\omega_{c,i}$, which contributes to the wave damping rate (Eqs. 3.67, 3.70). This term appears due to finite orbit width effects that has been neglected here. For later reference, we show

here without derivation approximate explicit formulae for the GAM frequency and damping rate found in [28]:

$$\omega = Re[\hat{\omega}] = q\omega_{0,i}\frac{\sqrt{7+4\tau_e}}{2}\sqrt{1+\mathcal{R}_1}, \tag{3.66}$$

$$\gamma = Im[\hat{\omega}] = -q^2\omega_{0,i}\frac{\sqrt{\pi}\mathcal{R}_{23}}{2+\mathcal{R}_1}, \tag{3.67}$$

where

$$z_r = Re[z], \tag{3.68}$$

$$\mathcal{R}_1 = \frac{2(23+16\tau_e+4\tau_e^2)}{q^2(7+4\tau_e)^2}, \tag{3.69}$$

$$\mathcal{R}_{23} = \exp(-z_r^2)\mathcal{R}_2 + \frac{1}{64}(k_r\rho_i q)^2\exp(-z_r^2/4)\mathcal{R}_3, \tag{3.70}$$

$$\mathcal{R}_2 = (1+2\tau_e)z_r^2 + z_r^4, \tag{3.71}$$

$$\mathcal{R}_3 = \left(6+7\tau_e+\frac{5}{2}\tau_e^2\right)z_r^2 + (1+\tau_e)z_r^4 + \frac{1}{8}z_r^6, \tag{3.72}$$

and z, $\omega_{0,i}$ are defined in Eq. 3.48. The above equations are valid for $k_r\rho_i q^2 \ll 1$. One can see from these expressions that the GAM frequency has significant dependence on the safety factor and the plasma temperatures, while the damping rate also significantly increases with the radial wavenumber.

Chapter 4

GAM damping

In this chapter, we consider different GAM damping mechanisms in the tokamak plasma systems, briefly introduced in Sec. 1.4. In particular, in Sec. 4.1, we are going to investigate the Landau damping of the geodesic acoustic modes by thermal species in different plasma regimes, with the main emphasis on the role of electron dynamics. A process, called phase mixing, where increased mode damping due to non-flat temperature and safety factor profiles is observed, is presented in Sec. 4.2. In Sec. 4.3, the collisional damping of the geodesic modes is briefly discussed. Finally, in Sec. 4.4, the GAM linear frequency spectrum is estimated in an ASDEX Upgrade discharge, and the collisional damping is compared with the Landau damping of the mode. Most of the results presented in this chapter have been published in [34].

4.1 Landau damping

It was reported previously [32, 33] that models derived with adiabatic electrons can result in significantly smaller GAM damping rate in comparison to simulations performed with kinetic electrons. By adiabatic electron models, we mean here models treating the $m \neq 0$ component of the electrons as adiabatic, and setting the zonal component of the electron density perturbation to zero. By performing linear electromagnetic GK simulations with drift-kinetic electrons, which have a realistic deuterium-electron mass ratio $m_e/m_d = 2.5 \cdot 10^{-4}$, the influence of the electron dynamics on the geodesic mode behaviour is shown. Interpolating formulae for the GAM frequency and damping rate in different plasma regimes are derived based on the gyrokinetic simulations with ORB5.

Electrostatic simulations with kinetic electrons are faster than electromagnetic simulations, due to the smaller number of equations to be solved. Nevertheless, a high

frequency oscillation, called the ω_H-mode [75], is observed to be often numerically unstable. From gyrokinetic Vlasov and Poisson equations in a slab geometry one can obtain a plasma dispersion relation, and one of whose solutions is the ω_H-mode. It can be considered as an electrostatic shear Alfvén wave, which has the highest growth rate at $(k_\perp \rho_s)(\omega_H \Delta t) = \sqrt{2}$ with the onset of instability at $\omega_H \Delta t \gtrapprox 1$, where Δt is the time step in a considered simulation. To decrease the level of the high-frequency oscillations, electromagnetic simulations in the small-β_e limit ($\beta_e = 10^{-5}$) are performed instead of the electrostatic ones. MHD equilibria of the circular and elongated plasma is calculated with the external code CHEASE [64]. Simulations are carried out with a flat density profile, which is shown to not impact the GAM frequency and damping rate in linear simulations (Appendix in [34]). To focus on the Landau damping in the absence of the phase mixing effect, a flat temperature profile is considered. Since the safety factor profiles are taken from the CHEASE code, there is a magnetic shear ($s\partial_s \ln(q) \neq 0$) that also causes the phase mixing, but its influence on the GAM frequency (and as a result, on the damping rate due to the increase of the radial wavenumber, see Sec. 4.2) is much smaller in comparison to the temperature gradient effect (Eq. 3.66).

The plasma parameters are taken close to the AUG parameters near the plasma edge [49]: the major radius $R_0 = 1.65\ m$, the minor radius $a = 0.5\ m$ (inverse aspect ratio is $\varepsilon = 0.303$), the magnetic field on the axis $B_0 = 2\ T$. In the CHEASE code, the plasma elongation κ is defined at the plasma boundary and changes gradually to the plasma center. Since we know the exact value of the elongation only at the edge, we measure the GAM frequency and damping rate near the plasma boundary (at the radial position $s_0 = 0.90$) to make the scan on the elongation more precise. We consider a deuterium plasma: $m_d = 2m_p$, $Z_d = 1$, where m_p is the proton mass. The temperature is taken to be $T_d = T_e = 70\ eV$. This means that $c_s = 5.8 \cdot 10^4\ m/s$, $\rho_s = c_s/\omega_{cd} = 6.1 \cdot 10^{-4}\ m$, $\rho^* = \rho_s/a = 1.2 \cdot 10^{-3}$, and the deuterium gyro-frequency is $\omega_{ci}/(2\pi) = 15.2\ MHz$. To weaken the constraint on the radial resolution, we simulate only a ring from $s_1 = 0.85$ to $s_2 = 0.95$ in a poloidal cross section with the Dirichlet condition for the potential ϕ on boundaries ($\phi(s_1) = \phi(s_2) = 0$).

A standard simulation in this work has the following parameters. Number of nodes in radial direction is taken to be $n_s = 256$, in toroidal directions $n_\phi = 4$ and along the straight-field-line coordinate χ the number of nodes is $n_\chi = 64$. Time step is $dt[\omega_{ci}^{-1}] = 2$. The GAM damping rate and frequency are calculated for different GAM radial wavenumbers $k = k_r \rho_i \in [0.054, 0.377]$ (in this chapter, $\rho_i = \rho_d = \sqrt{2} v_{Td}/\omega_{cd} = 8.57 \cdot 10^{-4}\ m$ is the deuterium Larmor radius), the safety factor $q \in [3.5, 5.0]$ at $s_0 = 0.90$ and the plasma elongation $\kappa \in [1.0, 1.6]$ at the edge. This is the regime where GAMs are typically observed in tokamak plasmas (see, for example, [49]).

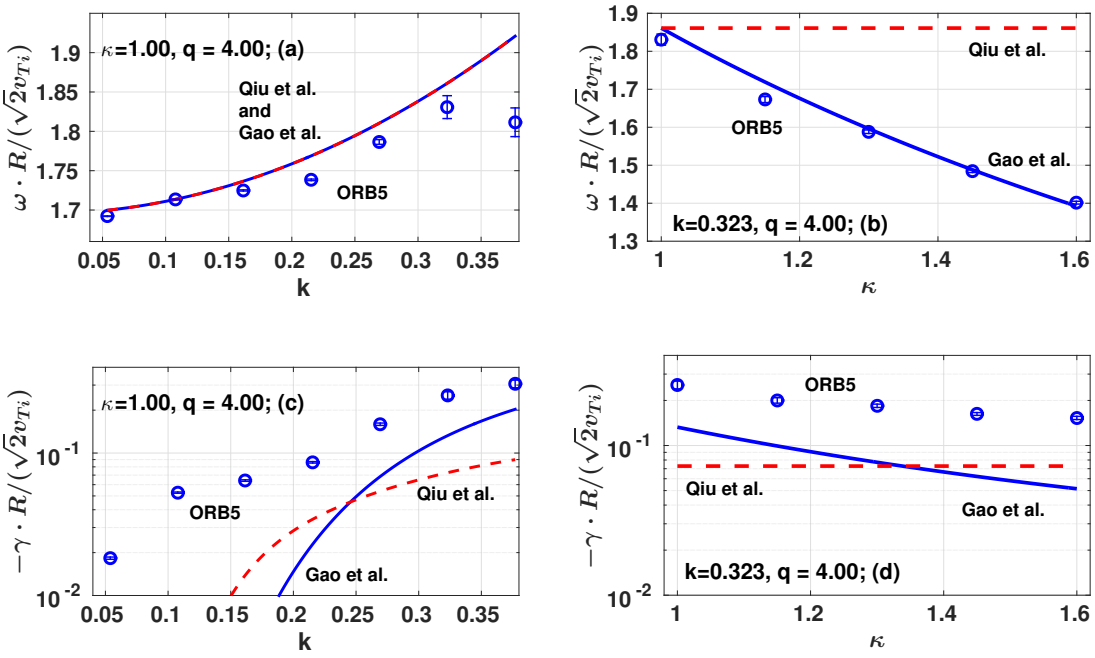

Figure 4.1: Comparison of linear gyrokinetic simulations (blue dots), performed with drift-kinetic electrons, with the analytical theories Gao 2010 [30] (solid blue line) and Qiu et al. 2008 [29] (dashed red line), derived with adiabatic electrons. Here, $k = k_r\rho_i$ is the normalised radial wavenumber, q is the safety factor, κ is the elongation. *Reprinted with permission from [34], with permission from AIP Publishing.*

The ORB5 simulations are initialized by introducing a zonal density perturbation designed to produce an initial electric potential field of the form $\sim \sin(ks)$, where $s \in [s_1, s_2]$ (as in the so-called Rosenbluth-Hinton test [9]). All toroidal modes $n \neq 0$ and poloidal modes $|m| > 10$ are filtered out. To study the GAM dynamics, the frequency and damping rate of the zonal radial electric field are calculated.

In Fig. 4.1, a comparison of the GAM frequencies and damping rates obtained from the numerical simulations with two analytical theories of Qiu et al. 2009 [29] and Gao 2010 [30] is shown. Both the analytical theories derived using adiabatic electrons take into account higher order transit resonances[1] (see Eq. 5.5) and can be applied in the case with $k_r\rho_i q^2 \gg 1$, which is opposite to the approach presented in Chapter 3. However, the Gao theory also includes geometric effects of the background magnetic field such as the field elongation κ. A good agreement between the numerical results

[1]The large orbit drift width limit.

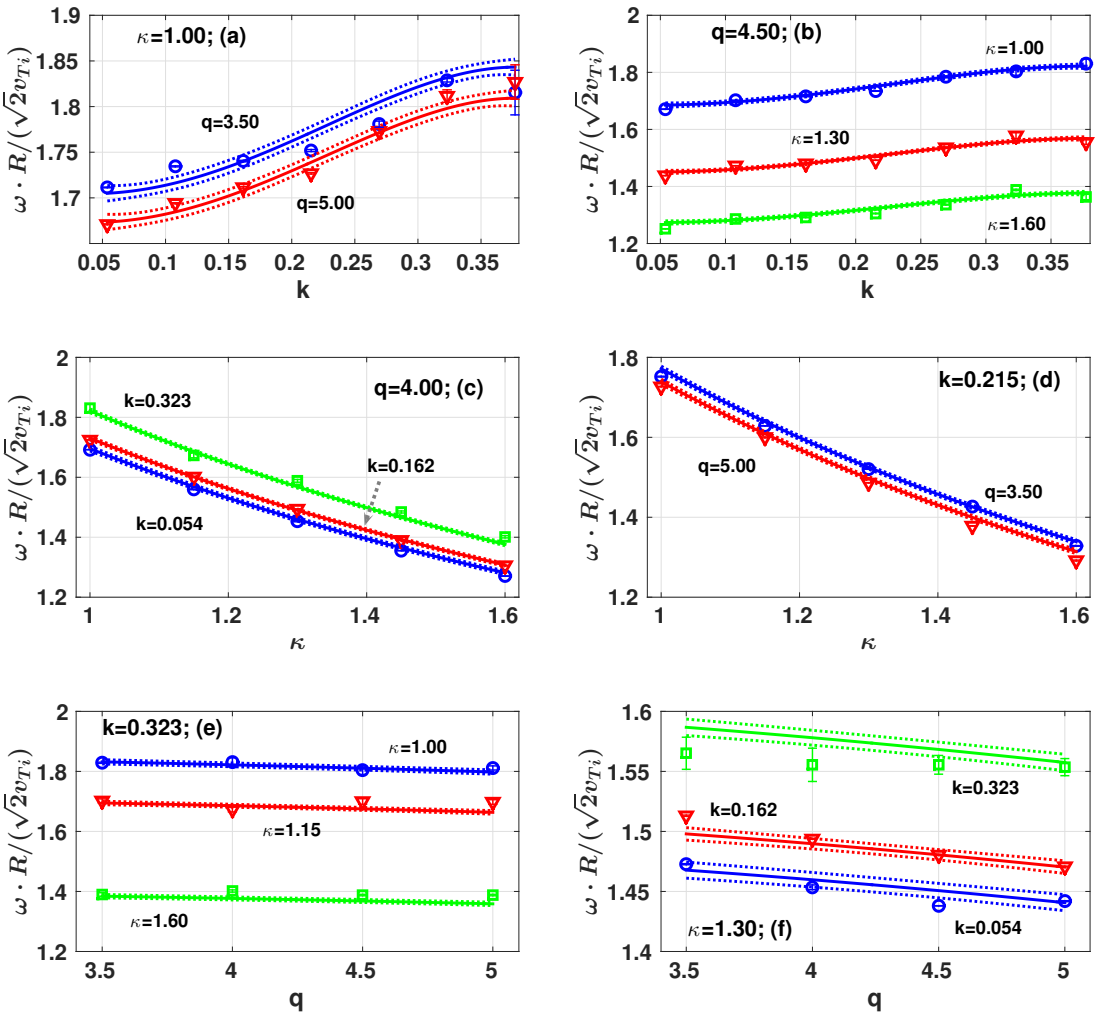

Figure 4.2: Comparison between numerical simulations (dots, triangles and squares) of the GAM frequency and values obtained using the interpolating expression provided in Eq. 4.1 (solid lines). Dotted lines indicate 95% confidence bounds of the fitting. Here, $k = k_r \rho_i$ is the normalised radial wavenumber, q is the safety factor, κ is the elongation. *Reprinted with permission from [34], with permission from AIP Publishing.*

and the analytical predictions of the GAM frequency are found. Nevertheless, the analytical GAM damping rate is smaller in comparison to the numerical simulations with drift-kinetic electrons, and the divergence increases for smaller values of the

GAM radial wavenumber. Moreover, a divergence in the GAM frequency between the numerical results and the analytical theories is observed in the domain of higher wavenumbers (Fig. 4.1).

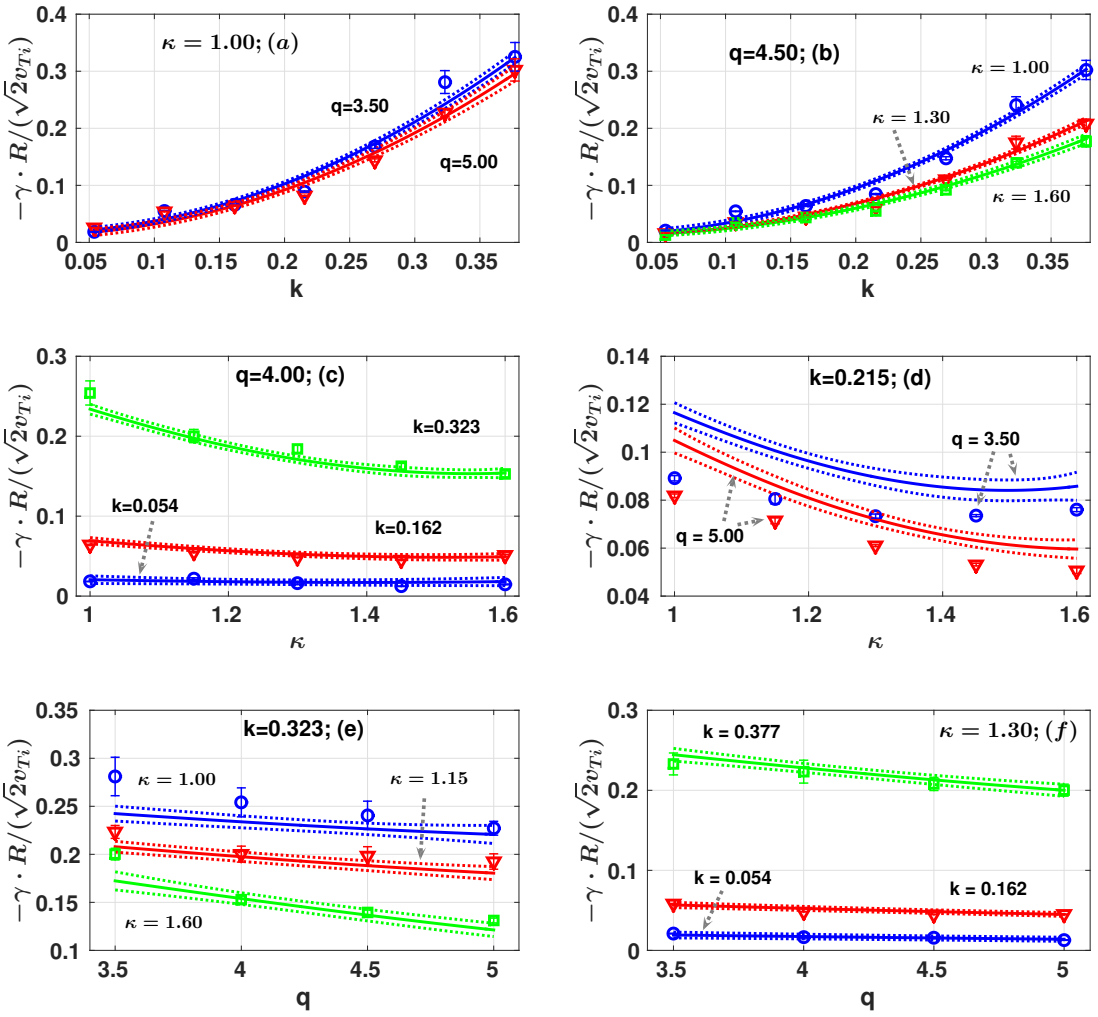

Figure 4.3: Comparison between numerically simulated values (dots, triangles or squares) of the GAM damping rate and values obtained by using the interpolating expression provided in Eq. 4.2 (solid lines). Dotted lines indicate 95% confidence bounds of the fitting. Here, $k = k_r\rho_i$ is the normalised radial wavenumber, q is the safety factor, κ is the elongation. *Reprinted with permission from [34], with permission from AIP Publishing.*

As it was mentioned above, the Gao 2010 theory describes the GAM dependence on the plasma elongation and it is in a good agreement with numerical results for the frequency. Although the Gao 2010 theory provides significantly smaller damping rate in comparison to the simulations, it seems to give a similar trend of the damping coefficient with the plasma elongation, i.e., the damping rate is weakened by the elongation. Since the theory is derived in the large orbit drift width limit, the dominant damping mechanism is the resonance $\omega \sim \omega_d$, where the magnetic drift $\omega_d = \boldsymbol{k}_r \cdot \boldsymbol{v}_d$ (see Eq. 3.19 and the text after it) is defined by the drift velocity $\boldsymbol{v}_d$ (see Eq. 1.54). As explained in [30], the GAM frequency decreases with the increase of the elongation more slowly than the drift frequency. This means only the particles with higher drift velocities can satisfy the resonance $\omega \sim \omega_d$. Since the resonance in this case involves fewer particles, the GAM damping rate decreases.

To provide a scaling of the GAM frequency and damping rate, corresponding interpolating expressions are fitted to the results of the gyrokinetic simulations. These expressions are valid within the parameter range considered in our simulations: GAM radial wavenumber $k = k_r \rho_i \in [0.054, 0.377]$, safety factor $q \in [3.5, 5.0]$, and plasma elongation $\kappa \in [1.0, 1.6]$.

To derive an interpolating expression for the frequency, several assumptions are used. The experimentally obtained dependence [49] on the plasma elongation $1/(1+\kappa)$ is slightly modified to $1/(1+g_6\kappa)$, where g_6 is an adjustable coefficient. The dependence on the safety factor is taken in the form $\exp(-g_5 q^2)$. In fact, the q-dependence in a form of $\sqrt{1+g_5/q^2}$ given in [33], gives the same results. To describe how the frequency changes with the radial wavenumber, a polynomial is taken. Moreover, to take into account the frequency saturation for higher wavenumbers [76], we introduce a function of the form $1/(1+g_4 k)$. The resulting frequency interpolating formula is the following one (here, the frequency is normalised to $\sqrt{2}v_{Ti}/R_0$):

$$f_\omega \left[\frac{\sqrt{2} v_{Ti}}{R_0} \right] = \frac{g_1 + g_2 k^2 + g_3 k^4}{1 + g_4 k} \frac{\exp\left(-g_5 q^2\right)}{1 + g_6 \kappa}. \tag{4.1}$$

Among different tested functions, this form gives the best approximation to numerically simulated values of the GAM frequency, it has one of the smallest 95% confidence bounds and is not overfitted. The corresponding coefficients g with their

95% confidence bounds (lower g_{lc} and upper g_{uc} bounds) are

$$\begin{aligned} g = \quad & [3.7733,\ 6.3505,\ -1.9741e1, \\ & 1.3557e-1,\ 1.4620e-3,\ 1.1684], \\ g_{lc} = \quad & [3.6745,\ 3.3168,\ -2.8800e1, \\ & -6.0078e-2,\ 1.1373e-3,\ 1.1234], \\ g_{uc} = \quad & [3.8720,\ 9.3843,\ -1.0682e1, \\ & 3.3121e-1,\ 1.7866e-3,\ 1.2135]. \end{aligned}$$

Results for the Eq. 4.1 are depicted in Fig. 4.2.

For the damping rate we get the following expression:

$$f_\gamma \left[\frac{\sqrt{2} v_{Ti}}{R_0} \right] = \frac{(h_1 + h_2 k^2) \exp\left[-h_3 q^2\right]}{1 + h_4 \kappa^2} + \\ + \frac{(h_5 + h_6 k^2) \exp\left[-h_7 q^2\right]}{1 + h_8 \kappa^4}. \tag{4.2}$$

with the interpolating coefficients

$$\begin{aligned} h = \quad & [-1.2494e-2,\ -8.9688e-1,\ 4.5498e-2, \\ & -1.9884e-1,\ -1.1248e-2, -2.5481, \\ & -5.3340e-3,\ 7.7748e-1], \\ h_{lc} = \quad & [-2.3115e-2,\ -1.6490,\ 2.5215e-2, \\ & -3.3573e-1,\ -2.5523e-2,\ -3.1909, \\ & -1.9665e-2,\ 5.1924e-2], \\ h_{uc} = \quad & [-1.8723e-3,\ -1.4471e-1,\ 6.5781e-2, \\ & -6.1955e-2,\ 3.0272e-3,\ -1.9053, \\ & 8.9973e-3,\ 1.5030]. \end{aligned}$$

Comparison between the results from the gyrokinetic simulations and the interpolation expression for the GAM damping rate is shown in Fig. 4.3 for some specific values of parameters taken as examples.

4.2 Phase mixing

To investigate the influence of the phase mixing on the GAM dynamics, we take the same parameters as in Sec. 4.1, but introducing a temperature gradient (the same

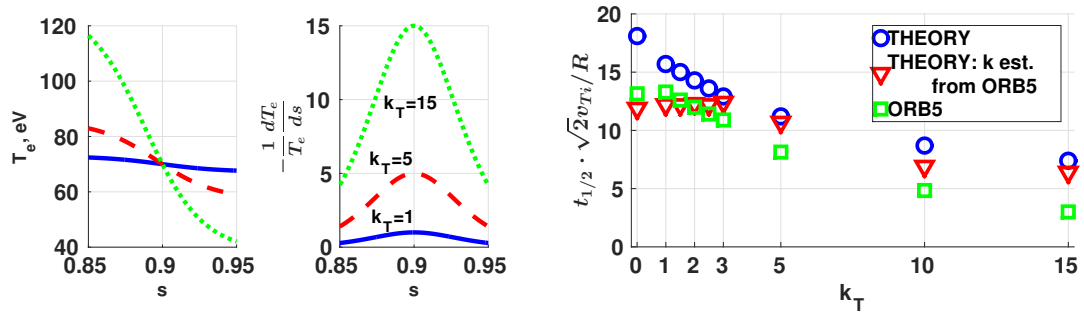

Figure 4.4: Left plot: Radial profiles of the temperature and its gradient for different k_T: $k_T = [1, 5, 15]$ (blue solid, red dashed and green dotted curves respectively). Right plot: Dependence of the GAM half-decay time on the temperature gradient: GK simulations in ORB5 (green squares), analytical theory using the linear estimation Eq. 4.10 (blue dots), and analytical theory using numerical estimation of the radial wavenumber in the GK simulations (red triangles). Here, it is the combined effect of the drift-kinetic electrons and the phase mixing that gives the resulting numerical and analytical estimation of the GAM half-decay time. *Reprinted with permission from [34], with permission from AIP Publishing.*

for both electrons and ions to have $\tau_e = T_e/T_i = 1$, $T_i(s_0) = 70\ eV$) at the radial position $s_0 = 0.90$. The radial point $s_0 = 0.90$ is chosen here to be in agreement with Sec. 4.1. The initial radial wavenumber of the radial electric field is $k = 0.108$. The safety factor is $q(s_0) = 4.0$. We consider a temperature profile of the following form, similarly to [40]:

$$\frac{T_e(s)}{T_e(s_0)} = \exp\left[-\Delta \cdot k_T \cdot \tanh\left(\frac{s - s_0}{\Delta}\right)\right], \tag{4.3}$$

where $\Delta = 0.04$, $k_T = -\,d[\ln(T)]/ds|_{s=s_0}$. The temperature profiles and the corresponding temperature gradient profiles for different k_T in a radial interval $s = [0.85, 0.95]$ are shown in Fig. 4.4. Dependence of the GAM half-decay time $t_{1/2}$ on the temperature gradient is investigated in the domain $k_T \in [1, 15]$[2]. A scan of gyrokinetic simulations with the temperature gradient k_T is performed, and the results are depicted in Fig. 4.4, green squares. Due to the temperature gradient, the GAM oscillates with different frequencies at different radial points. This leads to the distortion of the initial GAM radial structure. Producing higher radial wavenumbers, this

[2]For example, in the AUG#20787 discharge considered in Sections 4.4 and 8.2, the normalised temperature gradient is $k_T(s = 0.9) \approx 8.5$, but it significantly increases at the very edge of the plasma system due to small temperature values.

distortion amplifies the GAM damping. This combined effect, already investigated in [39, 40] for a more simplified configuration, is observed even more pronounced in the gyrokinetic simulations performed with drift-kinetic electrons. For example, using the Sugama-Watanabe model for the Landau damping [28], which is derived with adiabatic electrons, and combining with phase mixing, using Eq. 4.10 for the evolution of the wavenumber, we obtain $t_{1/2}[R_0/(\sqrt{2}v_{Ti})] = 118$ for the $k_T = 1$ and $t_{1/2}[R_0/(\sqrt{2}v_{Ti})] = 23.4$ for $k_T = 10$. This adiabatic estimation predicts much longer GAM half-decay time in comparison to the calculations based on the simulations with the drift-kinetic electrons (compare with Fig. 4.4).

In order to verify the results of the gyrokinetic simulations, we use a theoretical simplified model of the phase mixing proposed in [16, 39, 40], where a linear growth in time of the radial wavenumber is considered.

In the phase mixing simulations, a space point s_0 is considered with a certain temperature $T(s_0)$ and temperature gradient $k_T(s_0)$. The initial radial electric field has the following radial structure:

$$E(s) = E_0 \cos(k_0 s) \tag{4.4}$$

with the initial amplitude E_0 and initial normalised radial wavenumber k_0. The electric field is assumed to evolve in time at a point s_0 according to a simple rule

$$E(s_0, t) = E_a(s_0, t) \cos(\omega(s_0)t), \tag{4.5}$$

where $E_a(s_0, t)$ is the amplitude of the electric field, which changes in time due to the damping, $E_a(0) = E_0$. The general form of the GAM frequency is

$$\omega(s, t) = \frac{\sqrt{2}c_s}{R_0}\omega^*(k(t), q, \kappa) = \frac{\sqrt{2}}{R_0}\sqrt{\frac{T_e(s)}{m_i}}\omega^*(k(t), q, \kappa), \tag{4.6}$$

where $\omega^*(k(t), q, \kappa)$ describes the frequency dependence on the radial wavenumber, the safety factor and the elongation. One of the simplest analytical formulae for the GAM frequency has been shown in Eq. 3.66, derived in the case with adiabatic electrons. However, here we are going to use Eq. 4.1, obtained from the GK simulations with drift-kinetic electrons, although their effect on the GAM frequency is much smaller than on the wave damping rate. The safety factor profile is taken to be flat, and a deuterium plasma with a circular cross-section is considered: $\kappa = 1.00$, $r \approx as$.

The damping rate is defined as

$$\gamma(s_0, t) = \frac{1}{E(s_0, t)}\frac{\mathrm{d}E(s_0, t)}{\mathrm{d}t}. \tag{4.7}$$

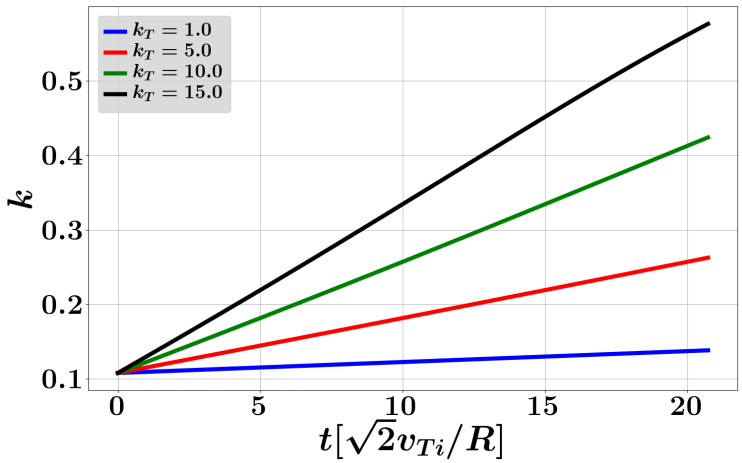

Figure 4.5: Typical evolution in time of the GAM radial wavenumber in the presence of different temperature gradients. The curves are calculated analytically using Eq. 4.10, where the radial gradient of the wave frequency found from Eqs. 4.9 and 4.1. Here, the following parameters are used: $T_e = 70\ eV, \tau_e = 1, q = 4.0, \kappa = 1.0, B_0 = 2.0\ T, a = 0.5\ m, R = 1.65\ m$, initial normalised radial wavenumber $k_0 = 0.108$, and temperature gradients $k_T = [1, 5, 10, 15]$.

At the beginning of every time interval $[t_1, t_1 + \Delta t]$, new values of the damping rate $\gamma(s_0, t_1)$ and frequency $\omega(s_0, t_1)$ are found with the scaling formulae given in Eq. (4.2) and (4.1), using the current value of the wavenumber $k(s_0, t_1)$. The new value of the electric field can be found, assuming that the damping rate is constant within the lapse of time $[t_1, t_1 + \Delta t]$:

$$E(s_0, t_1 + \Delta t) = E(s_0, t_1) \cdot (1 + \gamma(s_0, t_1)\Delta t). \tag{4.8}$$

After that, the new value of the wavenumber $k(s_0, t_1 + \Delta t)$ is calculated using the radial derivative of the frequency. Considering the case with a flat safety factor profile and radially constant magnetic field elongation, one gets from Eq. 4.6

$$\left.\frac{\partial \omega(s, t_1)}{\partial s}\right|_{s=s_0} = -\frac{1}{2}\omega(s_0, t_1)k_T, \tag{4.9}$$

where the factor $1/2$ comes from the radial derivative of the sound speed $\sim \sqrt{T_e(s)}$. With that, the wavenumber is assumed to change linearly in time as [16]

$$k(s_0, t_1 + \Delta t) = k(s_0, t_1) - \sqrt{2}\rho^* \left.\frac{\partial \omega(s, t_1)}{\partial s}\right|_{s=s_0} \Delta t. \tag{4.10}$$

Eq. 4.10 indicates that the mode radial wavenumber grows in time because of the radial dependence of the GAM frequency (Eq. 4.9) that takes place due to the temperature gradient (Fig. 4.5). Another option is to estimate the time evolution of the radial wavenumber directly from numerical calculations in ORB5 (red triangles in Fig. 4.4) instead of applying the analytical equation 4.10. Substituting the new value of the normalised wavenumber $k(s_0, t_1 + \Delta t)$ into Eq. (4.2), we can find the damping rate $\gamma(s_0, t_1 + \Delta t)$ at the next time point. To sum up, by using Eqs. 4.1 and 4.2 to know respectively the frequency and damping rate dependence on the mode radial wavenumber, and by applying these formulae in Eqs. 4.8 and 4.10, one can analytically calculate the evolution in time of the electric field, from which the mode half-decay time can be found.

The results obtained with this reduced theoretical model are shown in Fig. 4.4. The dependence of the half-decay time on the temperature gradient matches reasonably well the gyrokinetic simulations and the analytical theory. The difference is due to the global dynamics of the ORB5 simulations, which is compared here with a theory where the phase mixing follows a local estimation given in [16].

4.3 Collisional damping

Another possible mechanism of the GAM damping is the collisional processes. The collisional GAM damping is rarely discussed since it should be less relevant in the core region than the collisionless mode decay. On the other hand, the GAMs are often observed in the edge region where the plasma temperature is reduced, and since that, the plasma collisions are enhanced. Their contribution can be estimated using the formulae derived by Gao in [31], where GK theory of the ion plasma with adiabatic electrons is considered. It means that only the ion-ion collisions are taken into account. To find the GAM collisional damping, the right hand side of the GK equation similar to Eq. 3.24 is completed with a collision operator. After that, one derives the GAM dispersion relation for the mode complex frequency, where the imaginary part of the frequency includes the Landau and collisional parts. In particular, in [31], the so-called BGK (Bhatnagar-Gross-Krook) collision operator [77]

with particle conservation[3] is used

$$C_K = i\nu_i \left(\frac{n(t,\boldsymbol{r})}{n_0(\boldsymbol{r})} F_{0,i}(\boldsymbol{r},\boldsymbol{v}) - f(t,\boldsymbol{r},\boldsymbol{v}) \right), \tag{4.12}$$

where ν_i is the ion collision rate. In general, the collisions modify both mode frequency and damping rate, but we are interested here only in the latter one. Introducing the normalised ion collision rate $\hat{\nu}_i = \nu_i q R_0 / v_{Ti}$, the collisional damping rate is calculated according to [31] as

$$\frac{\gamma^{col}}{v_{Ti}/(qR_0)} = -\frac{3\hat{\nu}_i}{14 + 8\tau_i}, \tag{4.13}$$

if $\hat{\nu}_i \ll 1$, and as

$$\frac{\gamma^{col}}{v_{Ti}/(qR_0)} = -\frac{3}{8}\hat{\nu}_i \left(\frac{7}{4} + \tau_i + \frac{\hat{\nu}_i^2}{q^2} \right)^{-1}, \tag{4.14}$$

if $\hat{\nu}_i \geq q$. Here, $\tau_i = T_i/T_e$. To find the ion collision rate, we use classical expressions (see [78], page 33):

$$\nu_i[s^{-1}] = 4.8 \cdot 10^{-8} Z^4 (m_i/m_p)^{-1/2} n_i[cm^{-3}] T_i[eV]^{-3/2} \ln\Lambda, \tag{4.15}$$

$$\ln\Lambda = 23 - \ln\left[\sqrt{2 n_i[cm^{-3}]} \frac{Z^3}{T_i[eV]^{3/2}} \right], \tag{4.16}$$

where the ion species are assumed to be near Maxwellian. According to Eq. 4.13, the mode damping due to the collisions generally increases with the growth of the ion collision rate $\hat{\nu}_i$. However, the tendency is reversed when the rate becomes comparable with the sound frequency $v_{v_{Ti}}/R_0$ (Eq. 4.14). One can see that the collisional damping significantly depends on the ion temperature profile, and as it is shown in Sec. 4.4, generally becomes noticeable only at the very edge of the plasma system.

[3]The particle (density) conservation means that the zero moment of the GK (Vlasov) equation has to be equal to zero

$$\frac{\mathrm{d}\int f(t,\boldsymbol{r},\boldsymbol{v})\,\mathrm{d}\boldsymbol{v}}{\mathrm{d}t} = \int C_K\,\mathrm{d}\boldsymbol{v} = 0 \tag{4.11}$$

that results in the $n(t,\boldsymbol{r})/n_0(\boldsymbol{r})$ term in front of the equilibrium distribution function $F_{0,i}(\boldsymbol{r},\boldsymbol{v})$ in Eq. 4.12.

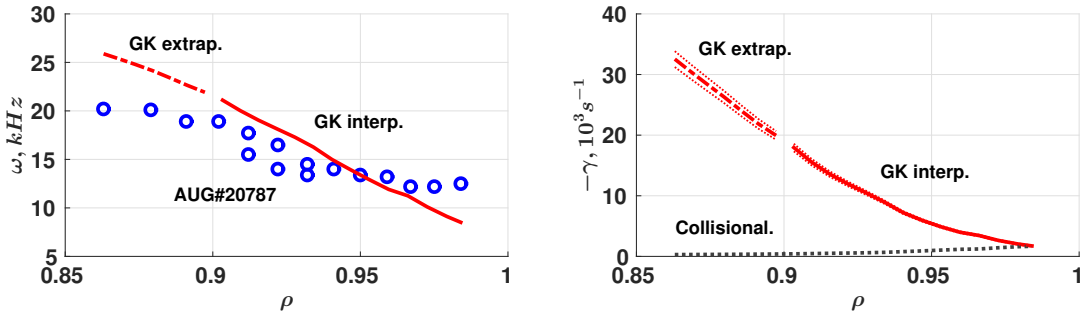

Figure 4.6: Left plot: comparison of the experimental GAM frequency [49] to Eq. 4.1. Right plot: Landau (red line, according to Eq. 4.2) and collisional damping (grey line, according to Eq. 4.13) rates. Here, $\rho = \psi/\psi_{edge}$ is the radial coordinate. *Reprinted with permission from [34], with permission from AIP Publishing.*

4.4 GAM linear frequency and damping spectra in ASDEX Upgrade

The fitting formulae obtained in Eqs. 4.1, 4.2 as the interpolation of the performed gyrokinetic simulations in Sec. 4.1 can be used to compare the GAM frequency obtained from the numerical estimations and from measurements, performed on ASDEX Upgrade tokamak [49]. More precisely, we consider the discharge AUG#20787 with the plasma elongation at the edge $\kappa = 1.09$ assuming that it is constant in the considered radial region $\rho = \psi/\psi_{edge} = [0.8, 1.0]$. The GAM radial wavenumber is considered to be constant and is estimated to be $k_r a = 40\pi$ from the experimental radial profile of the GAM amplitude (see Fig. 5f in [49]). Experimental safety factor and ion temperature profiles are taken to calculate the GAM frequency and damping rate using the scaling formulae Eqs. 4.1, 4.2 and Eq. 4.13 at different radial points ρ.

In Fig. 4.6, the GAM experimental frequency spectrum with the numerical estimation are depicted. A good general agreement is found in the central region of interest, where the GAM intensity, measured in the experiments, is peaked. However, the interpolating equation 4.1 cannot explain neither the staircase nature of the frequencies nor the GAM peak splitting that is observed experimentally, for example, at the radius positions $\rho = 0.922$ or $\rho = 0.932$. We should note that the presence of a GAM global spectrum has been suggested by simplified analytical models in [79, 80]. Nevertheless, taking account our numerical results, we can conjecture that the global GAM spectrum must have a nonlinear origin (see Sec. 8.2). We also notice that it is

consistent with GENE nonlinear simulations in [52].

Finally, we can compare the GAM Landau damping with collisional one. According to Fig. 4.6, the collisional damping is found to be negligible in the radial domain where the GAMs are experimentally measured. It is only in a very narrow region close to the plasma edge that the order of magnitude of the collisional damping is comparable to that of the Landau damping.

4.5 Chapter summary

This chapter has presented a numerical investigation of the dominant damping mechanisms of geodesic acoustic modes. Landau damping on thermal ions is one of the main damping processes since characteristic ion frequencies lie in the domain of GAM frequency. However, using plasma parameters close to those of ASDEX Upgrade near the plasma edge, it has been demonstrated that the inclusion of electron dynamics can significantly increase the mode damping rate keeping the GAM frequency practically unchanged. This result is confirmed in Chapter 6 and Chapter 7, where the same tendency is observed in linear and nonlinear EGAM dynamics.

The phase mixing process has also been analytically and numerically analysed in this chapter. Generally, GAMs have a continuum frequency spectrum, where the wave frequency depends on plasma temperature and safety factor profiles and therefore varies in the radial direction. Moreover, the GAM damping rate significantly increases with the rise of the radial wavenumber (Eq. 4.2, Fig. 4.3). Due to that, a finite temperature gradient and magnetic shear ($s\partial_s \ln(q)$) lead to the evolution of the GAM wavenumber in time, and as a result, to an increase of the mode damping rate.

Finally, using ASDEX Upgrade temperature profiles, the collisional GAM damping has been estimated and has been found to be negligible in comparison to the Landau damping, except a narrow region close to the plasma edge.

Chapter 5

Mode-Particle-Resonance diagnostic

In Chapter 4, it has been shown that including electrons as a kinetic species in gyrokinetic simulations, one can significantly increase the damping rate of the geodesic acoustic modes as compared to the case of adiabatic electrons. To understand why the GAM damping by electrons takes place and in general the role of electrons in the damping process, one should investigate the mode - electron interaction in velocity space. The power balance diagnostic (Sec. 2.3) is extended to localise the wave-particle resonances in velocity space. The resulting diagnostic is called Mode-Particle-Resonance (MPR) technique and is presented in Sec. 5.1. In Sec. 5.2, we explain how to work with the developed diagnostic, and localise the GAM-thermal ion resonances in velocity space. In Sec. 5.3, the diagnostic is analytically verified. It is shown that the GAM damping rate calculated by the MPR is consistent with the mode dispersion relation derived in Chapter 3. The MPR diagnostic is used later in Chapter 6 and Chapter 7 to investigate the EGAM linear and nonlinear dynamics. This chapter is based on material published in [58].

5.1 Implementation

In the MPR diagnostic we consider the electric field interaction with plasma particles. The magnetic potential perturbation $A_{\parallel}$ is omitted. As it has been mentioned in Sec. 2.3, a precise form of the GK energy transfer signal, valid in both linear and nonlinear cases, can be derived from the GK Hamiltonian using the Noether

theorem [57]:

$$\mathcal{P} = -Ze \int_V \mathrm{d}V \int_W \mathrm{d}W (f_0 + \delta f) \dot{\boldsymbol{R}}_0 \cdot \boldsymbol{\nabla}(J_0 \Phi), \tag{5.1}$$

where $\mathrm{d}W$ is defined in Eq. 2.5. The unperturbed particle trajectory $\dot{\boldsymbol{R}}_0$ can be obtained from Eq. 2.25 by eliminating all terms that include the field perturbation Φ. This means that the term Eq. 2.31 does not contribute to the energy transfer signal $\mathcal{P}$. The term involving the equilibrium distribution function f_0 in Eq. 5.1 gives a negligible contribution to the integral in the case of the Maxwellian or two-bumps-on-tail distribution functions discussed in Sec. 2.2, since they disappear during the integration over the real space[1]. Because of that, we are going to consider only the term related to δf. By integrating the signal over the whole real space V and in a small velocity domain ΔW, related to a particular velocity bin, we can analyse the energy exchange between fields and particles in that particular region of velocity space. In a PIC approach we have then

$$\mathcal{P} = -\frac{Ze}{N} \sum_{p \in V, \Delta W} w_p (\boldsymbol{v}_{p,\parallel} + \boldsymbol{v}_{p,\nabla B} + \boldsymbol{v}_{p,curvB} + \boldsymbol{v}_{p,\nabla p}) \cdot \boldsymbol{\nabla}(J_0 \Phi)|_p, \tag{5.2}$$

where the sum $\sum_{p \in V, \Delta W}$ is taken on all markers in the phase volume $V \Delta W$. The energy transfer is normalised in the following way:

$$\mathcal{P} = \frac{\mathcal{P}[W]}{T_e(s_{ref})[J] \omega_{ci}[s^{-1}]}, \tag{5.3}$$

where s_{ref} is the reference radial point. The gyro-averaged electric field $-\boldsymbol{\nabla}(J_0 \Phi)|_p$ is taken at a position of a marker p. The sum is normalised to the total number of species markers N in the whole phase-space domain. Since the GK model used in ORB5 is based on the Hamiltonian formulation, the momentum p_z, which has an explicit dependence on $A_\parallel$ according to Eq. 2.10, is used as one of the velocity variables. This is a common choice in most of the modern GK PIC codes. In the MPR diagnostic a variable u is used as a parallel velocity:

$$u = \frac{p_z}{m}. \tag{5.4}$$

In the ES case, the variables u and $v_\parallel$ are identical $u = v_\parallel$ (see Eq. 2.10), and in EM simulations with low β_e they are close $u \approx v_\parallel$. With the rise of β_e, the difference

[1] One can see it from Eq. 5.16, where f_0 would be used instead of the δf. In this case, the integral 5.24 turns to zero since it would have $\sin\theta$ instead of $\sin^2\theta$.

between these two variables increases because of the contribution of the parallel magnetic potential $A_\parallel$. A proper transition from the variable p_z to the variable $v_\parallel$ (instead of u) is necessary for the investigation of the dynamics of EM modes and for proper analysis of EM simulations. This transition is not implemented yet (it requires explicit calculation of the time derivative of $A_\parallel$), but it should be done in the near future to use the MPR technique to investigate resonances between plasma and EM modes, such as Alfvén waves.

5.2 Post-processing: application to a simplified GAM case

To describe the post-processing of the signals, given by the MPR diagnostic, we apply it to a linear GAM simulation, where a circular magnetic configuration is considered. A deuterium plasma with flat safety factor $q = 1.5$, flat density and temperature radial profiles is investigated. The temperature is defined by the value of $\rho^* = 1/205$. The simulation is performed electrostatically with adiabatic electrons, and the MPR diagnostic is applied only to the ions. Non-zonal modes, i.e. modes with toroidal numbers $n \neq 0$, are filtered out. Background magnetic field at the magnetic axis is $B_0 = 2.0\ T$, the minor and major radii are $a_0 = 0.5\ m$, $R_0 = 1.65\ m$ respectively. To reduce the computational effort, a radial domain $s = [0.5, 1.0]$ is simulated. The space resolution is $n_s = 300, n_\chi = 64, n_\phi = 4$, the time step is $dt[\omega_{ci}^{-1}] = 10$, and the number of the ion markers is $N_i = 10^8$. As in Chapter 4, to excite a GAM the Rosenbluth-Hinton test [9] is performed by introducing an axisymmetric density perturbation designed to produce the desired initial electric potential.

First of all, the MPR diagnostic provides the energy transfer signal $\mathcal{P}(v_\parallel, \mu, t)$ (Eq. 5.2) as a function of the velocity variables $(v_\parallel, \mu)$ and time. By averaging this signal on several GAM periods, resonances of the mode-particle interaction can be localised in velocity space. Location of such resonances of the order m can be analytically estimated as

$$v_{\parallel,res}^{(m)} = \frac{qR_0\omega_{GAM}}{m}, \tag{5.5}$$

where m is the poloidal mode number of the plasma density, ω_{GAM} is the GAM frequency that can be found directly from the zonal electric field $\overline{E}_r$. By integrating in corresponding velocity domains, one can estimate contribution of these resonances to the mode dynamics. In this particular case, it can be seen from Fig. 5.1, that the

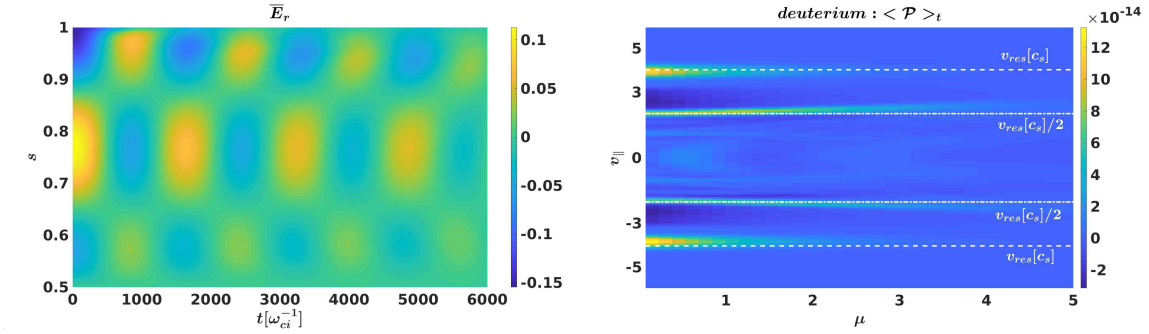

Figure 5.1: Left plot: evolution in time of the GAM radial electric field. Right plot: velocity dependence of the energy transfer signal averaged on several GAM periods. White dashed and dotted lines indicate the analytical estimation of the parallel velocities where the GAM-plasma resonance should be observed according to the analytical expression Eq. 5.5. The parallel velocity here is normalised to the sound velocity $c_s = \sqrt{T_e/m_i}$, and the magnetic moment is normalised to $m_i c_s^2/(2B_0)$. *Reprinted with permission from [58], with permission from Elsevier Publishing.*

energy exchange occurs at the first and second order resonances. By integrating the signal in the whole velocity domain, one gets the time evolution of the heating rate $\mathcal{P}$. The GAM damping rate can be estimated using Eq. 2.64. Following the algorithm, which was described in [58], one can eliminate the stationary zonal flow component in the energy transfer and field energy signals. The corresponding signals are shown in Fig. 5.2. From this plot, one can see that the elimination of the stationary zonal flow from the MPR signals reduces the asymmetry in the signals' oscillations (compare, for example, the red and greed lines in the left plot in Fig. 5.2).

Since here we are dealing with oscillating signals, we should use Eq. 2.64, which involves the integration in time. Varying and choosing different time intervals, one can estimate an errorbar of the GAM damping rate by building a distribution (or histogram) of the damping rate values. Every chosen time interval has to contain an integer number of GAM periods. The resulting histogram can be fitted with the normal distribution function that gives a mean value of the damping rate $\overline{\gamma}$, while the errorbar is estimated as 1.96σ, where σ is the standard deviation found from the distribution function. The number 1.96 is the 0.975 quantile of the standard normal distribution [81]:

$$P(-1.96\sigma < \gamma - \overline{\gamma} < 1.96\sigma) = 0.95, \tag{5.6}$$

where P is the probability to find the value of the damping rate in the range $[\overline{\gamma} -$

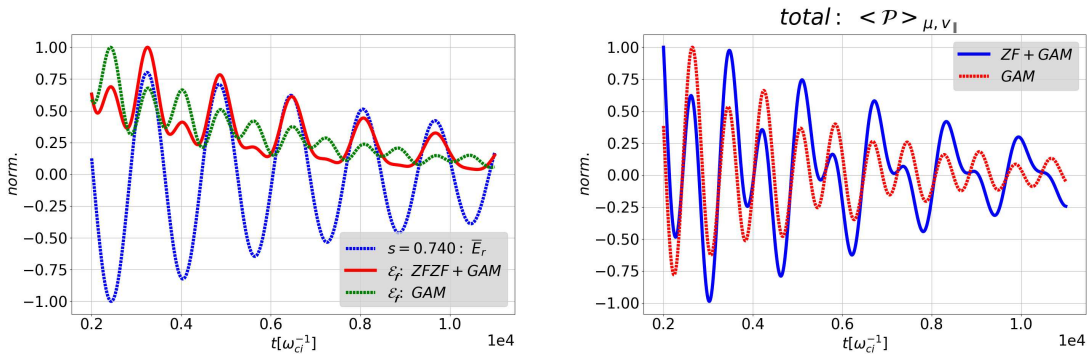

Figure 5.2: Left plot: evolution in time of the field energy signal with zero-frequency zonal flows (ZFZF) and GAM components (red line) and with only GAM component (green line) is plotted. For comparison, the zonal radial electric field at $s = 0.74$ is shown as well (blue line). Right plot: the raw energy transfer signal (blue line), which has both ZFZF and GAM components, and the one without the ZFZF component (red line) are presented. The energy transfer signals are integrated over the whole velocity and space domains. *Reprinted with permission from [58], with permission from Elsevier Publishing.*

$1.96\sigma, \overline{\gamma} + 1.96\sigma]$. Another more conservative method to estimate the errorbar is to take the half-width of the area covered by the damping rate distribution. The resulting value of the GAM damping rate found from the MPR diagnostic is

$$\gamma[\omega_{ci}] = -1.1 \cdot 10^{-4} \pm 1.5 \cdot 10^{-5}, \tag{5.7}$$

and the distribution of the GAM damping rate values is shown in Fig. 5.3 (the histogram has around 100 samples.). Here, values of the errorbar found from the normal distribution function and directly as a half-width of the area of the damping rate distribution are the same.

The result from the MPR diagnostic can be compared with the direct calculation of the GAM damping rate by fitting the zonal radial electric field $\overline{E}_r$ to a test function. We investigate the zonal signal $\overline{E}_r$ at $s = 0.74$, where the geodesic mode is localised (Fig. 5.1). As the first step, the GAM frequency is estimated by the Fast Fourier Transform, while the damping rate is estimated by the linear least-square root method from the peaks in the time evolution of $\overline{E}_r$. This preliminary processing gives the first assumption of the GAM dynamics used as an initial guess

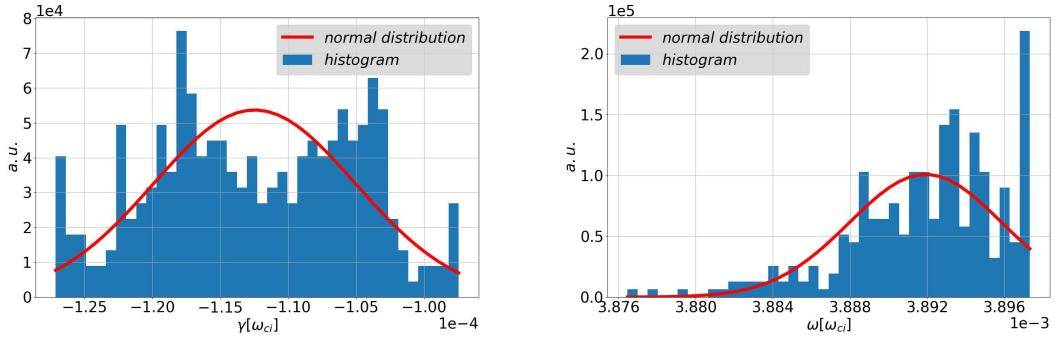

Figure 5.3: Left plot: distribution of the GAM damping rate from the MPR diagnostic. Right plot: a histogram of the GAM frequency found from the non-linear fitting of $\overline{E}_r(s = 0.74)$ to the test function Eq. 5.8. *Reprinted with permission from [58], with permission from Elsevier Publishing.*

in the non-linear fitting procedure[2], where a function

$$\sim \cos(\omega t) \exp(\gamma t) \tag{5.8}$$

is applied as a test one, and is fitted to the time evolution of $\overline{E}_r(s = 0.74)$. The same method has been used in Sec. 4.1 to calculate GAM frequency and damping rate in different plasma regimes. The errorbars of the wave frequency and damping rate are estimated by varying time intervals as it is done in the MPR diagnostic. To exclude outliers during the non-linear fitting, we compare the final results with the preliminary estimation of the frequency and damping rate and exclude values, which are significantly different from the preliminary guesses. The GAM frequency and damping rate found from the non-linear fitting are

$$\omega[\omega_{ci}] = 3.89 \cdot 10^{-3} \pm 7.8 \cdot 10^{-6}, \tag{5.9}$$
$$\gamma[\omega_{ci}] = -1.1 \cdot 10^{-4} \pm 8.3 \cdot 10^{-6}. \tag{5.10}$$

A histogram (distribution function) for the GAM frequency is shown in Fig. 5.3. As it can be seen here, the calculation of the GAM frequency is quite precise with an errorbar being around 0.3%, while the errorbar of the damping rate prediction is around 8%. Comparing both methods (Eq. 5.7 and 5.10), one can see that the MPR diagnostic is not as precise as the non-linear fitting, at least, in case of the calculation

[2]The Levenberg-Marquardt algorithm is used here (see Sec. 15.5.2 in [82]).

of the GAM damping rate. On the other hand, its strength is the fact that it provides additional information such as a position of the GAM-plasma resonances in velocity space (Fig. 5.1).

5.3 Analytical verification

Here, we would like to show the consistency of the MPR diagnostic with the analytical dispersion relation, derived previously in Chapter 3. In this section, we omit species indices since all relevant plasma variables are related to the deuterium. A GAM, as a standing wave, is described by the evolution of the zonal electric field:

$$\overline{\mathbf{E}} = (\overline{E}_r, 0, 0), \tag{5.11}$$

$$\overline{E}_r = E_1 \cos(kr) \exp(-i\hat{\omega}t), \tag{5.12}$$

with a radial wavenumber k and a complex frequency $\hat{\omega} = \omega + i\gamma$ that verifies the dispersion relation Eq. 3.64, E_1 is the GAM amplitude. To derive the expression for the energy transfer signal (Eq. 2.52), we consider, first of all, the linear ES version of the particle equation of motion presented in Eq. 3.14. Using Eq. 1.24, one gets

$$\dot{\boldsymbol{R}}_0 \cdot \overline{\boldsymbol{E}} = -v_d \overline{E}_r \sin\theta, \tag{5.13}$$

where v_d being the magnetic drift (as in Eq. 1.54)

$$v_d = \frac{mc}{eB_0R_0}\left(\frac{v_\perp^2}{2} + v_\parallel^2\right). \tag{5.14}$$

Since the energy transfer signal is the real variable, we have:

$$\mathcal{P} = e\int \mathrm{d}V\, \mathrm{d}W\, Re[\delta f] Re[\dot{\boldsymbol{R}}_0] \cdot Re[\overline{\boldsymbol{E}}], \tag{5.15}$$

and taking into account Eq. 5.13, one gets:

$$\mathcal{P} = -e\int \mathrm{d}V\, \mathrm{d}W\, v_d Re[\delta f] Re[\overline{E}_r] \sin\theta, \tag{5.16}$$

where v_d is the real variable. Now, we need to know also the form of the perturbed distribution function δf that satisfies the GAM dispersion relation Eq. 3.64. We are interested only in the non-adiabatic component[3] δK of the distribution function

[3]The adiabatic component of the perturbation does not contribute to the power exchange due to the reason explained in the footnote in Sec. 5.1.

(Eq. 3.25) that takes part in the power exchange expression. In Eq. 5.16, one performs the integration in space, including the integration along the poloidal direction. In case of the GAM dynamics, $\dot{\mathbf{R}}_0 \cdot \mathbf{E} \sim \sin\theta$, as one can see in Eq. 5.13. Because of that, the terms in δK proportional to $\cos\theta$ do not contribute to the power exchange. In other words, we do not consider δK_c (see Eq. 3.34), but only the term δK_s:

$$\delta f = \delta K_s \sin\theta. \tag{5.17}$$

By combining Eqs. 3.57, 3.58 and 3.37, one gets the final expression for the distribution perturbation

$$\delta f = \frac{e}{T}\frac{i\hat{\omega} f_0}{\hat{\omega}^2 - \omega_{tr}^2}\left(\frac{2cT}{eB_0R_0}\frac{N(z)}{D(z)} - v_d\right)\overline{E}_r \sin\theta. \tag{5.18}$$

Considering now the integration in velocity and using still complex variables, one obtains that

$$\int \mathrm{d}W v_d \delta f = \frac{e}{T}(I_1 - I_2)\overline{E}_r \sin\theta, \tag{5.19}$$

$$I_1 = i\hat{\omega}\frac{2cT}{eB_0R_0}\frac{N(z)}{D(z)}\int \frac{f_0 v_d}{\hat{\omega}^2 - \omega_{tr}^2}\,\mathrm{d}W, \tag{5.20}$$

$$I_2 = i\hat{\omega}\int \frac{f_0 v_d^2}{\hat{\omega}^2 - \omega_{tr}^2}\,\mathrm{d}W. \tag{5.21}$$

Evaluating the velocity integrals I_1 and I_2, one gets the expression

$$I_1 - I_2 = -i\frac{u_{th}^2}{\omega_c^2}\frac{u_{th}q}{R_0}\left(\frac{N^2(z)}{D(z)} - F(z)\right). \tag{5.22}$$

It is easy to reformulate the previous expression in terms of the GAM dispersion relation (Eq. 3.64):

$$I_1 - I_2 = -i\frac{u_{th}^2}{\omega_c^2}\hat{\omega}. \tag{5.23}$$

Using Eq. 5.16, one can derive the expression for the energy transfer signal:

$$\mathcal{P} = -E_1^2\frac{mc^2}{B_0^2}(\gamma + \gamma\cos(2\omega t) + \omega\sin(2\omega t))\exp(2\gamma t) \int \mathrm{d}V \sin^2\theta\cos^2(kr). \tag{5.24}$$

On the other hand, the wave energy is taken from Eq. 2.58:

$$\mathcal{E}_f = \frac{mc^2}{2B_0^2}\int \mathrm{d}V|\nabla_\perp \Phi|^2, \tag{5.25}$$

where we are dealing only with real signals. Finally, taking into account the perturbation of the zonal radial electric field $|\nabla_\perp \Phi|^2 \approx \overline{E}_r^2$, we get

$$\mathcal{E}_f \approx \frac{mc^2}{4B_0^2}E_1^2(1+\cos(2\omega t))\exp(2\gamma t)\int \mathrm{d}V \cos^2(kr). \tag{5.26}$$

The GAM damping rate can be found using Eq. 2.64 that leads to the following expression

$$\gamma^{MPR} = 2\left(\gamma + \frac{\omega}{n_w T_{gam}}\int \frac{\sin(2\omega t)}{1+\cos(2\omega t)}\,\mathrm{d}t\right)\frac{\int \cos^2(kr)\sin^2\theta\,\mathrm{d}V}{\int \cos^2(kr)\,\mathrm{d}V}. \tag{5.27}$$

The ratio of the space integrals is equal to 1/2. Taking into account Eq. 2.65, we finally can prove the consistency between the GAM dispersion relation and the MPR method:

$$\gamma^{MPR} = \gamma. \tag{5.28}$$

The expression 5.28 means that using the field and plasma perturbations (Eq. 5.12 and Eq. 5.18), which satisfy the GAM dispersion relation Eq. 3.64, in the MPR diagnostic (Eq. 2.64), one obtains the same damping rate originally found as the imaginary part of the GAM dispersion relation.

5.4 Chapter summary

In this chapter, we have presented the implementation of the Mode-Particle-Resonance diagnostic to investigate the interaction of the geodesic modes with plasma particles. The diagnostic is based on resolving the energy transfer signals in velocity space. This allows us to localise wave-particle resonances. This technique is used in Chapter 6 to demonstrate the EGAM excitation by energetic ions and its damping by barely trapped electrons.

Detailed MPR post-processing has been presented here by considering the GAM dynamics with localisation of the GAM-ion resonances, and the GAM damping rate calculation. Finally, by using the GAM dispersion relation, the consistency of the power balance diagnostic, which underlies the MPR method, has been analytically verified.

Chapter 6

Linear dynamics of Energetic particle driven GAMs

The Mode-Particle-Resonance (MPR) technique presented in Chapter 5 is now applied in global GK simulations of the experimental AUG discharge described in Sec. 6.1 to study the interaction of Energetic-particle-driven GAM (EGAM) with fast and thermal species (Sec. 6.2). This mode is characterised by the oscillations of toroidally symmetric global radial ES field with a frequency comparable to that of the GAMs. The energetic particles (EPs) excite the mode through the inverse Landau damping, and the EPs are displaced from higher to lower energy range [83, 84]. In addition to the ion Landau damping, the GAMs are subject to the electron Landau damping [32, 33, 34, 35], as it was shown in Chapter 4. Here, we demonstrate that the EGAMs are also subject to the electron Landau damping, which can be as crucial as the ion Landau damping in experimentally relevant conditions. Apart from that, inclusion of electron dynamics into GK simulations also modifies the energy transfer between the EGAM and both the energetic and thermal ions. Finally, to verify the obtained results, a comparison with the Eulerian gyrokinetic code GENE [85] is made in an electrostatic case with adiabatic electrons in Sec. 6.3. This chapter is based on material published in [58].

6.1 ASDEX Upgrade plasma configuration

The AUG discharge #31213 at time 0.84 s is selected within the Non-Linear Energetic-particle Dynamics (NLED) Eurofusion enabling research project [86, 87]. It is chosen to study the effect of the energetic particles on the dynamics of EGAMs. We are dealing here with three species: gyrokinetic thermal deuterium, gyrokinetic ener-

getic (fast) deuterium, and thermal electrons, either adiabatic (AE) or drift-kinetic (KE). The linear dynamics of EGAMs in this NLED-AUG case has been recently investigated with the gyrokinetic codes GENE and ORB5 by considering adiabatic electrons [88]. The previous study is extended here by investigating the effect of kinetic electrons and describing the contribution of the resonances of all species in phase space. The simulation with the AE is performed electrostatically, while the simulation with the KE is done including dynamics of the magnetic potential perturbation as well[1]. In this latter case the pullback method [56, 60] is used in EM simulations for the mitigation of the cancellation problem [89, 90] mentioned in Sec. 2.1. The essence of this problem is that in the Ampère law (Eq. 2.21), the non-physical skin depth terms $A_{\parallel}/d^2$, which arise due to the Hamiltonian representation, have to be cancelled with the adiabatic parts of the corresponding species currents from the left hand side. However, since the current terms are calculated with markers, while the skin depth terms are measured using finite elements, numerical inaccuracy leads to inexact cancellation of these terms. What makes the problem even worse is that absolute values of these non-physical terms is much higher than that of the physical terms on the right hand side. That is why even a small inaccuracy in the cancellation leads to a big error in the Ampère equation.

As it has been mentioned before, the pullback scheme can be used to mitigate the cancellation problem. It is based on the so-called mixed-variable formulation, where advantages of both Hamiltonian and symplectic formulations are taken into account. Thanks to a splitting of the magnetic potential on symplectic and hamiltonian components at the end of every time step, one can eliminate the non-physical terms in the Ampère law, while still using an explicit time solver to calculate the particle parallel acceleration.

Profiles of the safety factor, species density and temperature, used in the considered simulations, are shown in Fig. 6.1. The magnetic field is reconstructed from experimental data, including all geometrical effects (Fig. 6.1). The magnetic field at the magnetic axis is $B_0 = 2.2\ T$. The major radius at the axis is $R_0 = 1.67\ m$, the minor radius is $a_0 = 0.482\ m$. The real space of the system is discretized using the following parameters: $n_s = 256$, $n_\chi = 256$, $n_\phi = 32$. In the ES simulation, the time grid has a step $dt[\omega_{ci}^{-1}] = 20$. Number of markers for the thermal and fast ions are $N_i = N_f = 5 \cdot 10^8$. In the EM case, the time step and number of markers are changed: $dt[\omega_{ci}^{-1}] = 5$, $N_i = N_f = 10^8$, $N_e = 4 \cdot 10^8$. Such a high number of markers is needed to provide at least several thousands of numerical markers in every velocity bin, where the mode-plasma resonances are observed. In the EM case, the radial domain

[1] As it was indicated in Sec. 5.1, the MPR diagnostic can be applied in EM simulations with a small beta to study mainly ES modes such as the (E)GAMs.

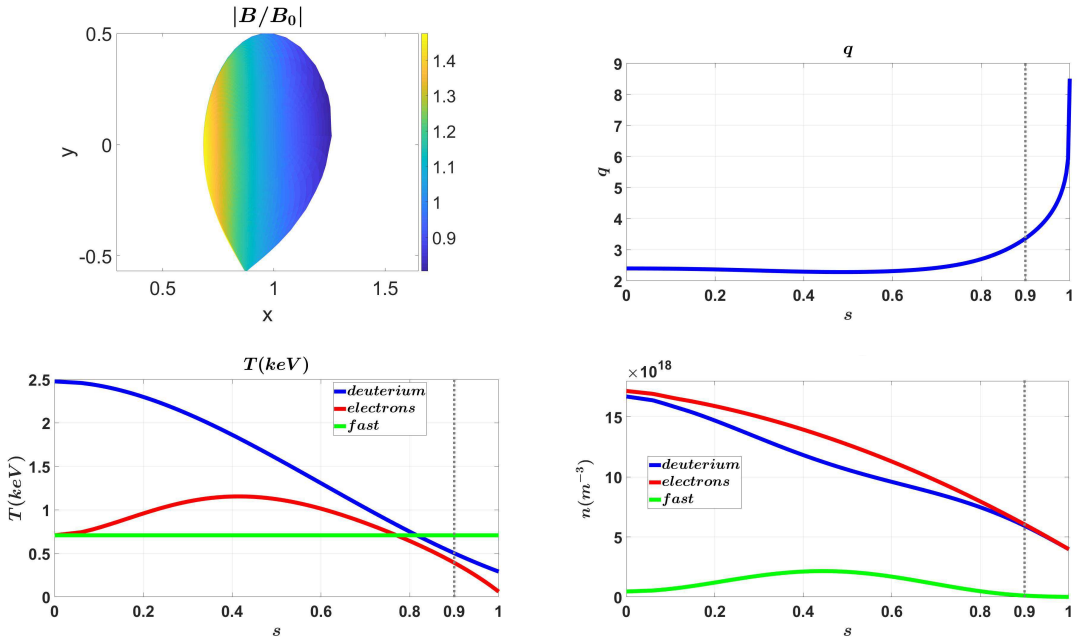

Figure 6.1: Magnetic configuration (upper left plot), radial profile of the safety factor (upper right plot), species temperature (lower left plot) and density (lower right plot) radial profiles for the EGAM simulations in the ASDEX Upgrade shot #31213 (see [86, 87]). The grey vertical dotted lines indicate the right boundary of the simulated radial domain in the EM case with drift-kinetic electrons. *Reprinted with permission from [58], with permission from Elsevier Publishing.*

is reduced to $s = [0.0, 0.9]$ to avoid numerical instabilities due to the abrupt increase of the safety factor at the edge. The density profile that is depicted in Fig. 6.1, corresponds to the case with $\beta_e = 2.7 \cdot 10^{-4}$. In both cases, the velocity distribution of the fast particles is described by the expression Eq. 2.38 with $u_H = 8$ and $T_H = 1$. This means that the distribution function of the fast species is centred around $v_\parallel = 8$ and $v_\parallel = -8$ (two bumps-on-tail) with maxima in $v_\parallel$ at ± 8 times the sound velocity, as one can see from Fig. 6.4 (grey line). Due to this shift in the parallel velocity, the fast particles lie near the EGAM-particle resonance velocity, which is estimated in Eq. 5.5, and can exchange energy with the zonal electric field. As a result, the term "fast" (or "energetic") is used here to identify species that are responsible for the EGAM excitation. More precisely, the energetic deuterium particles, which lie on the positive-gradient part of the right bump and negative-gradient part of the left bump, in total, transfer their energy to the electric field, driving in such a way

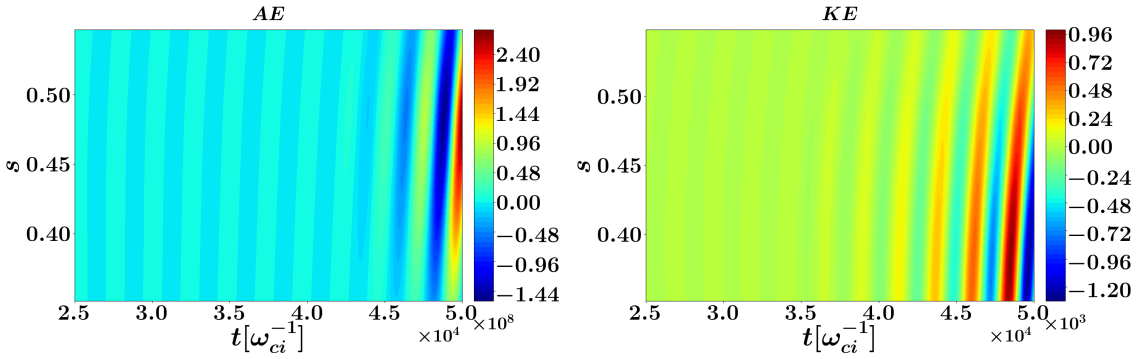

Figure 6.2: Comparison of the radial structure of $\overline{E}_r$ in simulations with adiabatic (left plot) and drift-kinetic (right plot) electrons.

the EGAMs (see Sec. 1.4). The width of these bumps is constant in space, which is described by the flat temperature profile of the fast species. The ORB5 simulation with such parameters of the energetic deuterium results in one of the highest EGAM growth rate for the given plasma configuration.

6.2 Role of the wave-particle interaction in the EGAM linear dynamics

At the beginning of every simulation presented in this section, we initialize the ion zonal density perturbation with a radial wavenumber $\sim a_0$, and we inject the energetic particles with the parameters described in the previous section. We would like to emphasize here that it is the EP parameters that define the dynamics of the resulting EGAM, while the initial density perturbation has a minor effect. First of all, one can notice from Fig. 6.2 that the radial structure of the EGAMs slightly changes when the dynamics of the drift-kinetic electrons is switched on. The position of the crest in the EGAM radial structure shifts inwards from around $s \sim 0.48$ to $s \sim 0.40$. Considering firstly the ES case with AE, we compare the EGAM frequency and growth rate, calculated at radial positions $s = 0.40$ and $s = 0.48$,

using the non-linear fitting of $\overline{E}_r$:

$$s = 0.40: \quad \omega[\sqrt{2}v_{th,i}/R_0] = 9.391 \cdot 10^{-1} \pm 3.5 \cdot 10^{-4}, \tag{6.1}$$
$$\gamma[\sqrt{2}v_{th,i}/R_0] = 1.63 \cdot 10^{-1} \pm 1.4 \cdot 10^{-3}, \tag{6.2}$$
$$s = 0.48: \quad \omega[\sqrt{2}v_{th,i}/R_0] = 9.314 \cdot 10^{-1} \pm 3.7 \cdot 10^{-4}, \tag{6.3}$$
$$\gamma[\sqrt{2}v_{th,i}/R_0] = 1.65 \cdot 10^{-1} \pm 1.4 \cdot 10^{-3}. \tag{6.4}$$

From here on, only the radial point $s = 0.40$ is considered in the following calculations. Consistency between the EGAM growth rate calculated directly from $\overline{E}_r$ and by the MPR diagnostic, using Eq. 2.64, significantly improves in time due to the growth of the EGAM signal in comparison with the zero-frequency zonal flow. Skipping initial transient time period, the MPR diagnostic can be applied to measure the EGAM growth rate that appears to be consistent with Eq. 6.2:

$$MPR: \ \gamma[\sqrt{2}v_{th,i}/R_0] = 1.63 \cdot 10^{-1} \pm 2.8 \cdot 10^{-3}. \tag{6.5}$$

The consistency between both methods is observed in the EM case with KE as well:

$$\overline{E}_r(s = 0.4): \quad \omega[\sqrt{2}v_{th,i}/R_0] = 9.586 \cdot 10^{-1} \pm 4 \cdot 10^{-4}, \tag{6.6}$$
$$\overline{E}_r(s = 0.4): \quad \gamma[\sqrt{2}v_{th,i}/R_0] = 8.5 \cdot 10^{-2} \pm 1.0 \cdot 10^{-3}, \tag{6.7}$$
$$MPR: \quad \gamma[\sqrt{2}v_{th,i}/R_0] = 8.4 \cdot 10^{-2} \pm 3.6 \cdot 10^{-3}. \tag{6.8}$$

From Eq. 6.1 and Eq. 6.6 one can see that the change in the EGAM frequency is small in comparison with the change in the growth rate, when dynamics of the drift-kinetic electrons is included. In particular, the EGAM growth rate decreases from Eq. 6.5 (AE) to Eq. 6.8 (KE). We now want to investigate the role of the drift-kinetic electrons in the EGAM dynamics to understand which wave-particle interactions lead to the decrease of the EGAM total growth rate, by estimating the contribution of different species. For that purpose, we consider different terms in Eq. 2.57 and Eq. 2.64. In the simulation with adiabatic electrons we obtain

$$thermal\ deuterium: \quad \gamma[\sqrt{2}v_{th,i}/R_0] = -2.99 \cdot 10^{-1} \pm 3.9 \cdot 10^{-3}, \tag{6.9}$$
$$fast\ deuterium: \quad \gamma[\sqrt{2}v_{th,i}/R_0] = 4.62 \cdot 10^{-1} \pm 2.3 \cdot 10^{-3}. \tag{6.10}$$

These equations show that the total EGAM growth rate is a balance between the drive on the fast species and damping on the thermal one (one can see also [38] for a similar analysis in the case of EGAMs in simplified configurations with adiabatic electrons). Moreover, the absolute values of the species contributions are significantly higher than the absolute value of the EGAM total growth rate.

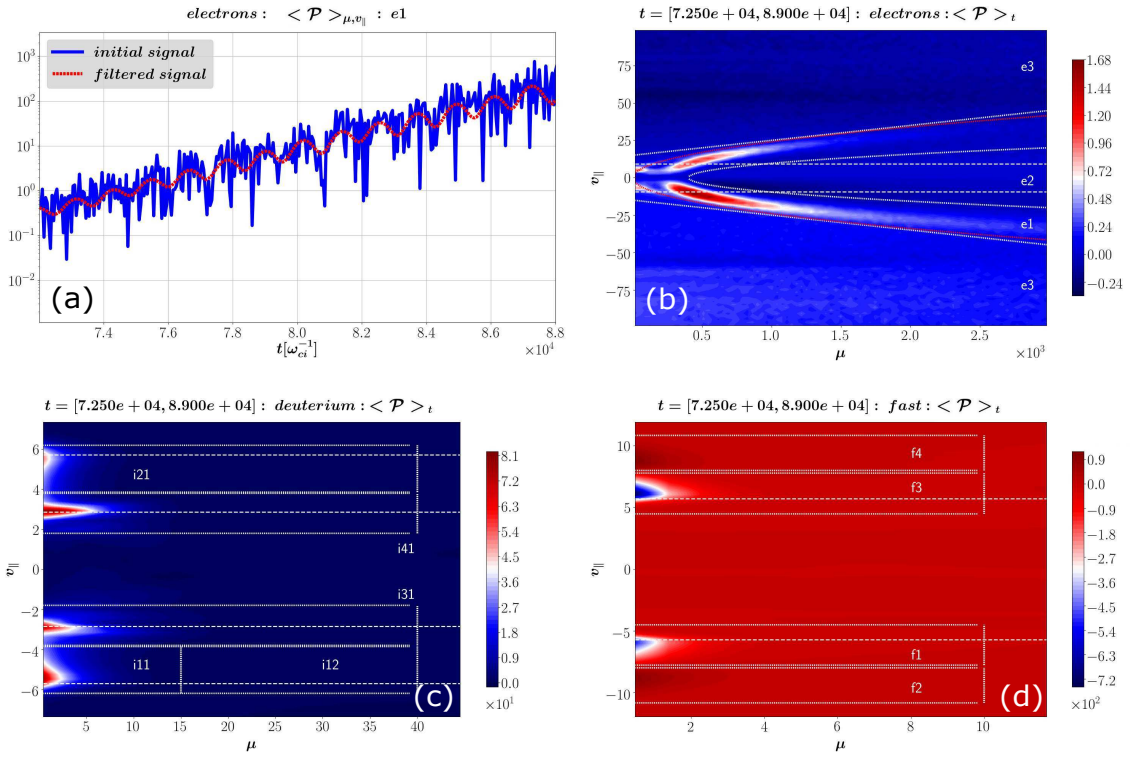

Figure 6.3: Energy transfer signal for electrons averaged on several EGAM periods with indication of different velocity domains is shown in Fig. 6.3b. The red cone indicates the analytical estimation of the passing-trapped boundary Eq. 6.14. The white horizontal dashed lines indicate analytical estimation of $m = 1$ EGAM-plasma resonance (Eq. 5.5). Fig. 6.3a: energy transfer signal integrated in the velocity domain $e1$. The blue line corresponds to the initial raw signal, while the red line shows the signal obtained after low-pass filtering. The energy transfer signals for the thermal (Fig. 6.3c) and fast (Fig. 6.3d) deuterium with indication of different velocity domains. The horizontal dotted lines indicate positions of the first $v_{\parallel,res}$ and second $v_{\parallel,res}/2$ order resonances found from Eq. 5.5. The parallel velocity here is normalised to the sound velocity c_s, and the magnetic moment is normalised to $m_i c_s^2/(2B_0)$. *Reprinted with permission from [58], with permission from Elsevier Publishing.*

In case with drift-kinetic electrons, the species contributions are the following:

$$thermal\ deuterium: \quad \gamma[\sqrt{2}v_{th,i}/R_0] = -3.94 \cdot 10^{-1} \pm 4.1 \cdot 10^{-3}, \tag{6.11}$$

$$thermal\ electrons: \quad \gamma[\sqrt{2}v_{th,i}/R_0] = -2.67 \cdot 10^{-2} \pm 4.6 \cdot 10^{-4}, \tag{6.12}$$

$$fast\ deuterium: \quad \gamma[\sqrt{2}v_{th,i}/R_0] = 5.03 \cdot 10^{-1} \pm 4.7 \cdot 10^{-3}. \tag{6.13}$$

From the above equations one can see that both drive by the fast particles (Eq. 6.10 and 6.13) and damping on the thermal ions (Eq. 6.9 and 6.11) increase with the inclusion of the electron dynamics. Since this increase is comparable with the electron contribution (Eq. 6.12), one cannot claim from these results that the decrease of the EGAM growth rate occurs only directly due to the additional damping on electrons. On the other hand, we observe that the inclusion of KE increases the damping on thermal ions more than the drive by fast ions, thus reducing the growth rate. As a consequence, the electron Landau damping, although small, turns out to have a non-negligible impact on the overall growth of the EGAM. Apart from that, the inclusion of drift-kinetic electrons changes the position of the EGAM crest (Fig. 6.2) and slightly changes the EGAM frequency. These changes might be responsible for the observed increase of the thermal and energetic ion contributions to the EGAM drive. Nevertheless, it is clearly shown here that in the experimentally relevant plasma conditions the inclusion of the drift-kinetic electrons significantly decreases the EGAM growth rate of about a factor 2.

We now want to investigate the role of different resonances in phase space. In Fig. 6.3b one can see the energy transfer signal for the EGAM-electron interaction in the velocity space averaged on several EGAM periods. The red cone there indicates an analytical estimation of the boundary between the passing and trapped electrons:

$$v_{\parallel}^{p-tr} = \sqrt{2\varepsilon\mu}, \tag{6.14}$$

obtained from Eq. 1.14, and where $v_{\parallel}^{p-tr}$ is normalised to c_s, while μ is normalised to $m_i c_s^2/(2B_0)$. According Fig. 6.3b, the EGAMs are damped by the electrons which are localised mainly near this boundary, similar to what happens with GAMs [32]. We should mention here that the estimated localisation of the passing-trapped boundary is shown in Fig. 6.3b only as a guide for the eye, and it is not used during the actual GK simulations. We can separate three different velocity domains $e1$, $e2$, $e3$. The area $e1$, which is between the passing-trapped boundary and the white parabola in Fig. 6.3b, describes mostly the contribution of the barely trapped electrons to the EGAM damping. The area $e2$, which is inside of the white parabola, corresponds to the deeply trapped electrons. Finally, the area $e3$, which is the velocity domain outside the passing-trapped boundary, describes the passing electrons. By integrating, for example, in the velocity domain $e1$, one gets the time evolution of the energy transfer signal (Fig. 6.3a) that should be smoothed for its proper use in Eq. 2.64.

The electron contributions from different velocity domains are the following:

$$e1: \quad \gamma[\sqrt{2}v_{th,i}/R_0] = -1.37 \cdot 10^{-2} \pm 3.9 \cdot 10^{-4}, \tag{6.15}$$
$$e2: \quad \gamma[\sqrt{2}v_{th,i}/R_0] = 2.5 \cdot 10^{-3} \pm 2.0 \cdot 10^{-4}, \tag{6.16}$$
$$e3: \quad \gamma[\sqrt{2}v_{th,i}/R_0] = -1.47 \cdot 10^{-2} \pm 2.3 \cdot 10^{-4}, \tag{6.17}$$
$$e1 + e2 + e3 \approx -2.59 \cdot 10^{-2}. \tag{6.18}$$

The sum of the electron contributions (Eq. 6.18) is close within the errorbars to the value found in Eq. 6.12[2]. First of all, we would like to note that one of the dominant components to the electron damping occurs due to the barely trapped electrons ($e1$). It is reasonable since the resonant velocity of the EGAM-electron interaction lies in the domain of the barely trapped electrons. On the other hand, we can see a significant contribution of passing electrons to the EGAM damping (Eq. 6.17). The reason might be in the choice of the velocity space variables employed in ORB5, as it has been explained in Sec. 5.1. More precisely, we have some contribution of the parallel magnetic potential to the velocity coordinate, used in the MPR diagnostic. To reduce this component, we can decrease the plasma β, as it is done in Appendix in [58] that leads to smaller contributions of passing and deeply trapped electrons to the field-electron interaction, keeping the same damping on barely trapped electrons.

We can also estimate contributions of different resonances to the EGAM damping by thermal ions (Fig. 6.3c):

$$i11: \quad \gamma[\sqrt{2}v_{th,i}/R_0] = -1.01 \cdot 10^{-1} \pm 3.4 \cdot 10^{-3}, \tag{6.19}$$
$$i12: \quad \gamma[\sqrt{2}v_{th,i}/R_0] = -1.02 \cdot 10^{-1} \pm 3.7 \cdot 10^{-3}, \tag{6.20}$$
$$i21: \quad \gamma[\sqrt{2}v_{th,i}/R_0] = -6.7 \cdot 10^{-2} \pm 2.7 \cdot 10^{-3}, \tag{6.21}$$
$$i31: \quad \gamma[\sqrt{2}v_{th,i}/R_0] = -9.6 \cdot 10^{-2} \pm 2.6 \cdot 10^{-3}, \tag{6.22}$$
$$i41: \quad \gamma[\sqrt{2}v_{th,i}/R_0] = -1.00 \cdot 10^{-1} \pm 1.4 \cdot 10^{-3}, \tag{6.23}$$
$$i12 + i21 + i31 + i41 \approx -3.65 \cdot 10^{-1}, \tag{6.24}$$

where the domain $i12$ includes $i11$, but extend further along μ. In Eq. 6.24 the contributions of all considered resonances are summed up. The resulting value is close enough[3] to the total contribution of the thermal ions (Eq. 6.11). From one point of view, it is an additional way to verify the implemented diagnostic. On the other hand, by comparing Eq. 6.19 and Eq. 6.20, one can see that the parallel

[2]The small difference can be explained by the necessity to perform the smoothing of the wave energy and energy transfer signals before applying Eq. 2.64.

[3]The small discrepancy can again be explained by the smoothing of the MPR signals.

ion dynamics has a predominant contribution to the energy exchange between the EGAMs and the thermal deuterium plasma.

Finally, we can consider different domains in the energetic deuterium velocity space (Fig. 6.3d):

$$f1: \quad \gamma[\sqrt{2}v_{th,i}/R_0] = 2.85 \cdot 10^{-1} \pm 4.78 \cdot 10^{-3}, \tag{6.25}$$

$$f2: \quad \gamma[\sqrt{2}v_{th,i}/R_0] = -7.11 \cdot 10^{-2} \pm 3.8 \cdot 10^{-3}, \tag{6.26}$$

$$f3: \quad \gamma[\sqrt{2}v_{th,i}/R_0] = 3.61 \cdot 10^{-1} \pm 6.3 \cdot 10^{-3}, \tag{6.27}$$

$$f4: \quad \gamma[\sqrt{2}v_{th,i}/R_0] = -6.7 \cdot 10^{-2} \pm 4.0 \cdot 10^{-3}, \tag{6.28}$$

$$f1 + f2 + f3 + f4 = 5.08 \cdot 10^{-1}. \tag{6.29}$$

One can see that there is an EGAM damping even on the energetic particles (Eq. 6.26 and Eq. 6.28). But it is significantly smaller than the dominant drive (Eq. 6.25 and 6.27). Sum on the resonances (Eq. 6.29) indicates that the EGAMs are driven by the fast species, and this sum is close enough to the total drive found in Eq. 6.13.

6.3 Comparison with GENE

To verify some of the obtained results in the ES case we perform a comparison with the gyrokinetic GENE code that has a similar diagnostic. The Gyrokinetic Electromagnetic Numerical Experiment (GENE) [85] is an Eulerian code, which solves the GK Vlasov-Maxwell system of coupled equations on a phase-space grid $(\mathbf{R}, v_\parallel, \mu)$ at each time step. The gyrokinetic description employs an approach based on the study of a distribution function $f_{sp}(\mathbf{R}, v_\parallel, \mu)$ for each plasma species, which contrarily as it is done in a particle-in-cell code as ORB5, is not discretized with markers.

The same AUG shot is simulated in GENE with adiabatic electrons (one can see also [91]), using the flux-tube (local) version of the code at $s = 0.5$. In Fig. 6.4, the blue curve indicates the inverse (with an opposite sign) energy transfer signal calculated in GENE[4], while the red curve presents the energy transfer obtained in ORB5. Both signals are integrated in real space and along perpendicular velocity. One can see that both ORB5 and GENE give the same positions of the resonances of the EGAM - fast deuterium plasma interaction. According to the chosen parameters of the fast deuterium distribution function, peaks of the energetic bumps are located at $|v_\parallel| = 8$. As a benchmark, comparison of the EGAM frequency and total growth

[4]The inversion just indicates the fact that in GENE and ORB5 the background magnetic field is directed in opposite directions with respect to the toroidal angle.

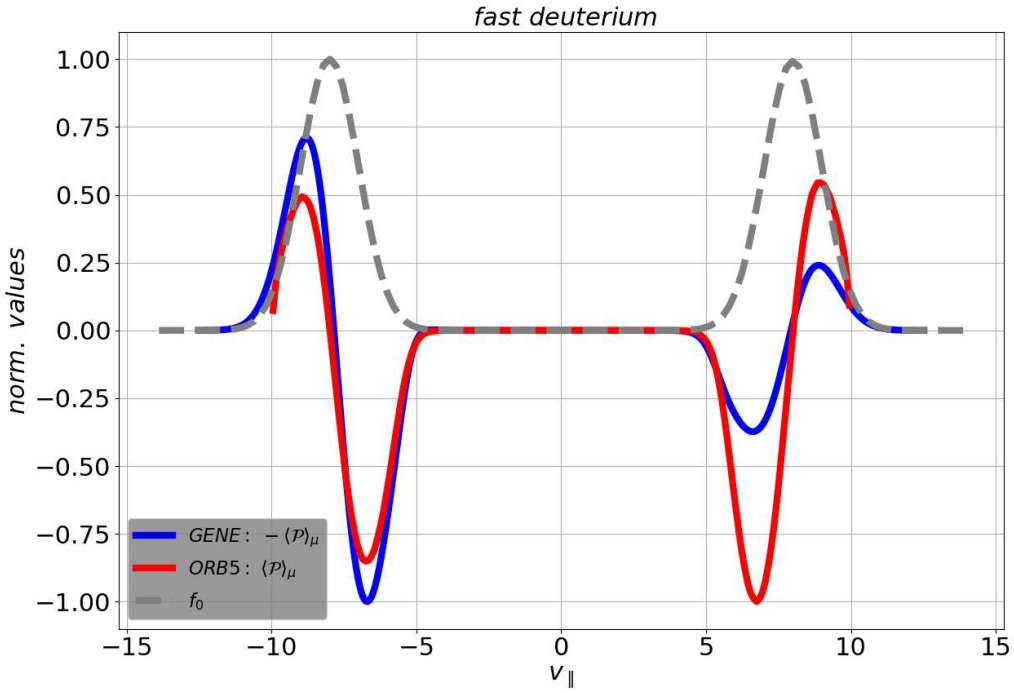

Figure 6.4: Resonance positions of the EGAM - fast deuterium interaction obtained from GENE and ORB5. The velocity grid is normalised to the sound speed c_s. The grey dotted line indicates the bumps' positions, which describe the equilibrium distribution of the energetic deuterium. *Reprinted with permission from [58], with permission from Elsevier Publishing.*

rate is made as well[5]. One can see that both codes give close values of the mode frequency:

$$GENE: \quad \omega/2\pi = 42\ (kHz), \tag{6.30}$$

$$ORB5: \quad \omega/2\pi = 43.60 \pm 0.02\ (kHz). \tag{6.31}$$

On the other hand, there is 18% difference between the codes for the EGAM total

[5]The main goal of this benchmark was to compare the GAM-ion resonance positions, and the corresponding wave frequency and damping rate. Having said that, we should note there are still other physical phenomena to explore in this linear ES plasma system. One of them is the asymmetry in the energy transfer signal (red line in Fig. 6.4) mainly observed in the local simulations with GENE, which is, however, out of scope of our investigation.

growth rate:

$$GENE: \quad \gamma = 40 \cdot 10^3 \ (s^{-1}), \tag{6.32}$$

$$ORB5: \quad \gamma = (47.6 \pm 0.4) \cdot 10^3 \ (s^{-1}), \tag{6.33}$$

and for the contributions of different plasma species to the mode dynamics:

$$thermal\ deuterium: \quad GENE: \ \gamma = -74 \cdot 10^3 \ (s^{-1}), \tag{6.34}$$

$$ORB5: \ \gamma = (-87 \pm 1) \cdot 10^3 \ (s^{-1}), \tag{6.35}$$

$$fast\ deuterium: \quad GENE: \ \gamma = 115 \cdot 10^3 \ (s^{-1}), \tag{6.36}$$

$$ORB5: \ \gamma = (134.8 \pm 0.7) \cdot 10^3 \ (s^{-1}). \tag{6.37}$$

The difference in the values can be explained mainly by the fact that the simulation in GENE is performed using the local flux-tube version, while the simulation in ORB5 is a global one.

6.4 Chapter summary

Geodesic acoustic modes, including the modes driven by energetic particles, are subject to the Landau damping, where the thermal ion dynamics has a dominant role. However, in this chapter, it has been shown that the EGAMs are also damped by barely trapped electrons, whose characteristic velocities are close to the EGAM-particle resonance. Moreover, a kinetic treatment of the electrons also modifies the energy transfer between the EGAM and both the fast and the thermal ions. The corresponding result has been obtained in GK simulations of a realistic ASDEX Upgrade discharge. It emphasizes the critical role of the electron dynamics for the accurate description of the (E)GAM behaviour in experimentally relevant plasma configurations. In Chapter 7, it is shown in nonlinear GK simulations that the inclusion of the drift-kinetic electrons has a direct influence on the bulk plasma heating by the geodesic modes as well.

Chapter 7

Nonlinear EGAM dynamics in ASDEX Upgrade

In this chapter, we are going to study nonlinear EGAM dynamics in the AUG discharge presented in Sec. 6.1. More precisely, here, we still consider only the zonal ($n = 0$) modes in our simulations. However, speaking about the nonlinearity, the particle characteristics (Eqs. 2.22, 2.23) will depend also on the field perturbations that allows exploring the mode saturation due to the flattening of the energetic particle distribution function. In Sec. 7.1, bulk plasma heating by the mode is investigated using the MPR diagnostic introduced in Chapter 5. Furthermore, in Sec. 7.2, we show that the code ORB5 can reproduce the relative EGAM up-chirping in the realistic AUG magnetic configuration, which is an essential step for the code validation.

The EGAMs can have a significant influence on the EP dynamics and the plasma confinement. First of all, being excited, this mode provides an additional mechanism of the energy exchange between the energetic particles and the thermal plasma [93, 84, 94, 95] due to the wave-particle interaction. Because of its interaction with the turbulence [96, 97], this mode might be used as an additional knob in the turbulence regulation. Significant progress has been made in the last decade in building a theoretical model that can explain the primary nonlinear physics of the EGAM [98, 20, 99]. Nevertheless, when one wants to compare quantitatively with experimental measurements, some of the approximations in the previous models can be limiting. For example, due to the importance of the wave-particle resonances with the thermal and energetic species, a kinetic treatment should be used as in [32, 52, 58]. Besides, the effect of the magnetic surface shape [88] can be considered by employing an experimental magnetic equilibrium. Here, the importance of these effects in an

experimental ASDEX-Upgrade case is investigated employing numerical simulations with the code ORB5. ORB5 has been previously used for nonlinear studies of the EGAMs in simplified configurations [100, 101], and it is used here to compare the nonlinear EGAM dynamics with experimental measurements.

Only the EGAM dynamics leaving aside its interaction with the turbulence is going to be considered here. It should be noted that in contrast to finite-n modes, which also can transfer energy from the EPs to the thermal plasma due to the wave-particle interaction, the EGAM dynamics are practically not associated with additional particle loss (at least, if one does not consider the mode propagation and topological orbital changes [102]).

We are going to investigate the EGAMs in the plasma configuration of the ASDEX Upgrade discharge #31213@0.84 s, which is described in Sec. 6.1, where a rich EP nonlinear dynamics is present. In this discharge, various types of EP-driven instabilities were identified, among which there are Alfvén instabilities (see, for example, [103]) and EGAMs. In particular, a bright EGAM chirping was observed. More precisely, at the experimental EGAM frequency spectrogram (Fig. 7.1) one can see at least two different branches of the EGAM evolution in time. A "short" one is with a ~ 2.5 ms period with the frequency rise from ~ 45 kHz till ~ 55 kHz. A "long" branch is characterised by an ascending frequency from ~ 45 kHz till ~ 58

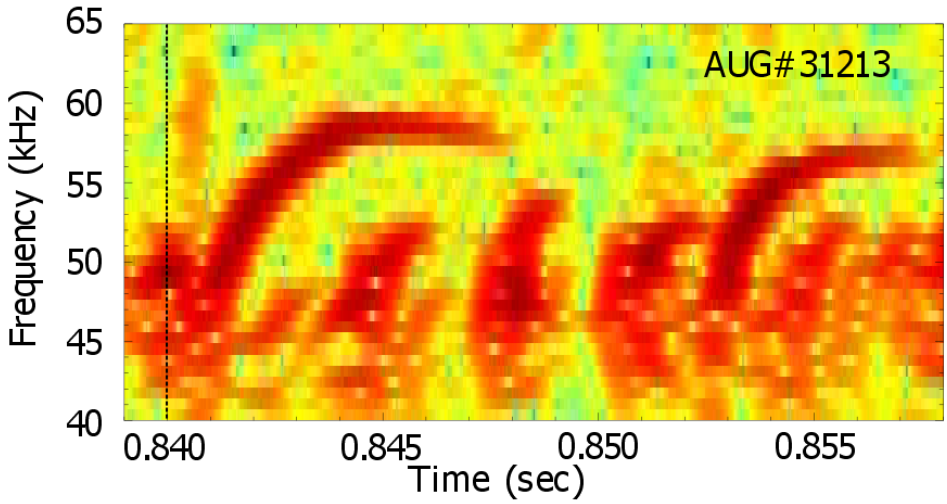

Figure 7.1: Experimental EGAM spectrum [87, 86] in the NLED AUG discharge #31213@0.84 s. *Reprinted with permission from [92], with permission from AIP Publishing.*

kHz and frequency saturation with a period of change around 13 ms.

Finally, by varying the EP parameters such as velocity or temperature, we are going to investigate how the EGAM saturation level depends on the energy exchange between the EPs and thermal plasma, and whether it is possible to enhance the plasma heating keeping the same EGAM level. The materials presented in this chapter is based on [92].

7.1 Plasma heating by EGAMs

To investigate the plasma heating by EGAMs, we start from the study of the mode behaviour dependence on energetic particle (EP) parameters. The physical mechanism underlying the heating process is explained below, see discussion relative to

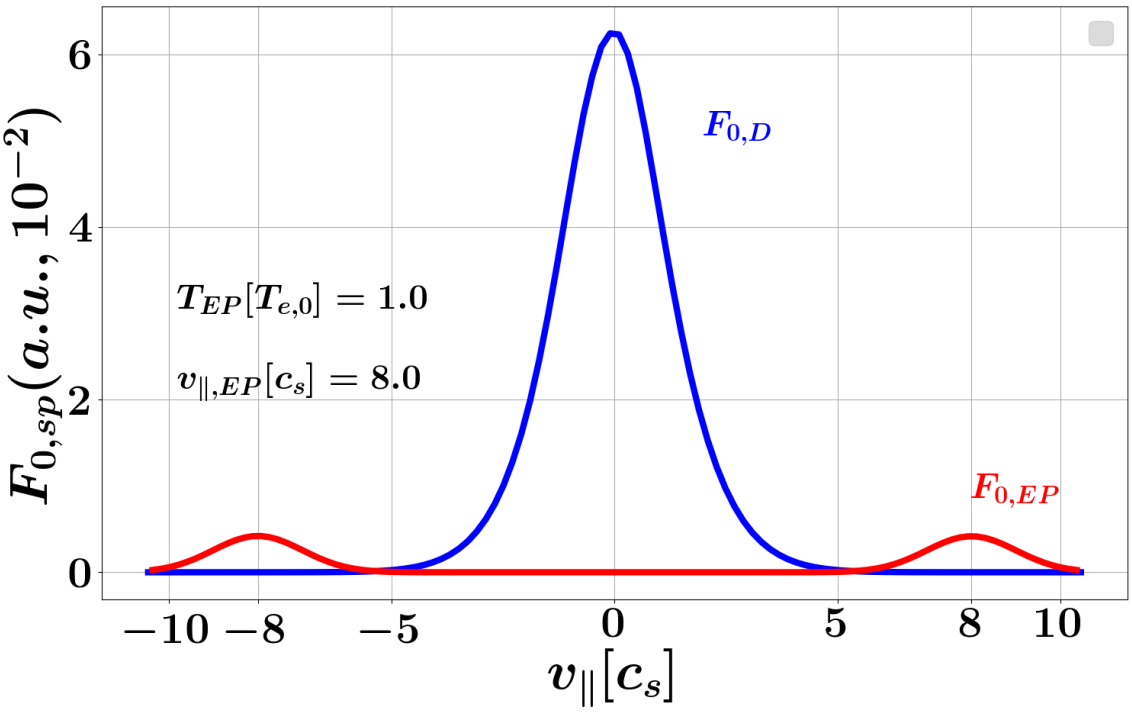

Figure 7.2: Equilibrium distribution functions of the thermal ($F_{0,D}$) and energetic ($F_{0,EP}$) ions in velocity space. Here, the EP temperature is normalised to the electron temperature at a reference radial point $T_{0,e} = T_e(s = 0) = 0.70$ keV. The EP parallel velocity is normalised to $c_s = \sqrt{T_{e,max}/m_d}$, where $T_{e,max} = 1.15$ keV. *Reprinted with permission from [92], with permission from AIP Publishing.*

Fig. 7.4. Under "energetic particles" we understand here, as it is in Chapter 6, a deuterium beam, which actually drives EGAMs in a plasma system. In the simulations this species is characterised by a two-bumps-on-tail distribution function in velocity space, while thermal species (deuterium or electrons) have a Maxwellian distribution function (Fig. 7.2). It should be remarked that in the experimental shot, the EGAM is driven mostly by an EP slowing-down distribution function with a pitch-angle dependence [104]. However, here the EPs are modelled by means of the two shifted Maxwellians to qualitatively investigate the EGAM behaviour in the AUG plasma configuration. From Fig. 6.1 one can see that the EPs have relatively low temperature. This just indicates the fact that the width of the EP bumps is smaller in comparison to that of the thermal ion Maxwellian. A typical shift of the EP bumps in the parallel velocity is $v_{\parallel,EP}[c_s] = 8.0$, while typical EP temperature is $T_{EP}[T_e(s=0)] = 1.0$ or $T_{EP}[keV] = 0.70$. Here, $c_s = \sqrt{T_{e,max}/m_d}$ is the sound speed with m_d being the deuterium mass, $T_{e,max} = 1.15\ keV$. Such kind of the normalisation for $v_{\parallel,EP}$ and T_{EP} is used throughout this chapter, and it is the same as in Sec. 6.2.

In this section, for the investigation of the plasma heating by EGAMs, the EPs are described in space by an axisymmetric Gaussian distribution function:

$$F_{0,EP}(s) \sim \exp\left(\frac{-(s-s_{EP})^2}{2\sigma_{EP}^2}\right), \tag{7.1}$$

with localisation at a radial point $s_{EP} = 0.50$. Such a simplification is done to have more freedom in the variation of the EP parameters. The radial width of the EP Gaussian used here is $\sigma_{EP} = 0.10$. The typical EP concentration is $n_{EP}/n_e \approx 0.01$, where n_{EP}, n_e are the EP and thermal electron densities averaged in volume, respectively.

First of all, the EGAM linear growth rate is strongly modified by EP temperature variations, as one can see in Fig. 7.3b, while the EGAM frequency remains practically the same and does not depend on T_{EP}. As it was already shown in different works [105, 38], the EPs can excite an EGAM corresponding to a damped geodesic mode in the absence of the EPs. By reducing the EP parallel velocity by a factor around of two, an EGAM with half the frequency of the original is excited (compare blue points and green crosses in Fig. 7.3a). This EGAM is driven by a higher-order GAM-EP resonance ($m > 1$ in Eq. 5.5). It should be noted here that since the mode excited by a smaller EP velocity is less unstable, it was necessary to increase the EP concentration from $n_{EP}/n_e \approx 0.01$ to $n_{EP}/n_e \approx 0.09$.

In Fig. 7.4a, one can see that by injecting an EP beam with $v_{\parallel,EP} = 8.0$ (blue dashed line), one obtains an EGAM driven by the low order resonance $m = 1$ (blue

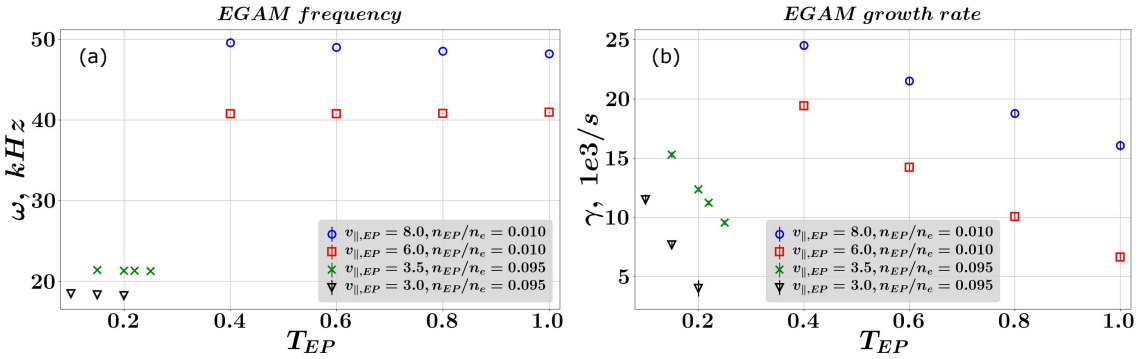

Figure 7.3: Dependence of the EGAM frequency (Fig. 7.3a) and linear growth rate (Fig. 7.3b) on the temperature and velocity shift of the EP beam. *Reprinted with permission from [92], with permission from AIP Publishing.*

solid line). On the other hand, injection of an EP beam with $v_{\parallel,EP} = 3.5$ (red dashed line) leads to the EGAM drive on the $m = 2$ resonance (red solid line). The time evolution of the zonal electric field in these two cases with low and high EP velocities is shown in Fig. 7.5. The high velocity energetic beam (Fig. 7.5b) drives an EGAM through a low order $m = 1$ resonance, and the resulting mode has a frequency close to the original GAM frequency. The low velocity energetic beam (Fig. 7.5a), which interacts with the geodesic mode through a high order $m = 2$ resonance, drives an EGAM with a frequency close to half the GAM frequency. Indeed, according to Fig. 7.4, the mode-species resonances are localised at

$$v_{\parallel,res,num}^{m=1} \approx 6.5, \quad v_{\parallel,res,num}^{m=2} \approx 2.7. \tag{7.2}$$

The GAM frequency can be computed from a simulation without EPs:

$$\omega_{gam}(s = 0.50) = 49\ kHz, \tag{7.3}$$

to compare with corresponding EGAM frequencies

$$\omega_{egam}^{EP8.0}(s = 0.50) = 40\ kHz, \quad \omega_{egam}^{EP3.5}(s = 0.50) = 21\ kHz \tag{7.4}$$

Using these frequencies and a safety factor value $q(s = 0.50) = 2.3$, (E)GAM-plasma resonance positions can be analytically estimated from Eq. 5.5:

$$v_{\parallel,res,theor}^{EP8.0} = qR_0\omega_{egam}^{EP8.0} \approx 5.2, \quad v_{\parallel,res,theor}^{EP3.5} = qR_0\omega_{egam}^{EP3.5} \approx 2.8, \tag{7.5}$$

$$v_{\parallel,res,theor}^{gam,m=1} \approx 6.4, \quad v_{\parallel,res,theor}^{gam,m=2} \approx 3.2. \tag{7.6}$$

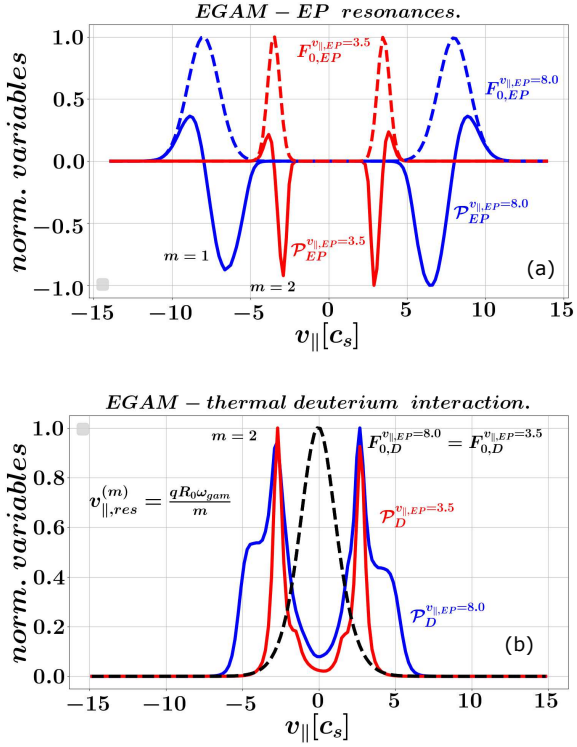

Figure 7.4: Localisation of the EGAM interaction with the EPs (Fig. 7.4a) and with thermal deuterium (Fig. 7.4b). Here, two simulations are considered: with $v_{\|,EP} = 8.0, T_{EP} = 1.0$ (blue lines), and with $v_{\|,EP} = 3.5, T_{EP} = 0.25$ (red ones). The solid lines indicate the mode-species energy transfer $\mathcal{P}_{sp}$ (Eq. 5.2), integrated on the perpendicular velocity and averaged on several EGAM periods in time. The dashed lines depict the localisation of the species initial distribution functions. *Reprinted with permission from [92], with permission from AIP Publishing.*

The difference between $v_{\|,res,theor}^{EP8.0}$ and $v_{\|,res,num}^{m=1}$ might be explained by the fact that $v_{\|,res,num}^{m=1}$ is estimated from the signal averaged in a whole space domain while $v_{\|,res,theor}^{EP8.0}$ is calculated by using local plasma parameters. Moreover, the first order resonance $v_{\|,res,num}^{m=1}$ has a significant width along parallel velocity. Since the $m = 1$ and $m = 2$ GAM resonance velocities are close to $v_{\|,res,num}^{m=1}$ and $v_{\|,res,num}^{m=2}$ respectively, it is reasonable to consider the EGAM as a mode that is driven by the first order resonance in case with $v_{\|,EP} = 8.0$, and by the second order resonance in case with $v_{\|,EP} = 3.5$.

As it was mentioned in [102, 95], the interactions between the EPs and thermal

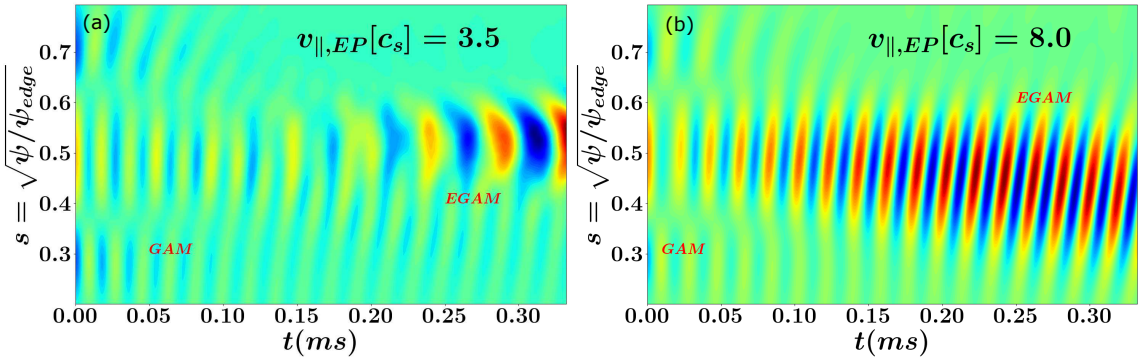

Figure 7.5: Time evolution of zonal electric field $\overline{E}$ in two cases with low (Fig. 7.5a) and high (Fig. 7.5b) EP velocities. *Reprinted with permission from [92], with permission from AIP Publishing.*

species significantly benefit from the existence of high order resonances, which is confirmed here as well. The EGAM-thermal ion energy exchange occurs at the higher order ($m = 2$) resonance in both cases, independently of the EP parallel velocity (Fig. 7.4b). In other words, even when the EGAM is driven by an EP beam with a high parallel speed, the EGAM is still damped by the thermal deuterium through resonances of higher order ($m = 2$). This can be simply explained by the fact that the position of these resonances are closer to the bulk of the thermal ion distribution function. Since the thermal ion energy transfer signal (Fig. 7.4b) is positive, and the EP energy transfer signal (Fig. 7.4a) is mostly negative, there is an energy flow from the EPs to the thermal ions establishing bulk plasma heating, where the EGAM plays a role of an intermediate agent. As a result, the thermal species can obtain energy from the EGAM due to the Landau damping of the mode, which in its turn is driven by the energetic particles through the inverse Landau damping. Note that this is also true for Alfvén modes, with the substantial difference that the EP radial redistribution by EGAMs is negligible with respect to that by Alfvén modes. Therefore, EGAMs represent a privileged mode for this plasma heating mechanism.

Now, by varying EP parameters, we are going to investigate the energy exchange between energetic/thermal species and the EGAM in the AUG plasma configuration by performing nonlinear GK simulations firstly in the ES limit with adiabatic electrons. In these simulations, we are dealing with gyrokinetic thermal deuterium, gyrokinetic energetic deuterium (EP), and adiabatic electrons (AE). Plasma parameters and magnetic configuration are taken the same as in Sec. 6.1. Real space is

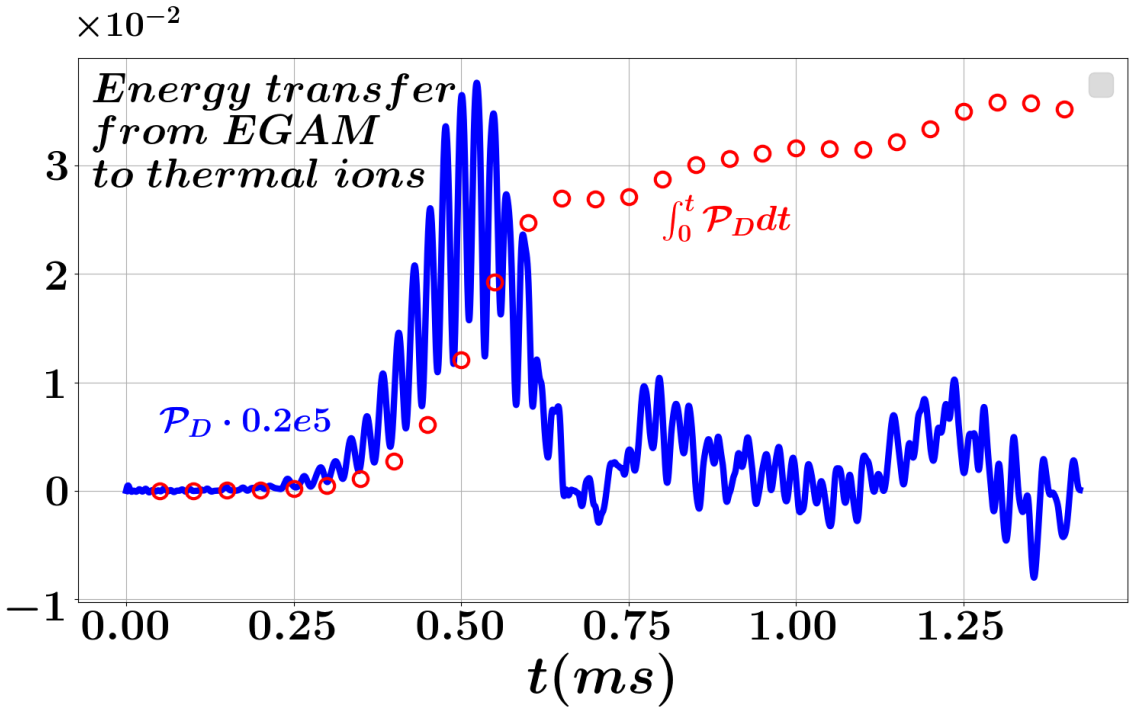

Figure 7.6: Time evolution of the heating rate (solid blue line), and the amount of energy transferred from the EGAM to the bulk deuterium plasma (red points). A case with $n_{EP}/n_e = 0.09, v_{\parallel,EP} = 3.5, T_{EP} = 0.25$ is considered here. The heating rate $\mathcal{P}_D$ is normalised according to Eq. 5.3. *Reprinted with permission from [92], with permission from AIP Publishing.*

discretized using the following grid parameters: $n_s = 128, n_\chi = 64, n_\phi = 32$, - for the radial, poloidal and toroidal directions respectively. Only $n = 0$ toroidal and $|m| = [0, .., 3]$ poloidal mode numbers are taken into account, since generally the geodesic acoustic modes have mainly low m numbers. The ES cases are simulated in a radial domain $s = [0.0, 0.95]$ with a time step $dt[\omega_{ci}^{-1}] = 20$. The number of numerical markers for the thermal deuterium (N_d) and for the EPs (N_{EP}) in these cases are $N_d = N_{EP} = 6 \cdot 10^7$.

To calculate the amount of energy transferred from the mode to the thermal ions, the EGAM-species energy exchange signal $\mathcal{P}_{sp}$ is integrated in time. As it is shown in Fig. 7.6, at the beginning, a rise of the heating rate due to the growth of the mode is observed. After a while, the mode saturates[1], the heating rate level decreases,

[1]One of the main mechanisms of the mode saturation is the flattening of the EP distribution

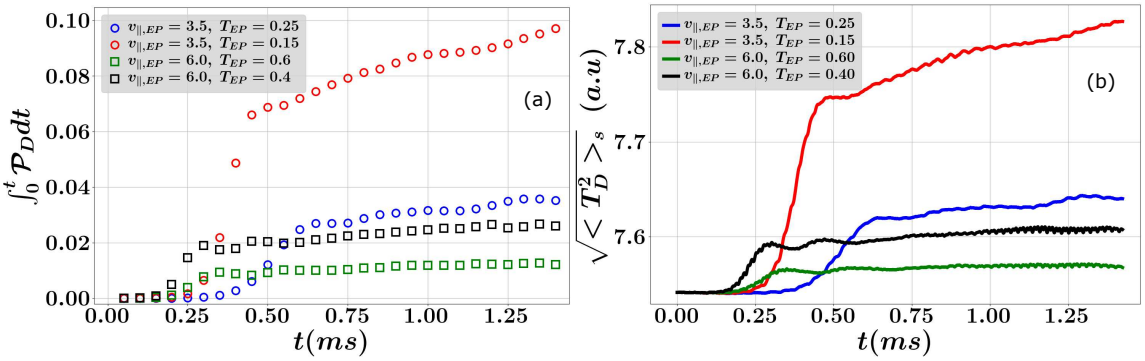

Figure 7.7: Energy transferred from the EGAM to the bulk ions for different EP temperatures and parallel velocities (Fig. 7.7a). Evolution of the thermal ion temperature in the same cases (Fig. 7.7b). *Reprinted with permission from [92], with permission from AIP Publishing.*

and in the deep saturated domain the energy transfer from the mode to the thermal ions is practically suppressed. This means that the total energy transferred to the bulk plasma (red points in Fig. 7.6) remains practically unchanged after the mode saturation. The amount of this energy depends on the EP parameters (Fig. 7.7a), which is directly reflected in the bulk ion temperature evolution (Fig. 7.7b).

By varying the EP parameters in NL electrostatic simulations, one can observe a general correlation between the EGAM saturation levels and the amount of energy transferred from the mode to the bulk deuterium plasma (Fig. 7.8). However, for example, the case with $v_{\parallel,EP} = 6.0,\ T_{EP} = 0.4,\ n_{EP}/n_e = 0.01$ (the rightmost red star) has practically the same saturation level as the case with $v_{\parallel,EP} = 3.5,\ T_{EP} = 0.15,\ n_{EP}/n_e = 0.09$ (the rightmost blue point), but the corresponding EGAM-bulk ion energy exchange for these cases is significantly different. This means that having the same mode level, one can achieve higher plasma heating by varying EP parameters. Here, in particular, the increase of the EP density n_{EP}/n_e and lowering of the EP temperature T_{EP} has led to a high energy transfer from the EPs to the mode. On the other hand, according to the simulations, the decrease of the EP velocity has made the mode transfer a higher part of its energy to the thermal plasma enhancing in such a way the energy exchange between energetic and thermal ions, and keeping the EGAM amplitude on the same level.

As we have already seen in Sec. 6.2, inclusion of the electron dynamics might

function (see Appendix B in [92] for more details).

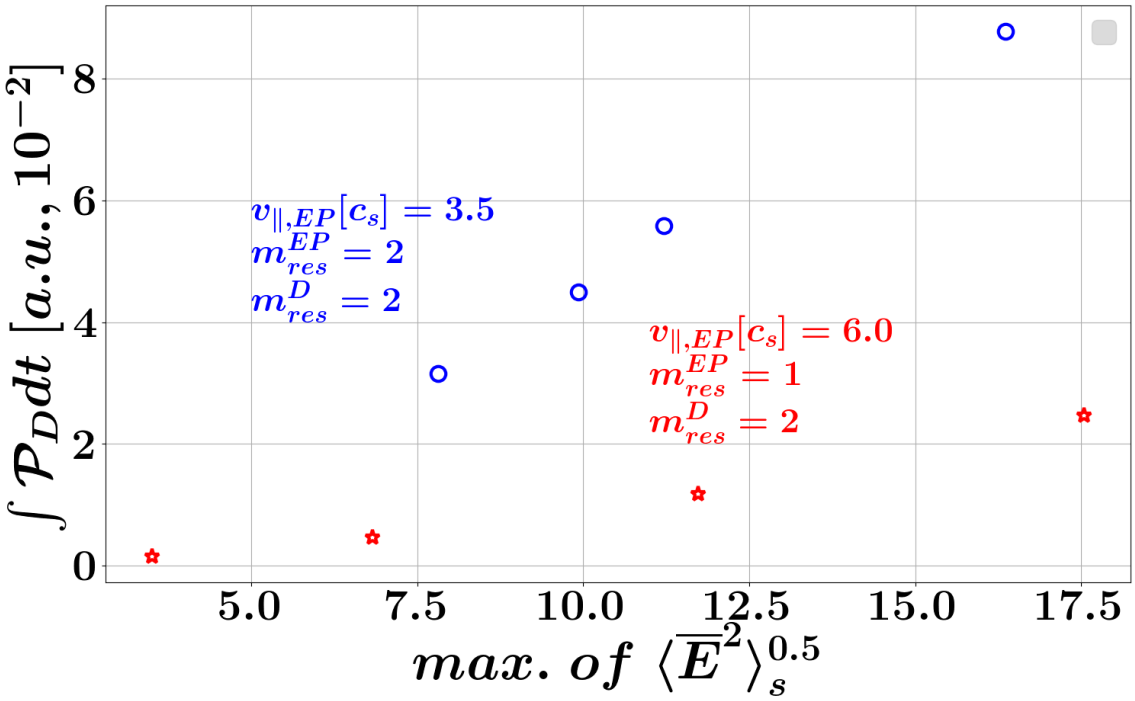

Figure 7.8: Dependence of the EGAM-thermal deuterium energy exchange on the EGAM saturation level in nonlinear ES simulations with adiabatic electrons. The saturation levels are calculated as a maximum value in time of r.m.s in space of the zonal electric field $\overline{E}$. The electric field is normalised to $T_e(s = 0.0)[eV]\omega_{ci}[s^{-1}]/c_s[m/s]$. Here, m_{res}^{sp} indicates an order of a resonance, where the mode-species energy exchange occurs. The blue points correspond to the cases with $v_{\parallel,EP} = 3.5$, $n_{EP}/n_e = 0.09$, $T_{EP} = [0.25, 0.22, 0.20, 0.15]$, while the red stars correspond to the cases with $v_{\parallel,EP} = 6.0$, $n_{EP}/n_e = 0.01$, $T_{EP} = [1.0, 0.8, 0.6, 0.4]$. *Reprinted with permission from [92], with permission from AIP Publishing.*

significantly reduce the EGAM growth rate. Consequently, it is reasonable to suppose that inclusion of the electron dynamics influences the nonlinear EGAM behaviour as well. To check this conjecture, NL electromagnetic simulations are performed here with drift-kinetic electrons (KEs). The KEs have a realistic deuterium/electron mass ratio $m_D/m_e = 3672$. The EM cases are simulated with $n_s = 256$, $dt[\omega_{ci}^{-1}] = 5$ in a radial domain $s = [0.0, 0.90]$, taking $N_e = 1.2 \cdot 10^8$ (number of electron markers) with the same N_d and N_{EP}. The radial domain is reduced to make the EM simulations more stable by avoiding the abrupt increase of the safety factor at the edge, reducing

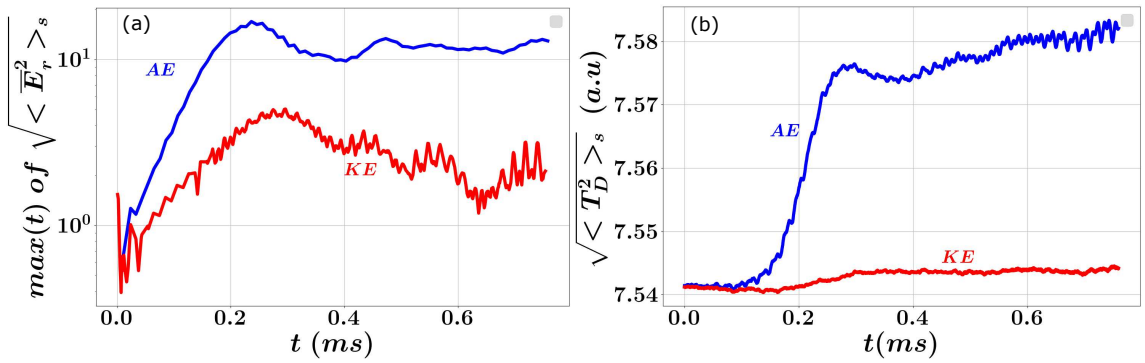

Figure 7.9: Comparison between an electrostatic NL simulation assuming adiabatic electrons (AE) and an electromagnetic NL simulation with drift-kinetic electrons (KE). In both cases $n_{EP}/n_e = 0.01, v_{\parallel,EP} = 8.0, T_{EP} = 1.0$ are taken. EGAM saturation levels (Fig. 7.9a). Evolution of the thermal deuterium temperature (Fig. 7.9b). *Reprinted with permission from [92], with permission from AIP Publishing.*

in such a way the restriction on the numerical time step. Since EGAMs are localised mainly in the core, this reduction of the radial domain has a negligible influence on the EGAM dynamics.

Consistently with the decrease of the EGAM linear growth rate, observed in Sec. 6.2, the mode saturation levels are reduced in NL simulations with KEs (Fig. 7.9a). This leads to a lowering of the plasma heating by the mode, which is clearly observed in the time evolution of the thermal ion temperature (Fig. 7.9b). However, even in the case with the drift-kinetic electrons, the EGAM transfers most of its energy to the thermal ions, and not to the electrons, that can be seen in Fig. 7.10a. In other words, the ion plasma heating remains the preferred heating channel. Having said that, we should emphasize the fact that the electron contribution is still not negligible in comparison to the total energy, obtained by the EGAM due to the wave-particle interaction with all kinetic species in the considered plasma system. More precisely, in Fig. 7.10b, one can see that the amount of energy that the mode stores in the ES simulation (blue line) and the energy that the mode transfers to the electrons in KE simulations (red line) in the EM simulation are of the same order. Negative blue line indicates the fact that the EGAM interaction with the EPs and the thermal ions result in the increase of the mode energy. The red curve is positive because the energy flows from the mode to the electrons. Although this flow is significantly smaller than that to the thermal ions, it is still comparable to the total mode energy. A similar behaviour has been identified in linear EGAM simulations in Sec. 6.2. Therefore, the

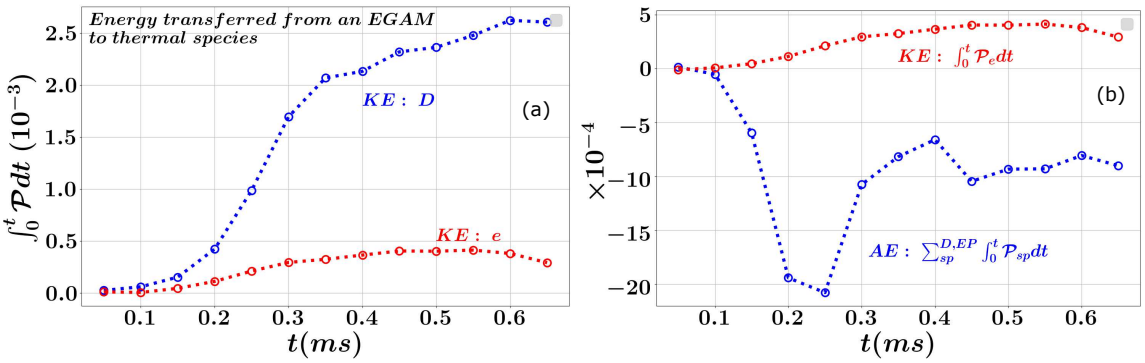

Figure 7.10: Nonlinear ES and EM cases with $n_{EP}/n_e = 0.01, v_{\parallel,EP} = 8.0, T_{EP} = 1.0$ are considered. Energy transferred from the mode to the thermal species (Fig. 7.10a, blue line - thermal ions, red line - electrons) in the nonlinear EM case with drift-kinetic electrons. Total energy balance between the EGAM and all kinetic species in the ES case (Fig. 7.10b, blue line), and the electron contribution in the EM simulation (red line). *Reprinted with permission from [92], with permission from AIP Publishing.*

electron dynamics can noticeably decrease the amount of energy stored in the mode, reducing its saturation level and in such a way lowering the plasma heating by the EGAM.

7.2 EGAM frequency chirping

To model the nonlinear evolution of the EGAM frequency, the EP parameters are taken consistently with previous works [88, 58]) and Sec. 6.1, where the mode frequency has been approximately reproduced in linear GK simulations in the same AUG discharge. The following EP velocity $v_{\parallel,EP} = 8.0$, temperature $T_{EP} = 1.0$ and concentration $n_{EP}/n_e = 0.095$ are applied. In Fig. 7.11a, one can see a zoom of the 'long' branch, described previously, of the experimental EGAM up-chirping. In Fig. 7.11b, experimental and numerical spectrograms normalised to initial EGAM frequencies are indicated. The blue curve shows the mode up-chirping obtained from a nonlinear ES simulation with adiabatic electrons. The numerical spectrogram is measured by nonlinear fitting of zonal electric field in different time windows at the radial point of the mode localisation $s = 0.70$ (Fig. 7.11c). The red curve corresponds to the experimental EGAM spectrogram, but with a squeezed time scale,

since the characteristic time of the numerical frequency change is shorter than the experimental one.

As one can see from Fig. 7.11b, the GK model is able to qualitatively reproduce the EGAM relative up-chirping in this AUG discharge. On the other hand, to perform a quantitative comparison with the experiment, one should use an EP

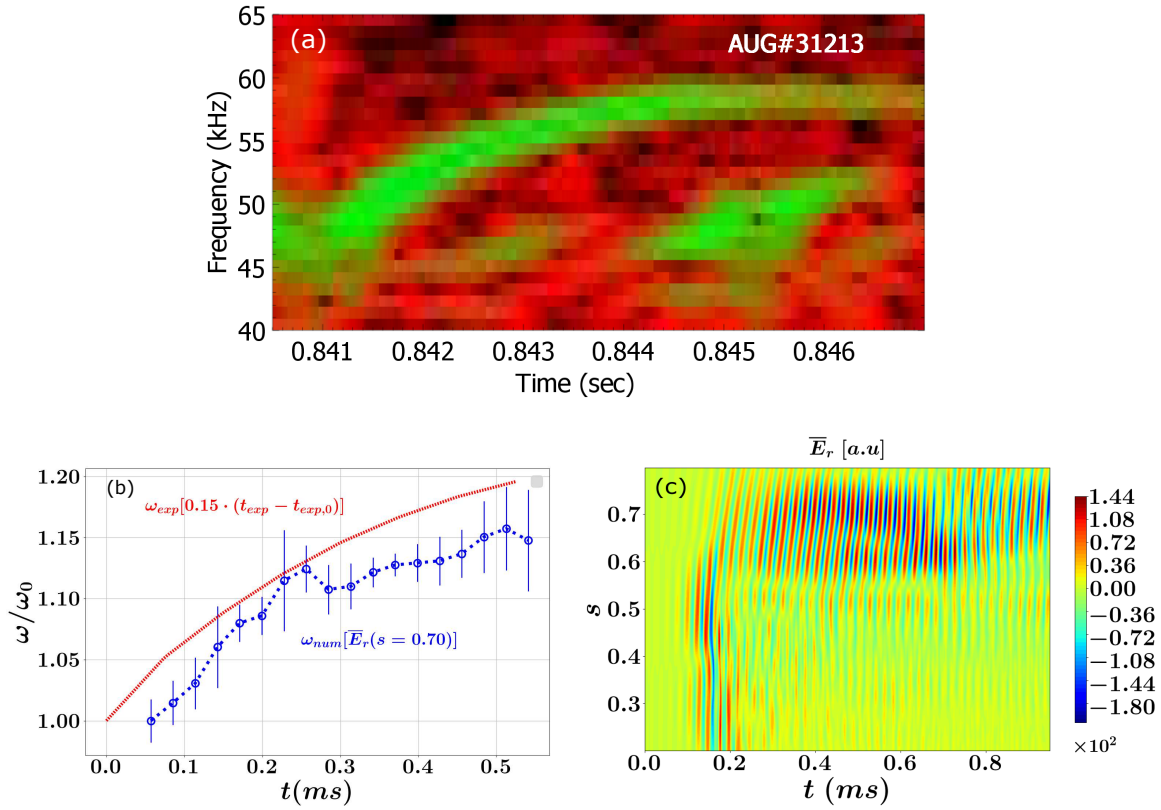

Figure 7.11: A zoom of a 'long' branch of the EGAM up-chirping from the experimental AUG spectrogram [87] is shown in Fig. 7.11a. Numerical and experimental EGAM spectrograms normalised to initial EGAM frequencies ($\sim 39\ kHz$ and $\sim 47\ kHz$ respectively) are indicated in Fig. 7.11b. The numerical chirping is calculated by nonlinear fitting of zonal electric field $\overline{E}$ at a radial point of the EGAM localisation. Time evolution of the zonal electric field: the EGAM is localised around a radial point $s \approx 0.7$ (Fig. 7.11c). *Reprinted with permission from [92], with permission from AIP Publishing.*

distribution function closer to the experimental one such as a slow-down distribution function with a pitch-angle dependence, since the EGAM is a strongly driven mode, and it significantly depends on EP parameters. Moreover, the considered simulation is performed electrostatically without taking into account the dynamics of the drift-kinetic electrons. As it has been shown previously, electrons can significantly modify the EGAM behaviour and, as a result, might have some effect on the mode chirping as well.

7.3 Some remarks on EGAMs in ITER

It should be noted that the EGAM existence in ITER, especially, in the standard scenarios, where the safety factor profile $q \sim 1$, is highly doubtful. To briefly investigate this question, we start from the consideration of the main ($m = 1$) GAM-EP resonance condition (Eq. 5.5):

$$v_{EP} = \omega_{GAM} q R_0, \tag{7.7}$$

where q is the safety factor, $R_0[m]$ is the major radius of the magnetic axis, ω_{GAM} is the GAM frequency, and v_{EP} is the EP speed. We can estimate the mode frequency as

$$\omega_{GAM} \sim \frac{v_{th,i}}{R_0}, \; v_{th,i} = \sqrt{\frac{T_{th,i}}{m_{th,i}}}, \tag{7.8}$$

where $v_{th,i}$ is the speed of thermal ions (deuterium or tritium) with a temperature $T_{th,i}$ and mass $m_{th,i}$. As a result, to have a resonance between the zonal mode and the energetic particles, the following equation must be satisfied:

$$\mathcal{E}_{EP} \sim \frac{m_{EP}}{2 m_{th,i}} T_{th,i} q^2, \tag{7.9}$$

where m_{EP} is an EP mass. According to [106], currently the neutral beam heating system in ITER is designed to deliver $\mathcal{E}_{EP} = 1\ MeV$ of deuterium or $0.87\ MeV$ of protium, which leads to $m_{EP}/m_{th,i} \leq 1$. Other relevant ITER plasma parameters are $T_{th,i} \sim 10\ keV$, $q^2 \sim 1 - 10$. In the case with a deuterium beam injected into bulk deuterium plasma with an elevated safety factor profile, we have that

$$\mathcal{E}_{EP} \sim 1\ MeV, \tag{7.10}$$

$$\mathcal{E}_{res} = \frac{m_{EP}}{2 m_{th,i}} T_{th,i} q^2 \sim 50\ keV. \tag{7.11}$$

One can see that the energy of the injected EP beam is far away from the resonance with the GAMs. To count on any EGAM drive by the EPs, the EP distribution function should be significantly relaxed to achieve the resonance with the mode. Because of the significant distance between the injected EP energy and the GAM resonance, the resulting slow-down distribution function might have such a weak slope in the velocity region of the mode resonance that the resulting EGAM drive might be insufficient to overcome the mode damping. We should also note that the EGAMs might be much weaker than other EP driven modes such as the Alfvén modes.

One of the main EGAM advantages is that they provide a way to transfer energy from the EPs directly to the thermal ions, while through the collisional processes the EPs with a temperature higher than some critical one heat mainly electrons. Having said that, we should mention again that in ITER the EPs have to be significantly slowed down to drive the geodesic modes. Using [107], we can estimate the critical EP energy where the energetic particles transfer equal parts of their energy to the thermal electrons and ions through collisions:

$$\mathcal{E}_{crit}[keV] = 14.8 \cdot T_e[keV] \cdot A_{EP} \left(\frac{1}{n_e} \frac{n_{th,i} Z_{th,i}^2}{A_{th,i}} \right)^{2/3}, \tag{7.12}$$

where T_e, n_e are thermal electron temperature and density, $A_{EP}, A_{th,i}$ are the atomic weights of the injected EPs and of the thermal ions respectively, and $Z_{th,i}$ is the charge number of the thermal ions. Above the critical energy, the EP-plasma collisions transfer energy from EPs mainly to thermal electrons while the EPs with an energy lower than the critical one exchange their energy through collisions mainly with thermal ions. By considering a case with energetic and thermal deuterium, one can estimate a value of the critical EP energy:

$$\mathcal{E}_{crit}[keV] \sim 185, \tag{7.13}$$

where we have assumed that $n_{th,i}[cm^{-3}] = 0.99 \cdot n_e[cm^{-3}]$ (this means energetic particles constitute 1% of all ions in the plasma system), $n_e[cm^{-3}] = 10^{14}$, $T_e[keV] = T_{th,i}[keV] = 10$. We note that an increase of the EP concentration leads to a slight decrease of the critical energy (due to the drop of the thermal ion density). From Eq. 7.11 and Eq. 7.13, it is evident that EGAMs are driven by EPs with a significantly lower energy than the critical one. The characteristic time scale of the collisional energy transfer (or, in other words, time scale of the EP thermalization) can be estimated using again [107]:

$$\tau_{coll}[s] = 2.09 \cdot 10^8 \frac{A_{EP} T_e[eV]^{3/2}}{Z_{EP}^2 n_e[cm^{-3}] \ln \Lambda} \ln \left(1 + \left(\frac{\mathcal{E}_{EP}}{\mathcal{E}_{crit}} \right)^{3/2} \right), \tag{7.14}$$

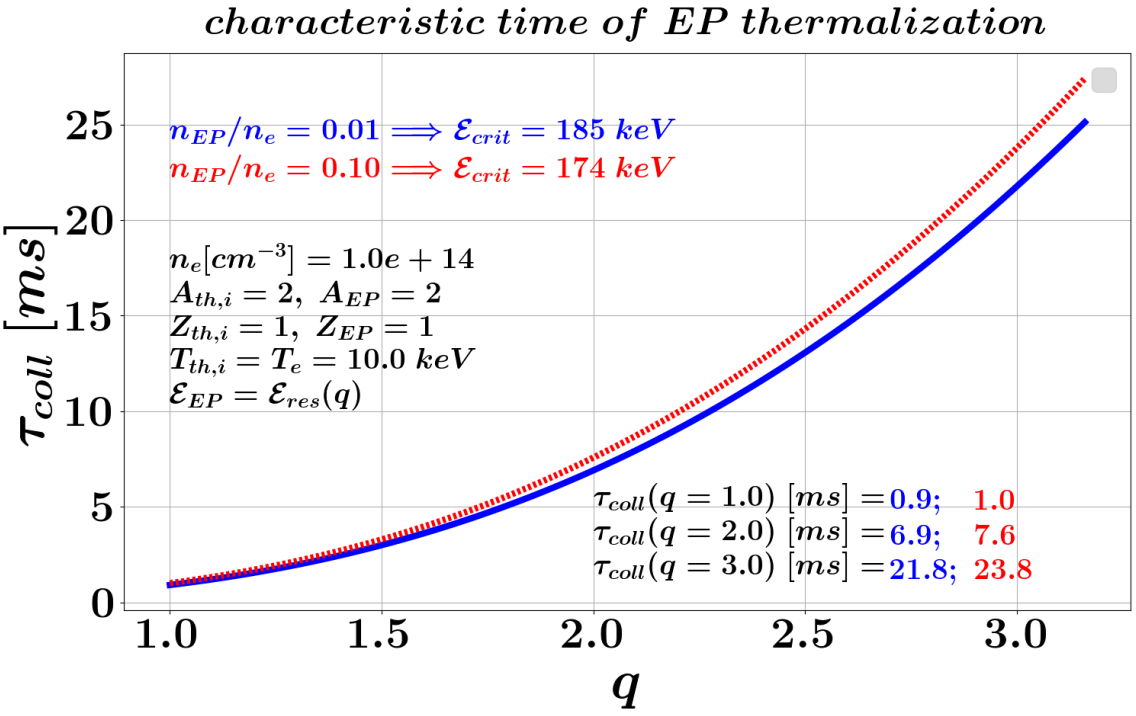

Figure 7.12: Dependence of the collisional characteristic time scale on the safety factor value for different EP concentrations.

where for the Coulomb logarithm we are going to use an expression for mixed ion-ion collisions, taken from [78]:

$$\ln\Lambda \;=\; 23 - \ln\left(\frac{Z_{th,i}Z_{EP}(A_{th,i}+A_{EP})}{A_{th,i}T_{EP}+A_{EP}T_{th,i}}\left(\frac{n_{th,i}Z_{th,i}^2}{T_{th,i}}+\frac{n_{EP}Z_{EP}^2}{T_{EP}}\right)^{1/2}\right). \quad (7.15)$$

Here, all temperatures are taken again in eV, while densities are in cm^{-3}, and we assume that $T_{EP} = \mathcal{E}_{EP}$. For the chosen parameters of the thermal and energetic species, the value of the Coulomb logarithm is around 21. Taking the EP energy $\mathcal{E}_{EP}$ in Eq. 7.14 equal to the resonance energy $\mathcal{E}_{res}(q)$ (Eq. 7.11) as a function of q, one can find the dependence of the EP thermalization time scale on the safety factor (Fig. 7.12). In a scenario with an elevated safety factor $q \sim 2$, the collisional time scale is around $7\ ms$. From this rough analysis follows that even if EGAM was excited in ITER, the process of the thermal ion heating by the geodesic mode would compete with the collisional heating of the thermal ions directly by the EPs.

7.4 Chapter summary

The EGAMs provide an additional mechanism of the energy exchange between the energetic particles and the thermal plasma, enhancing direct heating of the bulk ions. The significant progress done in the last decade in studying the EGAM nonlinear physics has been expanded here, by including drift-kinetic electrons and the geometrical effects of a realistic AUG magnetic shape in the GK simulations. It has been demonstrated that the GK code can handle zonal structures, and anisotropic distribution functions properly in experimentally relevant cases, which is a crucial ingredient before going into more complex plasma systems.

By varying the EP parameters, a general correlation between the mode level and the EP-thermal plasma energy flow has been revealed. It has been emphasized that the plasma heating by EGAMs benefits from the presence of high order mode-particle resonances, which are often responsible for the EGAM-thermal species interaction. Having the same mode levels, one can achieve a higher energy exchange between energetic and thermal species through an EGAM by adjusting the EP parameters. It has been indicated as well that although the EGAM transfers most of its energy to the thermal ions, and not to the electrons, the electron dynamics might significantly reduce the plasma heating by EGAMs by lowering the mode amplitude.

Chapter 8

Nonlinear GAM excitation by turbulence

The zonal structures including the GAMs can be driven directly by drift instabilities such as Ion Temperature Gradient (ITG) modes, as it has been indicated in Sec. 1.5. The excited oscillatory zonal modes can have continuum, staircase, or even global frequency spectra. The continuum spectrum, which is predicted by linear simulations, and generally appears in nonlinear calculations, is characterized by a clear dependence of the GAM frequency on plasma temperature and safety factor profiles. However, staircase and global GAM frequency spectra [108] were observed experimentally [49, 50, 109, 110], and in nonlinear numerical simulations [52, 53] as well. If a zonal mode has such kind of spectrum, it oscillates with a frequency that remains constant within a significant radial interval disregarding the change of the plasma temperature and magnetic field radial profiles. There is not still a final theory that would describe the formation of the global GAM spectra. A possible explanation given in MHD theory is the coupling of the second poloidal harmonics $m = 2$ of zonal electric field [111, 80]. The toroidal plasma rotation might favour the GAM transition from the continuum to the global regime as it is discussed in [51]. However, no global GAM eigenmodes were found in linear gyrokinetic simulations of an AUG shot where a global GAM was experimentally observed [49]. For this reason, we have conjectured that the global (staircase) GAM formation might have a nonlinear origin [34]. This was found to be consistent with GENE nonlinear simulations, where different factors like electromagnetic effects and collisionality were studied [52].

In this Chapter, we work with two realistic magnetic configurations. In Sec. 8.1, the results presented in [53] are extended by analysing the zonal mode generation

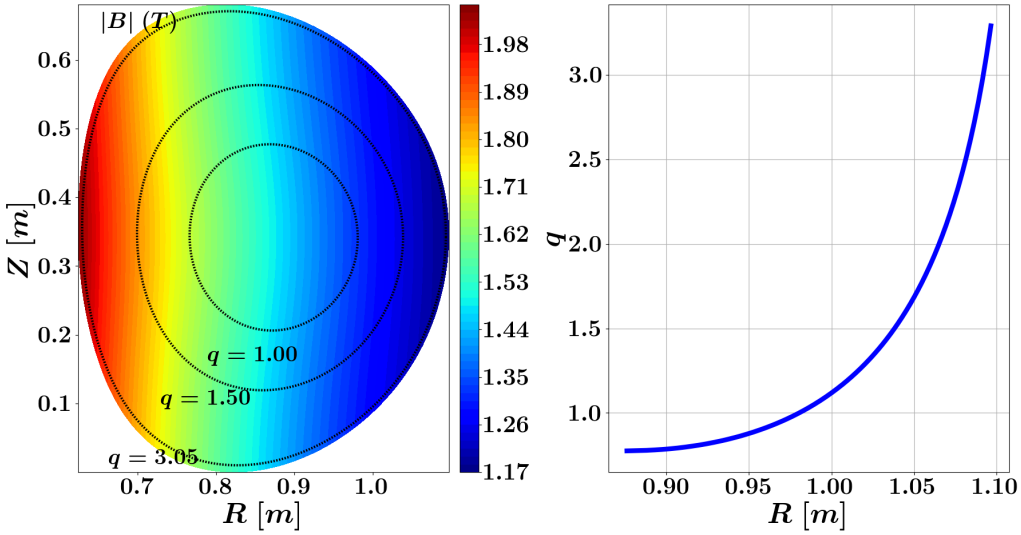

Figure 8.1: TCV magnetic configuration and safety factor profile. The indicated radial domain in meters ($R[m]$) in the right plot corresponds to the normalised radial interval $s = [0.0, 1.0]$.

by different ITG spectra in the TCV magnetic configuration. Both continuum and global spectra are observed in this modelling, and it is shown that higher toroidal mode numbers are responsible for the excitation of the global GAM-like structure in this discharge. In Sec. 8.2, nonlinear GK computation of the ASDEX Upgrade discharge #20787 is performed with the code ORB5. The resulting GAM spectrum is compared with the linear estimation of the mode frequency presented in Sec. 4.4 and with experimental data given in [49]. Consistently with the simulations of the TCV case, it is found that high toroidal n-modes are crucial for the observation of the GAM staircase spectrum. The comparison of the results obtained here for different tokamaks, serves to pave the way to a universal theoretical model of global GAMs, which is independent of the specific machine parameters.

8.1 Global frequency spectrum of a GAM-like zonal signal in TCV magnetic configuration

It was shown in [53] that the increase of the plasma temperature gradient at the very edge of a plasma system leads to the transition from a continuum GAM frequency spectrum to a mix of continuum and global GAM-like structures. In this section, we

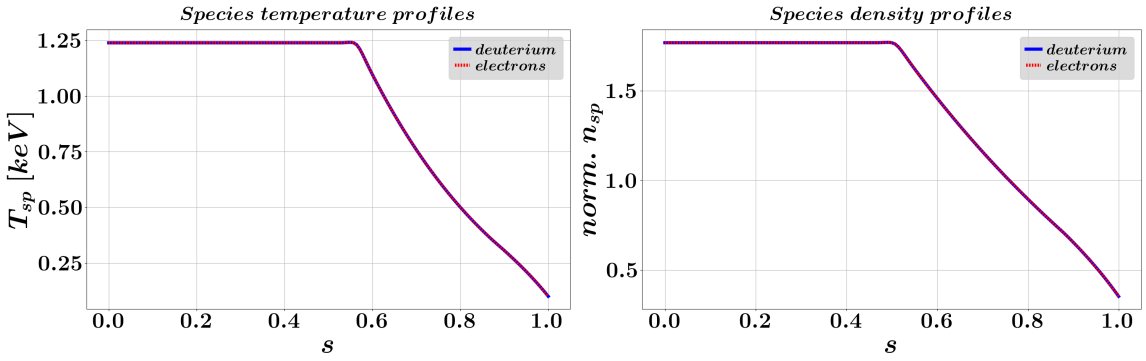

Figure 8.2: Species temperature and density profiles in the TCV case.

investigate the same TCV magnetic configuration (Fig. 8.1) with the major radius $R_0 = 0.88\ m$, the minor radius $a_0 = 0.25\ m$, and the magnetic field $B_0 = 1.44\ T$. Our final goal here is to find out what part of the ITG spectrum is responsible for the excitation of the global structures. The simulations are performed electrostatically with adiabatic electrons (see footnotes in Sec. 1.3). The species density and temperature profiles (Fig. 8.2) are taken from [53]. They are analytically created for a qualitative investigation of the global zonal structures. The reference radial point is $s_0 = 0.88$, where the temperature is $T_e(s_0) = 0.343\ keV$ that corresponds to the sound frequency $\omega_s = 145.6 \cdot 10^3\ rad/s = 23.2\ kHz$. The sound frequency $\omega_s = c_s(s_0)/R_0$ is used here for the ITG/GAM frequency, ITG growth rate, and time normalisation[1].

First of all, we should estimate the number of ITG modes that should be included in our nonlinear simulations. The ITG linear spectrum is taken from linear GK computation. According to Fig. 8.3, the most unstable linear ITG mode is that with a toroidal number n around 85. It corresponds to the poloidal wavenumber $k_\chi \rho_i \approx 1.72$ and the toroidal wavenumber $k_\phi \rho_i \approx 0.13$ estimated from[2]

$$k_\phi \approx \frac{n}{q(s_0)R_0}, \quad k_\chi \approx \frac{nq(s_0)}{a_0}. \tag{8.1}$$

To study how different ITG instabilities excite the zonal structures, we launch

[1] $\omega[Hz] = \omega[\omega_s] \cdot \omega_s[rad/s]/2\pi$, $\gamma[1/s] = \gamma[\omega_s] \cdot \omega_s[rad/s]$.

[2] The first equation in 8.1 is obtained by assuming that the so-called *connection length* measured along a magnetic field line to complete one poloidal turn is $L_{con} = 2\pi q R_0$. Therefore, the parallel wavelength of a mode with a toroidal number n, which is equivalent to the number of toroidal oscillations, is $\lambda_\phi = L_{con}/n$. The second equation assumes that the most unstable poloidal mode is $m = qn$, and the poloidal wavelength is estimated as $\lambda_\chi = 2\pi a_0/m$.

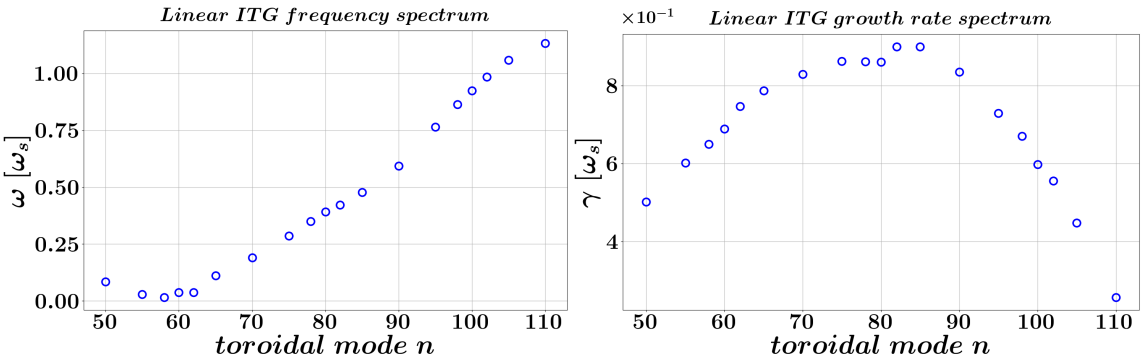

Figure 8.3: TCV case: linear ITG frequency and growth rate spectra. The values are normalised to the sound frequency $\omega_s = c_s(s_0)/R_0$.

several NL simulations with different ITG spectra. The simulations have respectively

$$n = [0, 40],\ m = [-137, 137],\ n_\phi = 160,\ n_\chi = 320,\ N_d = 3 \cdot 10^8, \tag{8.2}$$
$$n = [0, 60],\ m = [-198, 198],\ n_\phi = 240,\ n_\chi = 480,\ N_d = 6 \cdot 10^8, \tag{8.3}$$
$$n = [0, 80],\ m = [-270, 270],\ n_\phi = 320,\ n_\chi = 640,\ N_d = 6 \cdot 10^8, \tag{8.4}$$
$$n = [0, 128],\ m = [-428, 428],\ n_\phi = 528,\ n_\chi = 1056,\ N_d = 8 \cdot 10^8, \tag{8.5}$$

where m is the poloidal number, n_ϕ is the number of grid points in the toroidal direction, n_χ is the number of the poloidal grid points, N_d is the number of the deuterium markers. More precisely, in the case with $n = [0, 80]$ we keep all toroidal mode numbers from $n = 0$ (zonal structures) up to $n = 80$. The poloidal modes m are set in such a manner to guarantee that all modes $m(s) = nq(s) \pm \Delta m$ are included, where $\Delta m = 5$ is taken, and the safety factor profile $q(s)$ is shown in Fig. 8.1. This kind of Fourier filtering is justified because of the field alligned nature of the ITG instability. One can see that the maximum value of the safety factor is observed at the edge ($\max(q) \sim 3.3$). That is why $\max(|m|) = \max(n) \cdot \max(q) + 5 \approx 270$. The space resolution in the poloidal and toroidal directions should be adjusted according to the number of the toroidal n and poloidal m modes[3]. In all the cases, we model the $s = [0.0, 1.0]$ radial domain with $n_s = 256$. The choice of a field-aligned filtering has an influence on the choice of the radial resolution via the radial variation of the

[3]The code ORB5 uses OpenMP and MPI libraries for prarallelization. The MPI parallelization is based on the so-called domain/clone decomposition. Without presenting in detail the ORB5 parallelization and discretization, which is described, for example, in Sec. 3.1.5 in [112], we indicate the following rules that have to be satisfied: $n_\phi \geq 4 \cdot \max(n)$ (and $n_\phi \geq 4$ for $\max(n) = 0$),

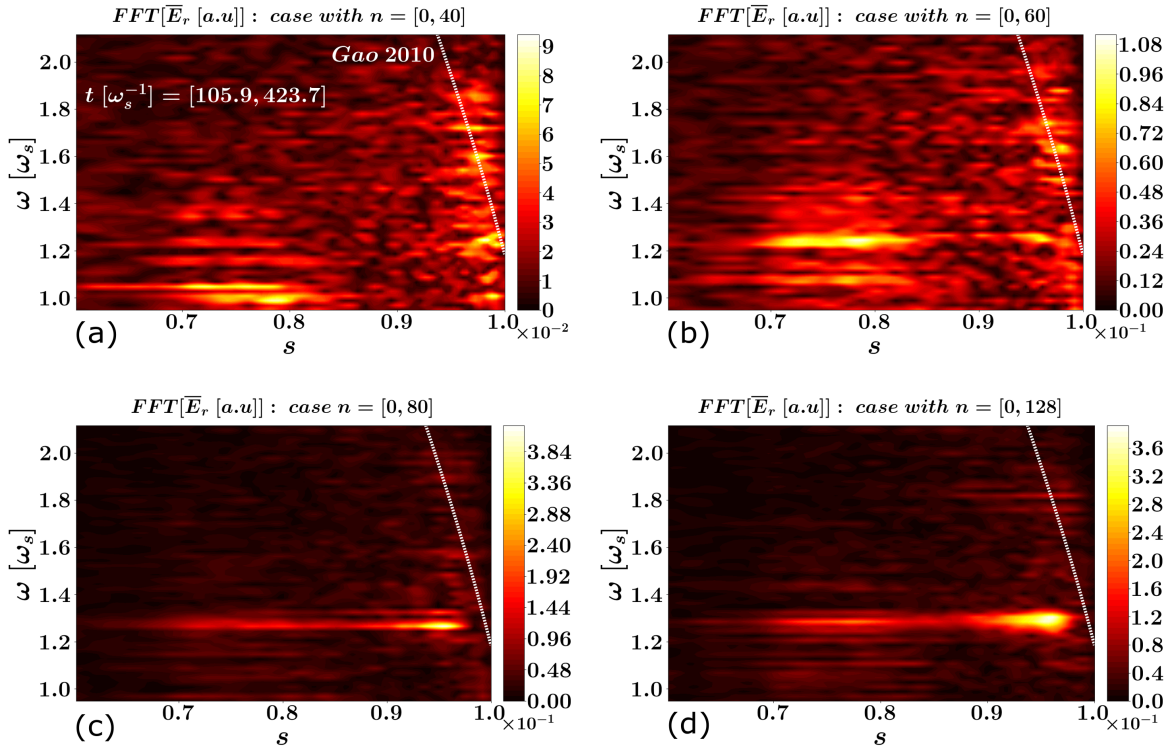

Figure 8.4: Nonlinear simulations of the TCV magnetic configuration. Frequency spectra of the zonal electric field in simulations with different ITG spectra: $n = [0, 40]$ (Fig. 8.4a), $n = [0, 60]$ (Fig. 8.4b), $n = [0, 80]$ (Fig. 8.4c), $n = [0, 128]$ (Fig. 8.4d). The white dotted lines indicate the linear estimation of the GAM frequency from the analytical theory of Gao [30]. The Fourier transformation is performed in the same time interval $t[\omega_s^{-1}] = [105.9, 423.7]$ in all the cases. Note the scale (amplitudes of the Fourier components) in the plots by comparing, for example, Fig. 8.4a and Fig. 8.4c.

$n_\chi \geq 2 \cdot \max(m)$, $\mod(n_\chi, n_\phi) = 0$, $\mod(n_\phi, n_{cpu}) = 0$, and

$$\mod\left(n_{nodes}, \frac{n_\phi \cdot n_{clones}}{n_{cpu}}\right) = 0. \tag{8.6}$$

To speed up Fast Fourier Transform, it is better to set n_ϕ as a power of 2. Here, n_{nodes} is the number of nodes (cores), where every node has n_{cpu} processes (CPU). The system is replicated into n_{clones} clones, and every clone is split in $n_{nodes} \cdot n_{cpu}/n_{clones}$ subdomains in the toroidal direction such that every subdomain has to include, at least, one toroidal point. Note that if the conditions described in Eq. 8.6 and the above text are satisfied, the code sets necessary n_{clones} automatically.

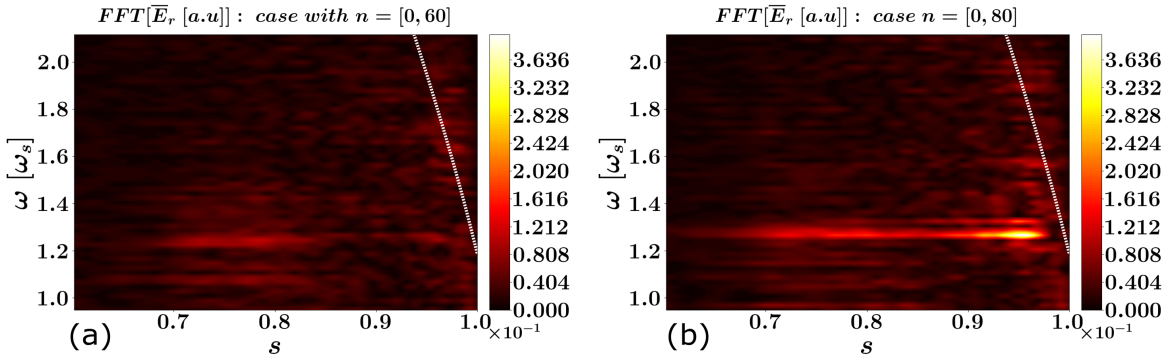

Figure 8.5: GAM frequency spectrum in the case with $n = [0, 60]$ and $n = [0, 80]$ in the same amplitude scales of the Fourier components.

safety factor profile. The time step is $dt[\omega_{ci}^{-1}] = 20$ ($dt[\omega_s^{-1}] = 0.04$).[4]

The frequency spectra of the zonal electric field for these four cases are shown in Fig. 8.4. The inclusion of the higher n-modes changes the GAM spectrum, it leads to the rise of a clear global zonal structure. In particular, in Fig. 8.4a with $n = [0, 40]$ one can see a continuum GAM spectrum near the plasma edge, which is well predicted by the linear analytical theory [30]. In the case with $n = [0, 60]$, one can already observe the formation of some global structure much closer to the plasma core ($s \sim [0.7, 0.8]$, Fig. 8.4b) with a frequency around $\omega[\omega_s] \sim 1.2$. If we keep increasing the toroidal mode numbers (Fig. 8.4c), we make the global structure to be the dominant one and much more pronounced than the continuum GAM branch. Finally, by taking into account the full ITG spectrum ($n = [0, 128]$, Fig. 8.4d), we increase the contribution of the global structure near the plasma edge. The GAM spectra for the cases with $n = [0, 60]$ and $n = [0, 80]$ are shown in Fig. 8.5 keeping the same plot scale. From these plots, one can clearly see that the global structure appears as an additional frequency branch of the zonal signal. At the same time, the continuum part of the mode remains practically unchanged when one includes higher toroidal mode numbers. The resulting global mode is strongly elongated in the radial direction ($s \sim [0.7, 0.97]$), its frequency is close to the continuum GAM

In particular, the TCV simulations have been simulated with $n_{nodes} = 30, n_{cpu} = 32, n_{clones} = 3$ for $max(n) = 80$, and $n_{nodes} = 33, n_{cpu} = 48, n_{clones} = 3$ for $max(n) = 128$.

[4]To keep the temperature radial profile constant in time, the so-called Krook operator (see Sections 3.3 and 3.4 in [27]), which is an artificial counterpart of the collisional operator presented in Sec. 4.3, is imposed. Here, we keep the same value of the Krook relaxation coefficient $\gamma_{rel}[\omega_s] = 0.066$ ($\gamma_{rel}[\omega_{ci}] = 1.4 \cdot 10^{-4}$) that was used in the original work [53].

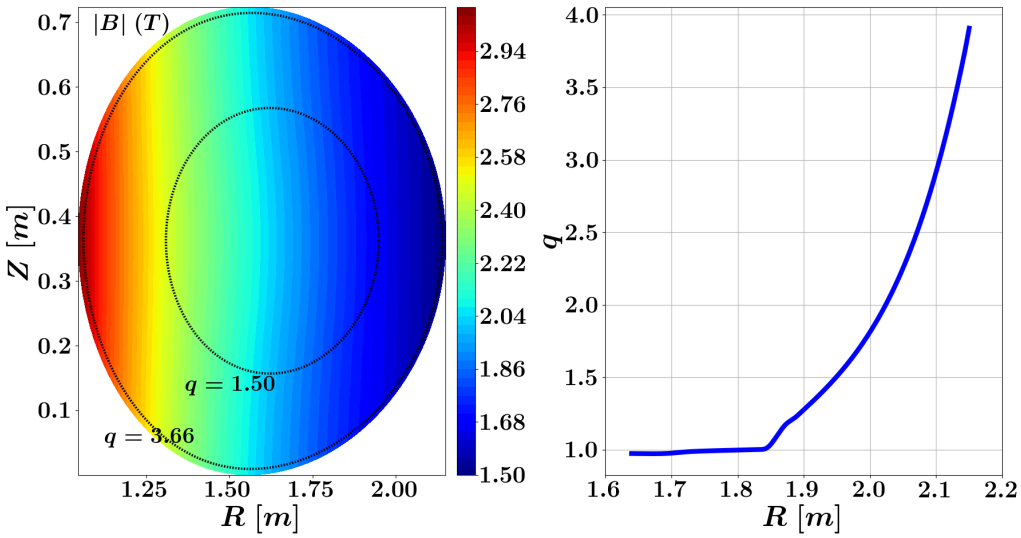

Figure 8.6: AUG discharge #20787 (see [49]): magnetic field configuration (left plot), the radial profile of the safety factor (right plot) used in the GK simulations. In the right plot, the indicated radial domain in meters $R[m]$ corresponds to the normalised radial interval $s = [0.0, 1.0]$ (however, the actual simulated plasma domain is $s = [0.4, 1.0]$).

frequency at the very edge of the plasma system, and remains the same in the whole radial interval.

8.2 Staircase GAM frequency spectrum in the AUG discharge

In Sec. 4.4, we have considered the linear GAM frequency spectra in the AUG discharge #20787 (see [49] for more details about the experimental plasma parameters of this shot) by using the fitting equation 4.1. This formula was obtained from linear gyrokinetic simulations. Although according to Fig. 4.6, it gives a reasonable estimation of the GAM frequency near the plasma edge, it does not predict the observed staircase behaviour of the mode spectrum. In this section, we are going to consider nonlinear GK simulations of the same AUG discharge, where the ITG drift instabilities generate the zonal modes through the mode coupling as it was described in Sec. 1.5.

The modelling of the deuterium plasma is performed electrostatically with adi-

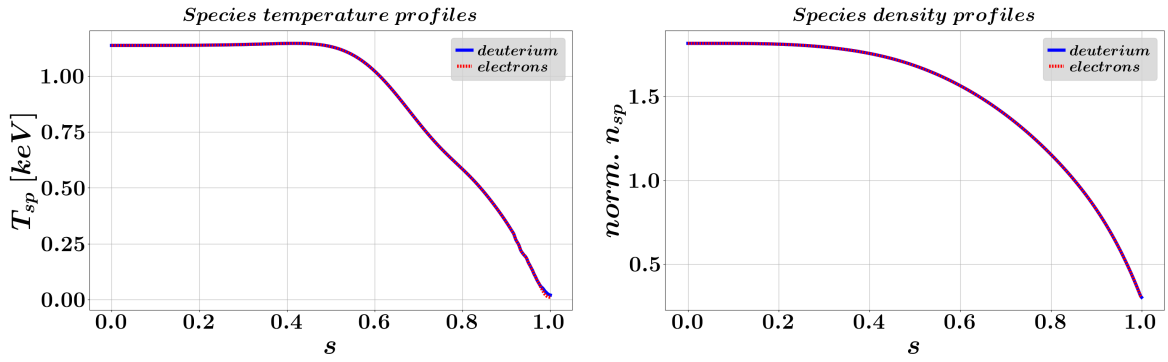

Figure 8.7: GK simulations of the AUG discharge #20787: species temperature and density profiles.

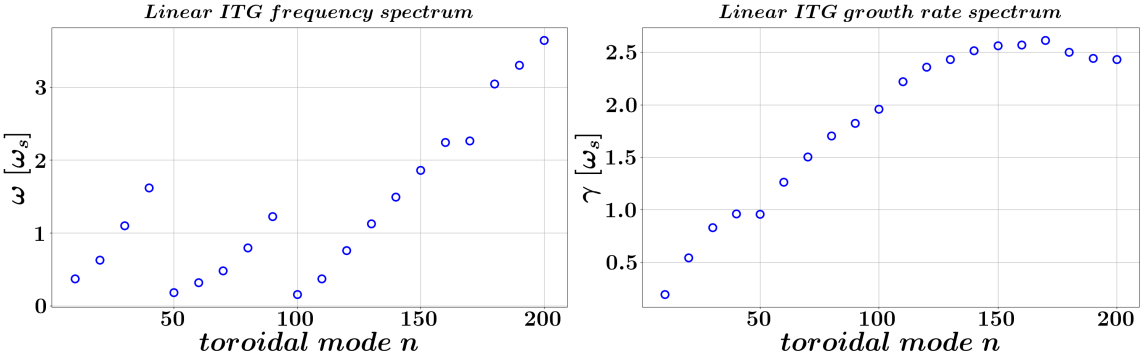

Figure 8.8: Linear GK simulations of the AUG discharge #20787: ITG frequency and growth rate spectra. The frequency and growth rate are normalised to the sound frequency ω_s.

abatic electrons. The magnetic field configuration is reconstructed from the experimental data using the code CHEASE (Fig. 8.6), where the poloidal cross-section of the background magnetic field is slightly elongated ($\kappa_{edge} \approx 1.1$). The major radius is $R_0 = 1.65\ m$, the minor radius is $a_0 = 0.5\ m$, and the magnetic field at the magnetic axis is $B_0 = 2.0\ T$. The temperature and density profiles are taken close to the experimental ones (Fig. 8.7), where the species temperatures are slightly different from each other ($\tau_e = T_e/T_i < 1$) just at the very edge of the plasma system.

As in the case discussed in the previous section, linear ITG frequency and growth rate spectra are calculated in linear GK simulations, and are indicated in Fig. 8.8. A

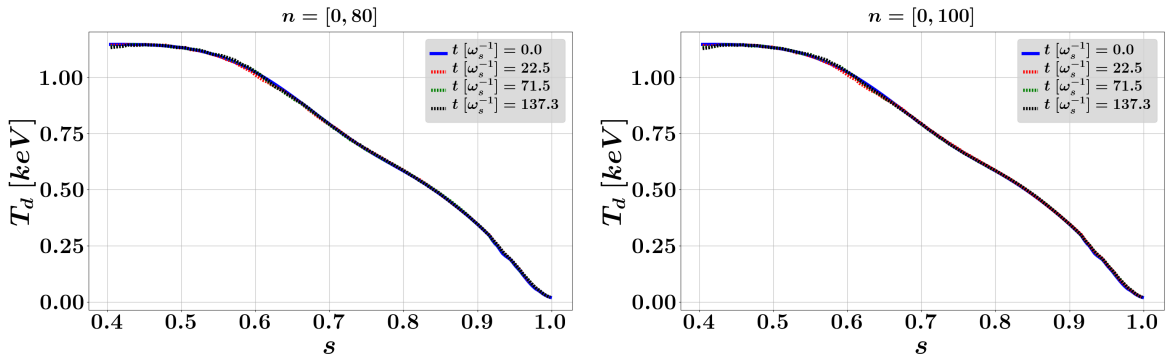

Figure 8.9: NL simulations of the AUG discharge #20787: evolution in time of the deuterium temperature profile for different ITG spectra. One can see that the temperature profiles remain unchanged during the simulations due to the imposed Krook operator.

mode with some toroidal number n can actually have several frequencies and growth rates that correspond, for example, to different poloidal numbers m. In Fig. 8.8, we indicate only the modes with the highest growth rates and corresponding frequencies. According to the linear computation, the most unstable mode is around $n = 170$ ($k_\phi \rho_i \approx 0.04$ and $k_\chi \rho_i \approx 1.37$, see Eq. 8.1). We are going to consider several NL simulations with different toroidal spectra:

$$n = [0, 40],\ m = [-165, 165],\ n_\phi = 192,\ n_\chi = 384,\ N_d = 2.4 \cdot 10^8, \quad (8.7)$$
$$n = [0, 60],\ m = [-245, 245],\ n_\phi = 288,\ n_\chi = 576,\ N_d = 3.6 \cdot 10^8, \quad (8.8)$$
$$n = [0, 80],\ m = [-325, 325],\ n_\phi = 336,\ n_\chi = 672,\ N_d = 4.8 \cdot 10^8, \quad (8.9)$$
$$n = [0, 100],\ m = [-405, 405],\ n_\phi = 432,\ n_\chi = 864,\ N_d = 6.0 \cdot 10^8. \quad (8.10)$$

The radial resolution is $n_s = 1200$ in all the cases since we keep the same radial size of the plasma system ($s = [0.4, 1.0]$), which is reduced to include only the radial domain with the non-zero temperature gradient, where the ITG modes can develop (compare to the temperature profile in Fig. 8.7). The time step is $dt[\omega_{ci}^{-1}] = 20$ ($dt[\omega_s^{-1}] = 0.01$). To keep the temperature radial profile constant in time (Fig. 8.9), the Krook operator is imposed with the relaxation coefficient $\gamma_{rel}[\omega_s] = 0.178$ ($\gamma_{rel}[\omega_{ci}] = 1.00 \cdot 10^{-4}$), which is around $\max(\gamma_{ITG})/14$ according to Fig. 8.8. The reference radial point is $s_0 = 0.95$, where $T_e(s_0) = 0.165\ keV$[5].

[5] $\omega_s = 53.9 \cdot 10^3\ rad/s = 8.6\ kHz$.

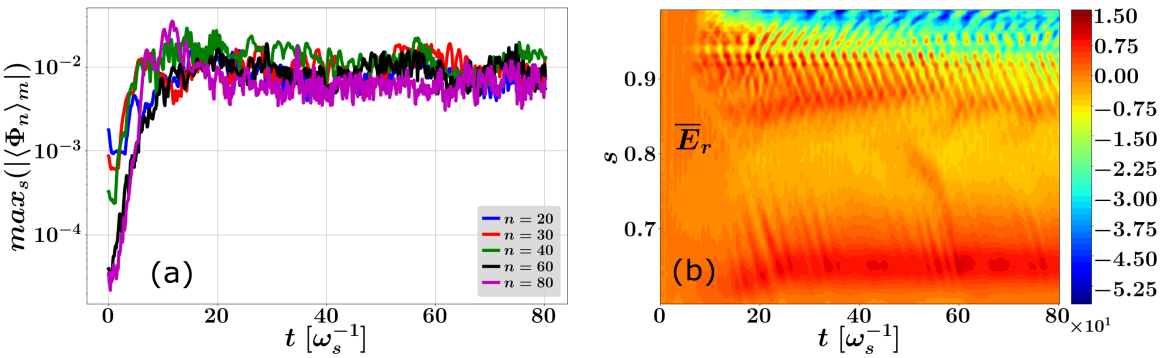

Figure 8.10: Nonlinear GK simulation of the AUG discharge #20787 with $n = [0, 80]$. Fig. 8.10a: evolution in time of the electrostatic potential for different toroidal n-modes that is summed up on all corresponding poloidal mode numbers m. At every time moment we consider the absolute maximum value of the potential in space. Fig. 8.10b: evolution in time of the radial structure of the zonal electric field $\overline{E}_r$ excited by the ITG instabilities.

One can see the evolution in time of different n-modes in the nonlinear simulation with $n = [0, 80]$ in Fig. 8.10a. Although the higher n-modes can have higher initial growth rates, their saturation levels are lower. In particular, it is the modes around $n \sim 40$ that have the highest saturation amplitudes, while the $n = 80$ mode being the strongest at the beginning decreases in time that might indicate the energy transfer from this mode to the zonal structures. This means that the ITG modes with even higher toroidal numbers can have significant contribution to the GAM evolution. Moreover, one can see from Fig. 8.10b that the GAM oscillations (yellow-red stripes propagating inward for $s < 0.94$ and mostly outward for $s > 0.94$) are concentrated near the plasma edge $s \sim [0.85, 1.0]$ (compare also to Fig. 8.12), while the stationary zonal modes are localised closer to the core ($s \sim 0.65$). One of the reasons is a higher safety factor value and lower plasma temperature near the edge that lead to a lower GAM damping rate (see Eqs. 3.67 and 4.2). Since the ITG modes with high toroidal numbers are also localised near the plasma edge (Fig. 8.11), they might be important for the GAM excitation, as it was observed in the previous section.

In Fig. 8.12 the frequency spectrum of the zonal electric field is displayed. First of all, one can see that the nonlinear results follow the tendency predicted by the linear GK simulations and the analytical theory. Besides, the resulting numerical GAM frequency has the order of magnitude close to the experimental data. Consistently with the TCV case, a broader ITG spectrum results in the generation of a

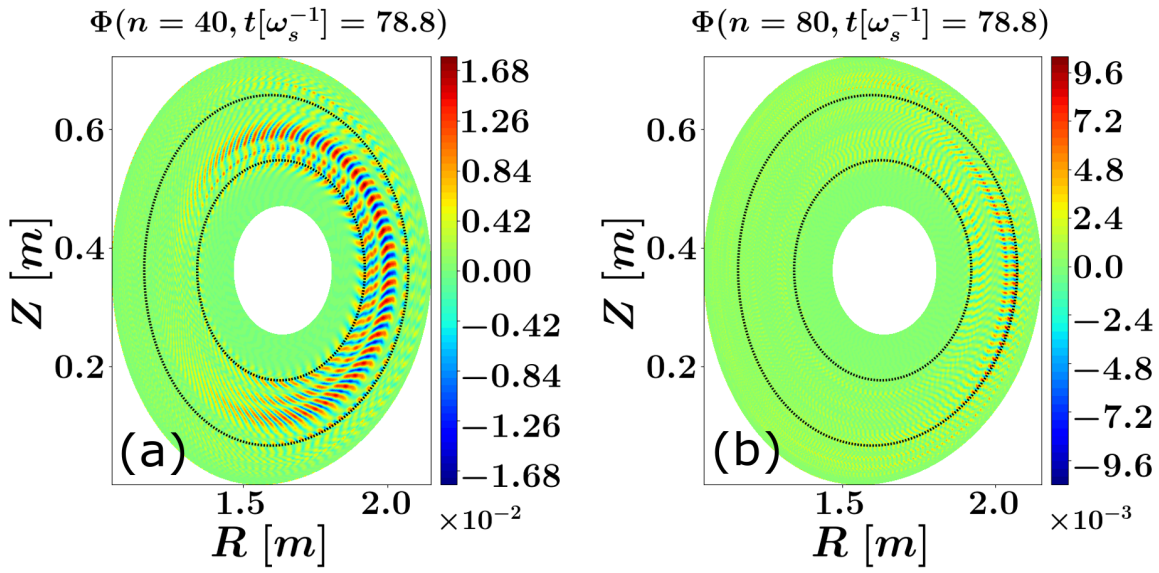

Figure 8.11: NL simulations of the AUG discharge #20787 with $n = [0, 80]$. Poloidal structure of the $n = 40$ mode (Fig. 8.11a) and of the $n = 80$ mode (Fig. 8.11b). The black dotted lines indicate the radial positions $s = 0.65$ and $s = 0.90$, respectively.

global (more precisely, staircase) GAM structure. One can see a radially elongated formation ($s \sim [0.86, 0.94]$) around the frequency $\omega[\omega_s] \approx 2.85$, which is however shifted with respect to the experimental plateau observed at $\omega[\omega_s] \approx 2.36$. This structure appears only if we take into account the ITG modes with $n > 60$. Besides, by comparing Figs. 8.12c and 8.12d, one can notice that the $n > 80$ modes amplify the GAM frequencies around $\omega[\omega_s] \sim 2.3$ at $s \sim 0.96$, which is close to the experimental spectrum. One of the possible explanations of the difference between the numerical and experimental frequencies, where the plateaus are observed, is the absence of the plasma rotation in the nonlinear simulations. In the studied discharge the plasma was heated by the neutral-beam injection that might lead to the plasma rotation, which in its turn can shift the GAM frequency. As it was mentioned before, the plasma rotation might not only change the GAM frequency, but also facilitate the development of the global GAM formations. Finally, we should note that the current nonlinear simulations have been performed with adiabatic electrons that exclude some instabilities, such as the Trapped Electron Mode (TEM), from the consideration. These modes can also excite the zonal structures and might significantly improve the numerical prediction of the GAM spectrum. However, the

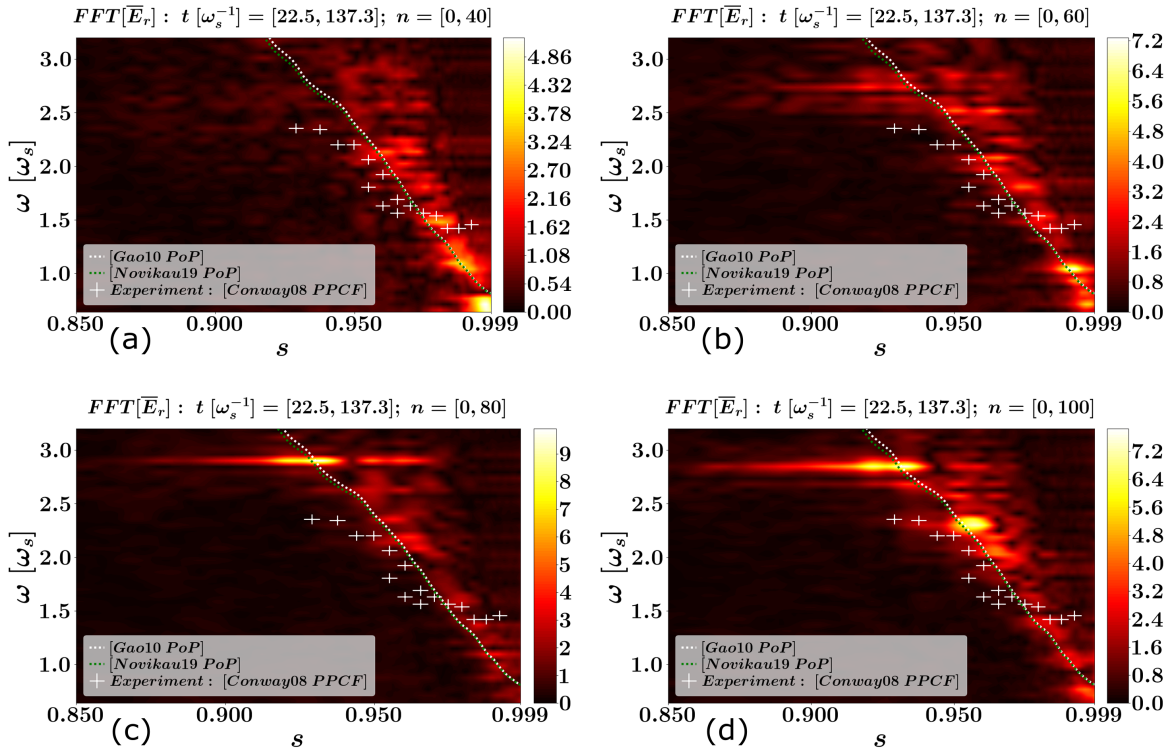

Figure 8.12: NL simulations of the AUG discharge #20787. The contour plots present the frequency spectra of the zonal electric field found in the time interval $t[\omega_s^{-1}] = [22.5, 137.3]$. Different ITG spectra are considered here: $n = [0, 40]$ (Fig. 8.12a), $n = [0, 60]$ (Fig. 8.12b), $n = [0, 80]$ (Fig. 8.12c), $n = [0, 100]$ (Fig. 8.12d). The white crosses indicate the experimental GAM spectrum [49]. The dotted lines show the estimation of the linear mode spectrum from the Gao analytical theory [30] (white line) and from the fitting equation 4.1 (green line).

corresponding simulations will require a more substantial amount of computational resources.

8.3 Discussion and chapter summary

The results presented in this Chapter should be considered as the first step in the numerical study of the GAM nonlinear excitation by turbulence in realistic magnetic configurations. It was shown that relatively simple nonlinear electrostatic models

with adiabatic electrons can reproduce the order of the GAM frequency, and even describe the formation of the global zonal structures. Besides, it was demonstrated that the ITG modes with high toroidal mode numbers play a crucial role for the GAM formation, and must be taken into account for the quantitative comparison with experimental data.

In the performed computations, the zonal structures have been excited by the non-zonal (turbulent) field that naturally arises due to the presence of the plasma temperature gradient. Instead of the self-consistent field, one can apply an external ES potential ("antenna") with a predefined space structure (e.g. with a particular toroidal mode number) and with a constant oscillation frequency. In such a way, it is possible to simplify the plasma system and to focus on the ITG-ZS interaction, where one of the modes (the ITG or the zonal mode) is fixed. As a result, one can explore the ZS excitation by the drift instabilities forgetting about the ZS feedback on the original ITG (see, for example, [113]). Conversely, if one fixes the zonal mode, one can concentrate on the shearing of the turbulence eddies by the zonal structures [114, 113], and study how the oscillatory nature of the GAMs changes the ZS impact on the turbulence. These studies are left for future work.

Chapter 9

Conclusions and outlook

In tokamak plasmas, drift instabilities such as the Ion-Temperature Gradient (ITG) mode give rise to Zonal Structures (ZSs) that shear turbulent cells and, consequently, reduce radial transport in the plasma systems. The nonlinear interactions between the Geodesic Acoustic Modes (GAMs), which are the oscillatory part of the ZSs, and the turbulence is determined to a high degree by the GAM damping rate. Lack of experimental data of this characteristic makes the results from gyrokinetic simulations particularly important for analytical and numerical investigation of the nonlinear GAM-ITG systems. Linear gyrokinetic simulations performed with drift-kinetic electrons and compared to analytical theories derived with adiabatic electrons have shown significant enhancement of the Landau damping of the geodesic modes. The phase mixing process that takes place in the case with finite temperature and safety factor gradients increases the mode damping rate as well (again in agreement with theory). The GK simulations with drift-kinetic electrons demonstrated a decrease of the GAM half-decay times in comparison to previous estimations based on the adiabatic electron approximation. The collisional damping of the mode has been estimated to be negligible, except in a narrow zone near the plasma edge.

Energetic particles can drive the geodesic modes, and the resulting global mode, called EGAM, have a significant influence on the EP dynamics and the plasma confinement. This mode provides an additional mechanism of the energy exchange between the energetic and thermal species enhancing the direct heating of the bulk ions. The significant progress made in the last decade in studying the EGAM physics has been expanded here, by including drift-kinetic electrons and the geometrical effects of a realistic magnetic shape in numerical modelling. Nonlinear global GK simulations of the EGAMs in an ASDEX Upgrade discharge have reproduced the mode relative up-chirping close to the experimental one. It has been demonstrated

that the GK code ORB5 can handle electrostatic zonal structures and anisotropic distribution functions properly in experimentally relevant cases which is a crucial ingredient before going onto more complex plasma systems. A general correlation between the mode level and the EP-thermal plasma energy exchange has been revealed. More precisely, it has been shown that having the same mode levels, one can achieve a higher energy exchange between energetic and thermal species through an EGAM by adjusting EP parameters.

To investigate the mode-particle interaction, a Mode-Particle-Resonance (MPR) diagnostic has been implemented in the code ORB5. The technique gives access to energy transfer signals between an ES mode and particles in phase space providing a way to localise mode-particle resonances. As in the case with GAMs, the drift-kinetic electrons exhibit a significant influence on the EGAM behaviour. Using the MPR technique, it has been revealed that the geodesic modes are damped by electrons due to the resonance with mainly barely trapped electrons, whose characteristic velocities are close to the mode phase speed. It has been indicated that although the EGAM transfers most of its energy to the thermal ions, and not to the electrons, the electron dynamics might significantly reduce the plasma heating by EGAMs by lowering the mode amplitude.

The current version of the MPR diagnostic can be applied only to the case of mainly electrostatic modes, such as GAMs or EGAMs. The reason is in the choice of the velocity space variables in ORB5. The MPR technique can be extended to work with EM simulations with arbitrary β_e, by performing a proper transition from the canonical variable p_z to the parallel velocity variable $v_\parallel$. There are different possible applications of the EM-MPR diagnostic. A more comprehensive range of the modes whose dynamics is mainly controlled by wave-particle resonances, like energetic-particle driven MHD instabilities, can be investigated. For a turbulent plasma, the collisionless interactions between EM fields and plasma particles can lead to secular field-particle energy exchange. It can result in collisionless damping of the turbulent fluctuations. More precisely, a particular challenge in plasma physics consists in the identification of the physical mechanisms by which the EM field and plasma flow fluctuations are damped and how their energy is converted to plasma heat or some other energization of particles. For example, in astrophysical plasma dissipation of the turbulent energy through the Landau damping of the Alfvén waves can take place [115]. There are also physical phenomena, which are specific to the space plasma, such as particle acceleration by the magnetic energy released during collisions of the magnetic islands in solar and heliospheric environments [116]. It might be interesting to investigate the role of such processes in tokamak plasmas as well.

Linear GAM simulations have predicted a continuum mode frequency spectrum, where the mode frequency changes consistently to plasma temperature profiles and magnetic field configuration. Nonlinear GK modelling of an AUG discharge, where the zonal structures are directly excited by the ITG drift instabilities, has been performed. It was shown that the inclusion of the ITG modes with higher toroidal mode numbers, which are localised closer to the plasma edge, can significantly change the GAM spectrum. The same tendency was observed in the nonlinear GK computation of the TCV magnetic configuration. It was demonstrated that the high-n ITG modes are responsible for the formation of a global GAM-like structure elongated in the radial direction. However, in the AUG case, we have obtained a GAM spectrum upshifted with respect to the experimental data. This inconsistency might be explained by the plasma rotation that should take place in the experiment due to the neutral beam heating, but was not included in the GK simulations.

The nonlinear simulations open a broad range of topics for theoretical and practical oriented studies related to the ITG-ZS interaction. One of the possible directions to move in is the application of an electrostatic field with a fixed space structure to plasma systems. In this way, one can investigate solely either the ZS excitation or the turbulence shearing excluding from the modelling one of the branches of the ITG-ZS interaction. From one point of view, it will give a new numerical method for the comparison with analytical theories. On the other hand, it will help to extract essential new pieces of the tokamak plasma physics from the gyrokinetic simulations. The final goal is a complete understanding of the complex interactions which determine the saturation of turbulence in toroidal plasmas, and thus predict the performance of a future fusion reactor.

Appendix A

Evaluation of the Plasma Dispersion Function

The Plasma Dispersion Function (PDF)

$$\mathcal{Z}(z) = \frac{1}{\sqrt{\pi}} \int_{-\infty}^{+\infty} \frac{\exp(-t^2)}{t - z} \, \mathrm{d}t \tag{A.1}$$

is defined for the case of $Im(z) > 0$ (here, z is equivalent to a complex wave frequency). Since we are dealing with the Landau damping, we have to analytically extend this integral to the case of $Im(z) < 0$. The analytical continuation is carried out in such a way that the path of the integration is deformed into a contour for which the pole z is always sitting on the left hand side as indicated in Fig. A.1. Now, we can consider a closed contour $\Gamma = C_\gamma + C_R$, as it is shown in Fig. A.1, where C_γ goes along a real axis and is curved near the pole z to keep it on the left hand side, and C_R is a half circle with a radius $R \to +\infty$. By denoting the integrand of the PDF as $G(t, z)$

$$G(t, z) = \frac{1}{\sqrt{\pi}} \frac{\exp(-t^2)}{t - z}, \tag{A.2}$$

we have the following equation

$$\int_\Gamma G(t, z) \, \mathrm{d}t = \int_{C_\gamma} G(t, z) \, \mathrm{d}t + \int_{C_R} G(t, z) \, \mathrm{d}t. \tag{A.3}$$

Since

$$\lim_{R \to +\infty} G(t, z) = 0, \tag{A.4}$$

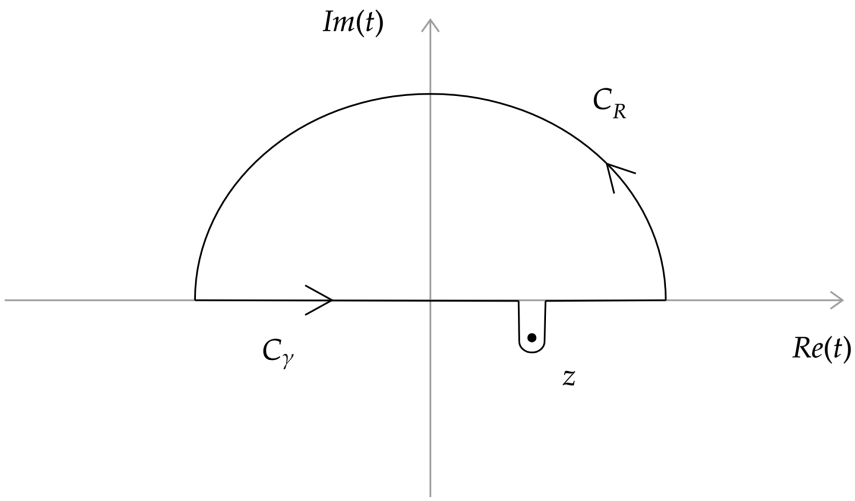

Figure A.1: Domain of integration of the Plasma Dispersion Function. The contour C_γ is curved in such a way to keep the pole z on the left hand said. After that, we assume that the pole falls on the contour C_γ from the domain surrounded by a closed contour $\Gamma = C_\gamma + C_R$.

the second integral on the right hand side of Eq. A.3 is equal to 0. The integral along the C_γ in the limit of a big radius R represents the analytical continuation of the PDF. If we assume that the pole z is sitting on the curved contour, we can evaluate the PDF using the principle value integral, more precisely, by applying the Sokhotski - Plemelj theorem:

$$\int_\Gamma G(t,z)\,\mathrm{d}t = \int_{C_\gamma} G(t,z)\,\mathrm{d}t = P.V\int_{C_\gamma} G(t,z)\,\mathrm{d}t - i\sqrt{\pi}\exp(-z^2). \tag{A.5}$$

Now, for the sake of numerical calculations, we would like to relate the principle value integral to the Imaginary Error Function Erfi(z). It is known that the Hilbert transform of the Gaussian can be related to Erfi(z) (Ref. [117]) as

$$\frac{1}{\sqrt{\pi}}P.V.\int_{-\infty}^{+\infty}\frac{\exp(-t^2)}{t-z}\,\mathrm{d}t = -\sqrt{\pi}\exp(-z^2)\mathrm{Erfi}(z). \tag{A.6}$$

Finally, the Plasma Dispersion Function $\mathcal{Z}(z)$, analytically extended to the lower half of the imaginary plane, can be expressed using the following equation:

$$\mathcal{Z}(z) = -\sqrt{\pi}\exp(-z^2)(i + \mathrm{Erfi}(z)). \tag{A.7}$$

Bibliography

[1] Live chart of nuclides, nuclear structure and decay data, 2019. URL: https://www-nds.iaea.org/relnsd/vcharthtml/VChartHTML.html.

[2] Fundamental physical constants, 2018. URL: https://physics.nist.gov/cuu/Constants/Table/allascii.txt.

[3] G. R. Caughlan, W. A. Fowler, M. J. Harris, B. A. Zimmerman, Tables of thermonuclear reaction rates for low-mass nuclei, Atomic Data and Nuclear Data Tables 32 (1985) 197 – 233. doi:https://doi.org/10.1016/0092-640X(85)90006-3.

[4] Caughlan, Fowler, Reaction rate directory (1988). URL: http://www.nuclear.csdb.cn/data/CF88/directory.html#006.

[5] J. D. Lawson, Some criteria for a power producing thermonuclear reactor, Proceedings of the Physical Society. Section B 70 (1957) 6–10. doi:10.1088/0370-1301/70/1/303.

[6] J. Wesson, Tokamaks: Second Edition, Oxford University Press, 1997. URL: https://www.amazon.com/Tokamaks-Oxford-Engineering-Science-Wesson/dp/0198562934.

[7] P. Manz, M. Ramisch, U. Stroth, Physical mechanism behind zonal-flow generation in drift-wave turbulence, Phys. Rev. Lett. 103 (2009) 165004. doi:10.1103/PhysRevLett.103.165004.

[8] A. Hasegawa, C. G. Maclennan, Y. Kodama, Nonlinear behavior and turbulence spectra of drift waves and rossby waves, The Physics of Fluids 22 (1979) 2122–2129. doi:10.1063/1.862504.

[9] M. N. Rosenbluth, F. L. Hinton, Poloidal flow driven by ion-temperature-gradient turbulence in tokamaks, Phys. Rev. Lett. 80 (1998) 724–727. doi:10.1103/PhysRevLett.80.724.

[10] P. H. Diamond, S.-I. Itoh, K. Itoh, T. S. Hahm, Zonal flows in plasma—a review, Plasma Physics and Controlled Fusion 47 (2005) R35–R161. doi:10.1088/0741-3335/47/5/r01.

[11] Ö. D. Gürcan, P. H. Diamond, Zonal flows and pattern formation, Journal of Physics A: Mathematical and Theoretical 48 (2015) 293001. doi:10.1088/1751-8113/48/29/293001.

[12] H. Biglari, P. H. Diamond, P. W. Terry, Influence of sheared poloidal rotation on edge turbulence, Physics of Fluids B: Plasma Physics 2 (1990) 1–4. doi:10.1063/1.859529.

[13] P. Manz, G. S. Xu, B. N. Wan, H. Q. Wang, H. Y. Guo, I. Cziegler, N. Fedorczak, C. Holland, S. H. Mueller, S. C. Thakur, M. Xu, K. Miki, P. H. Diamond, G. R. Tynan, Zonal flow triggers the l-h transition in the experimental advanced superconducting tokamak, Physics of Plasmas 19 (2012) 072311. doi:10.1063/1.4737612.

[14] L. Schmitz, L. Zeng, T. L. Rhodes, J. C. Hillesheim, E. J. Doyle, R. J. Groebner, W. A. Peebles, K. H. Burrell, G. Wang, Role of zonal flow predator-prey oscillations in triggering the transition to h-mode confinement, Phys. Rev. Lett. 108 (2012) 155002. doi:10.1103/PhysRevLett.108.155002.

[15] N. Chakrabarti, R. Singh, P. K. Kaw, P. N. Guzdar, Nonlinear excitation of geodesic acoustic modes by drift waves, Physics of Plasmas 14 (2007) 052308. doi:10.1063/1.2732167.

[16] F. Zonca, L. Chen, Radial structures and nonlinear excitation of geodesic acoustic modes, EPL (Europhysics Letters) 83 (2008) 35001. doi:10.1209/0295-5075/83/35001.

[17] Z. Qiu, L. Chen, F. Zonca, Excitation of kinetic geodesic acoustic modes by drift waves in nonuniform plasmas, Physics of Plasmas 21 (2014) 022304. doi:10.1063/1.4863973.

[18] B. Scott, The geodesic transfer effect on zonal flows in tokamak edge turbulence, Physics Letters A 320 (2003) 53 – 62. doi:https://doi.org/10.1016/j.physleta.2003.10.080.

[19] A. Kendl, B. D. Scott, Shear flow reduction by the geodesic transfer mechanism in tokamak edge turbulence, Physics of Plasmas 12 (2005) 064506. doi:10.1063/1.1938147.

[20] Z. Qiu, L. Chen, F. Zonca, Kinetic theory of geodesic acoustic modes in toroidal plasmas: a brief review, Plasma Science and Technology 20 (2018) 094004. doi:10.1088/2058-6272/aab4f0.

[21] N. Winsor, J. L. Johnson, J. M. Dawson, Geodesic acoustic waves in hydromagnetic systems, The Physics of Fluids 11 (1968) 2448–2450. doi:10.1063/1.1691835.

[22] J. P. Freidberg, Ideal MHD, Cambridge University Press, 2014. doi:10.1017/CBO9780511795046.

[23] H. Zohm, The MHD Equations, John Wiley and Sons, Ltd, 2015. doi:10.1002/9783527677375.ch1.

[24] A. Biancalani, Interaction of geodesic acoustic modes and energetic particles in tokamak plasmas, HDR thesis, Sorbonne University, Paris, France, 2019. URL: http://www2.ipp.mpg.de/~biancala/publications/.

[25] S. Jolliet, A. Bottino, P. Angelino, R. Hatzky, T. Tran, B. Mcmillan, O. Sauter, K. Appert, Y. Idomura, L. Villard, A global collisionless pic code in magnetic coordinates, Computer Physics Communications 177 (2007) 409 – 425. doi:https://doi.org/10.1016/j.cpc.2007.04.006.

[26] A. Bottino, E. Sonnendruecker, Monte carlo particle-in-cell methods for the simulation of the vlasov–maxwell gyrokinetic equations, Journal of Plasma Physics 81 (2015) 435810501. doi:10.1017/S0022377815000574.

[27] E. Lanti, N. Ohana, N. Tronko, T. Hayward-Schneider, A. Bottino, B. McMillan, A. Mishchenko, A. Scheinberg, A. Biancalani, P. Angelino, S. Brunner, J. Dominski, P. Donnel, C. Gheller, R. Hatzky, A. Jocksch, S. Jolliet, Z. Lu, J. M. Collar, I. Novikau, E. Sonnendruecker, T. Vernay, L. Villard, Orb5: A global electromagnetic gyrokinetic code using the pic approach in toroidal geometry, Computer Physics Communications (2019) 107072. doi:https://doi.org/10.1016/j.cpc.2019.107072.

[28] H. Sugama, T.-H. Watanabe, Erratum: 'collisionless damping of geodesic acoustic modes' [j. plasma physics (2006) 72, 825], Journal of Plasma Physics 74 (2008) 139–140. doi:10.1017/S002237780700668X.

[29] Z. Qiu, L. Chen, F. Zonca, Collisionless damping of short wavelength geodesic acoustic modes, Plasma Physics and Controlled Fusion 51 (2008) 012001. doi:10.1088/0741-3335/51/1/012001.

[30] Z. Gao, Plasma shaping effects on the geodesic acoustic mode in the large orbit drift width limit, Physics of Plasmas 17 (2010) 092503. doi:10.1063/1.3481464.

[31] Z. Gao, Collisional damping of the geodesic acoustic mode, Physics of Plasmas 20 (2013) 032501. doi:10.1063/1.4794339.

[32] H. S. Zhang, Z. Lin, Trapped electron damping of geodesic acoustic mode, Physics of Plasmas 17 (2010) 072502. doi:10.1063/1.3447879.

[33] A. Biancalani, A. Bottino, C. Ehrlacher, V. Grandgirard, G. Merlo, I. Novikau, Z. Qiu, E. Sonnendruecker, X. Garbet, T. Goerler, S. Leerink, F. Palermo, D. Zarzoso, Cross-code gyrokinetic verification and benchmark on the linear collisionless dynamics of the geodesic acoustic mode, Physics of Plasmas 24 (2017) 062512. doi:10.1063/1.4985571.

[34] I. Novikau, A. Biancalani, A. Bottino, G. D. Conway, Ö. D. Gürcan, P. Manz, P. Morel, E. Poli, A. Di Siena, Linear gyrokinetic investigation of the geodesic acoustic modes in realistic tokamak configurations, Physics of Plasmas 24 (2017) 122117. doi:10.1063/1.5003784.

[35] C. Ehrlacher, X. Garbet, V. Grandgirard, Y. Sarazin, P. Donnel, E. Caschera, P. Ghendrih, D. Zarzoso, Contribution of kinetic electrons to GAM damping, Journal of Physics: Conference Series 1125 (2018) 012010. doi:10.1088/1742-6596/1125/1/012010.

[36] V. Grandgirard, X. Garbet, C. Ehrlacher, A. Biancalani, A. Bottino, I. Novikau, Y. Asahi, E. Caschera, G. Dif-Pradalier, P. Donnel, P. Ghendrih, C. Gillot, G. Latu, C. Passeron, Y. Sarazin, D. Zarzoso, Linear collisionless dynamics of the gam with kinetic electrons: Comparison simulations/theory, Physics of Plasmas 26 (2019) 122304. doi:10.1063/1.5113679.

[37] H. Berk, C. Boswell, D. Borba, A. Figueiredo, T. Johnson, M. Nave, S. Pinches, S. Sharapov, J. E. contributors, Explanation of the JETn= 0 chirping mode, Nuclear Fusion 46 (2006) S888–S897. doi:10.1088/0029-5515/46/10/s04.

[38] D. Zarzoso, A. Biancalani, A. Bottino, P. Lauber, E. Poli, J.-B. Girardo, X. Garbet, R. Dumont, Analytic dispersion relation of energetic particle driven geodesic acoustic modes and simulations with NEMORB, Nuclear Fusion 54 (2014) 103006. doi:10.1088/0029-5515/54/10/103006.

[39] F. Palermo, A. Biancalani, C. Angioni, F. Zonca, A. Bottino, Combined action of phase-mixing and landau damping causing strong decay of geodesic acoustic modes, EPL (Europhysics Letters) 115 (2016) 15001. doi:10.1209/0295-5075/115/15001.

[40] A. Biancalani, F. Palermo, C. Angioni, A. Bottino, F. Zonca, Decay of geodesic acoustic modes due to the combined action of phase mixing and landau damping, Physics of Plasmas 23 (2016) 112115. doi:10.1063/1.4967703.

[41] Z. Qiu, L. Chen, Kinetic theories of geodesic acoustic modes: Radial structure, linear excitation by energetic particles and nonlinear saturation, Plasma Science and Technology 13 (2011) 257–266. doi:10.1088/1009-0630/13/3/01.

[42] W. Horton, Drift waves and transport, Rev. Mod. Phys. 71 (1999) 735–778. doi:10.1103/RevModPhys.71.735.

[43] W. Horton, D. Choi, W. M. Tang, Toroidal drift modes driven by ion pressure gradients, The Physics of Fluids 24 (1981) 1077–1085. doi:10.1063/1.863486.

[44] S. Kobayashi, Ö. D. Gürcan, P. H. Diamond, Direct identification of predator-prey dynamics in gyrokinetic simulations, Physics of Plasmas 22 (2015) 090702. doi:10.1063/1.4930127.

[45] L. Chen, Z. Lin, R. White, Excitation of zonal flow by drift waves in toroidal plasmas, Physics of Plasmas 7 (2000) 3129–3132. doi:10.1063/1.874222.

[46] F. Zonca, R. B. White, L. Chen, Nonlinear paradigm for drift wave–zonal flow interplay: Coherence, chaos, and turbulence, Physics of Plasmas 11 (2004) 2488–2496. doi:10.1063/1.1652811.

[47] P. N. Guzdar, R. G. Kleva, L. Chen, Shear flow generation by drift waves revisited, Physics of Plasmas 8 (2001) 459–462. doi:10.1063/1.1340618.

[48] K. Nishikawa, M. Wakatani, Plasma Physics: Third Edition, Springer Science and Business Media, 2000. URL: https://link.springer.com/book/10.1007%2F978-3-662-04078-2.

[49] G. D. Conway, C. Troester, B. Scott, K. Hallatschek, the ASDEX Upgrade Team, Frequency scaling and localization of geodesic acoustic modes in ASDEX upgrade, Plasma Physics and Controlled Fusion 50 (2008) 055009. doi:10.1088/0741-3335/50/5/055009.

[50] G. Wang, W. A. Peebles, T. L. Rhodes, M. E. Austin, Z. Yan, G. R. McKee, R. J. La Haye, K. H. Burrell, E. J. Doyle, J. C. Hillesheim, M. J. Lanctot, R. Nazikian, C. C. Petty, L. Schmitz, S. Smith, E. J. Strait, M. Van Zeeland, L. Zeng, Multi-field characteristics and eigenmode spatial structure of geodesic acoustic modes in diii-d l-mode plasmas, Physics of Plasmas 20 (2013) 092501. doi:10.1063/1.4819501.

[51] V. P. Lakhin, E. A. Sorokina, V. I. Ilgisonis, L. V. Konovaltseva, Mhd-model for low-frequency waves in a tokamak with toroidal plasma rotation and problem of existence of global geodesic acoustic modes, Plasma Physics Reports 41 (2015) 975–982. doi:10.1134/S1063780X15120077.

[52] G. Merlo, S. Brunner, Z. Huang, S. Coda, T. Goerler, L. Villard, A. B. Navarro, J. Dominski, M. Fontana, F. Jenko, L. Porte, D. Told, Investigating the radial structure of axisymmetric fluctuations in the TCV tokamak with local and global gyrokinetic GENE simulations, Plasma Physics and Controlled Fusion 60 (2018) 034003. doi:10.1088/1361-6587/aaa2dc.

[53] L. Villard, B. F. McMillan, E. Lanti, N. Ohana, A. Bottino, A. Biancalani, I. Novikau, S. Brunner, O. Sauter, N. Tronko, A. Mishchenko, Global turbulence features across marginality and non-local pedestal-core interactions, Plasma Physics and Controlled Fusion 61 (2019) 034003. doi:10.1088/1361-6587/aaf7e7.

[54] A. J. Brizard, T. S. Hahm, Foundations of nonlinear gyrokinetic theory, Rev. Mod. Phys. 79 (2007) 421–468. doi:10.1103/RevModPhys.79.421.

[55] R. Hatzky, A. Koenies, A. Mishchenko, Electromagnetic gyrokinetic pic simulation with an adjustable control variates method, Journal of Computational Physics 225 (2007) 568 – 590. doi:https://doi.org/10.1016/j.jcp.2006.12.019.

[56] A. Mishchenko, A. Bottino, R. Hatzky, E. Sonnendruecker, R. Kleiber, A. Koenies, Mitigation of the cancellation problem in the gyrokinetic particle-in-cell simulations of global electromagnetic modes, Physics of Plasmas 24 (2017) 081206. doi:10.1063/1.4997540.

[57] N. Tronko, A. Bottino, E. Sonnendruecker, Second order gyrokinetic theory for particle-in-cell codes, Physics of Plasmas 23 (2016) 082505. doi:10.1063/1.4960039.

[58] I. Novikau, A. Biancalani, A. Bottino, A. Di Siena, P. Lauber, E. Poli, E. Lanti, L. Villard, N. Ohana, S. Briguglio, Implementation of energy transfer technique in orb5 to study collisionless wave-particle interactions in phase-space, Comp. Phys. Comm. (2019). doi:10.1016/j.cpc.2019.107032.

[59] N. Tronko, C. Chandre, Second-order nonlinear gyrokinetic theory: from the particle to the gyrocentre, Journal of Plasma Physics 84 (2018) 925840301. doi:10.1017/S0022377818000430.

[60] A. Mishchenko, A. Bottino, A. Biancalani, R. Hatzky, T. Hayward-Schneider, N. Ohana, E. Lanti, S. Brunner, L. Villard, M. Borchardt, R. Kleiber, A. Koenies, Pullback scheme implementation in orb5, Computer Physics Communications 238 (2019) 194 – 202. doi:https://doi.org/10.1016/j.cpc.2018.12.002.

[61] H. Sugama, Gyrokinetic field theory, Physics of Plasmas 7 (2000) 466–480. doi:10.1063/1.873832.

[62] N. Miyato, B. D. Scott, D. Strintzi, S. Tokuda, A modification of the guiding-centre fundamental 1-form with strong e×b flow, Journal of the Physical Society of Japan 78 (2009) 104501. doi:10.1143/JPSJ.78.104501.

[63] W. D. D'haeseleer, W. N. G. Hitchon, J. L. Shohet, J. D. Callen, D. W. Kerst, Flux coordinates and magnetic field structure A guide to a fundamental tool of plasma theory, Springer, Germany, 1991. URL: http://inis.iaea.org/search/search.aspx?orig_q=RN:23003745.

[64] H. Luetjens, A. Bondeson, O. Sauter, The chease code for toroidal mhd equilibria, Computer Physics Communications 97 (1996) 219 – 260. doi:https://doi.org/10.1016/0010-4655(96)00046-X.

[65] A. Biancalani, A. Bottino, P. Lauber, D. Zarzoso, Numerical validation of the electromagnetic gyrokinetic code NEMORB on global axisymmetric modes, Nuclear Fusion 54 (2014) 104004. doi:10.1088/0029-5515/54/10/104004.

[66] S. Jolliet, Gyrokinetic Particle-In-Cell Global Simulations of Ion-Temperature-Gradient and Collisionless-Trapped-Electron-Mode Turbulence in tokamaks,

Phd thesis, Ecole Polytechnique Fédérale de Lausanne, Switzerland. Thesis number 4684., 2010. doi:10.5075/epfl-thesis-4326.

[67] F. Zonca, L. Chen, R. A. Santoro, Kinetic theory of low-frequency alfvén modes in tokamaks, Plasma Physics and Controlled Fusion 38 (1996) 2011–2028. doi:10.1088/0741-3335/38/11/011.

[68] P. H. Rutherford, E. A. Frieman, Drift instabilities in general magnetic field configurations, The Physics of Fluids 11 (1968) 569–585. doi:10.1063/1.1691954.

[69] T. M. Antonsen, B. Lane, Kinetic equations for low frequency instabilities in inhomogeneous plasmas, The Physics of Fluids 23 (1980) 1205–1214. doi:10.1063/1.863121.

[70] P. J. Catto, W. M. Tang, D. E. Baldwin, Generalized gyrokinetics, Plasma Physics 23 (1981) 639–650. doi:10.1088/0032-1028/23/7/005.

[71] E. A. Frieman, L. Chen, Nonlinear gyrokinetic equations for low-frequency electromagnetic waves in general plasma equilibria, The Physics of Fluids 25 (1982) 502–508. doi:10.1063/1.863762.

[72] J. W. Connor, R. J. Hastie, J. B. Taylor, High mode number stability of an axisymmetric toroidal plasma, Proceedings of the Royal Society of London. Series A, Mathematical and Physical Sciences 365 (1979) 1–17.

[73] R. A. Cairns, Plasma Physics, p. 104, Dordrecht Springer Netherlands, 1985. URL: http://dx.doi.org/10.1007/978-94-010-9655-3?nosfx=y.

[74] H. Sugama, T.-H. Watanabe, Collisionless damping of geodesic acoustic modes, Journal of Plasma Physics 72 (2006) 825–828. doi:10.1017/S0022377806004958.

[75] W. Lee, Gyrokinetic particle simulation model, Journal of Computational Physics 72 (1987) 243 – 269. doi:https://doi.org/10.1016/0021-9991(87)90080-5.

[76] R. Singh, Ö. D. Gürcan, Geodesic acoustic modes with poloidal mode couplings ad infinitum, Physics of Plasmas 24 (2017) 022507. doi:10.1063/1.4976116.

[77] P. L. Bhatnagar, E. P. Gross, M. Krook, A model for collision processes in gases. i. small amplitude processes in charged and neutral one-component systems, Phys. Rev. 94 (1954) 511–525. doi:10.1103/PhysRev.94.511.

[78] J. D. Huba, NRL PLASMA FORMULARY Supported by The Office of Naval Research, Naval Research Laboratory, Washington, DC, 2013. URL: http://wwwppd.nrl.navy.mil/nrlformulary/.

[79] M. Sasaki, K. Itoh, A. Ejiri, Y. Takase, Radial eigenmodes of geodesic acoustic modes, Contributions to Plasma Physics 48 (2008) 68–72. doi:10.1002/ctpp.200810011.

[80] V. I. Ilgisonis, I. V. Khalzov, V. P. Lakhin, A. I. Smolyakov, E. A. Sorokina, Global geodesic acoustic mode in a tokamak with positive magnetic shear and a monotonic temperature profile, Plasma Physics and Controlled Fusion 56 (2014) 035001. doi:10.1088/0741-3335/56/3/035001.

[81] I. Gertsbakh, Measurement Theory for Engineers, p. 20, Springer-Verlag Berlin Heidelberg 2003, 2003. URL: http://dx.doi.org/10.1007/978-3-662-08583-7.

[82] W. H. Press, S. A. Teukolsky, W. T. Vetterling, B. P. Flannery, Numerical Recipes 3rd Edition: The Art of Scientific Computing, Cambridge University Press, 2007.

[83] T. Ido, M. Osakabe, A. Shimizu, T. Watari, M. Nishiura, K. Toi, K. Ogawa, K. Itoh, I. Yamada, R. Yasuhara, Y. Yoshimura, S. Kato, LHD Experiment Group, Identification of the energetic-particle driven GAM in the LHD, Nuclear Fusion 55 (2015) 083024. doi:10.1088/0029-5515/55/8/083024.

[84] M. Osakabe, T. Ido, K. Ogawa, A. Shimizu, M. Yokoyama, R. Seki, C. Suzuki, M. Isobe, K. Toi, D. A. Spong, K. Nagaoka, Y. Takeiri, H. Igami, T. Seki, K. Nagasaki, LHD experiment group, Indication of bulk-ion heating by energetic particle driven geodesic acoustic modes on lhd, in: 25th IAEA fusion energy conference, 2014. URL: https://inis.iaea.org/search/search.aspx?orig_q=RN:47070985.

[85] F. Jenko, W. Dorland, M. Kotschenreuther, B. N. Rogers, Electron temperature gradient driven turbulence, Phys. Plasmas 7 (2000) 1904–1910. doi:10.1063/1.874014.

[86] P. Lauber, Aug test case description (2015). URL: http://www2.ipp.mpg.de/~pwl/NLED_AUG/data.html.

[87] L. Horváth, G. Papp, P. Lauber, G. Por, A. Gude, V. Igochine, B. Geiger, M. Maraschek, L. Guimarais, V. Nikolaeva, G. Pokol, The ASDEX Upgrade Team, Experimental investigation of the radial structure of energetic particle driven modes, Nuclear Fusion 56 (2016) 112003. doi:10.1088/0029-5515/56/11/112003.

[88] A. Di Siena, A. Biancalani, T. Görler, H. Doerk, I. Novikau, P. Lauber, A. Bottino, E. Poli, The ASDEX Upgrade Team, Effect of elongation on energetic particle-induced geodesic acoustic mode, Nucl. Fusion 58 (2018) 106014. doi:10.1088/1741-4326/aad51d.

[89] Y. Chen, S. Parker, Gyrokinetic turbulence simulations with kinetic electrons, Physics of Plasmas 8 (2001) 2095–2100. doi:10.1063/1.1351828.

[90] A. Mishchenko, R. Hatzky, A. Koenies, Conventional f-particle simulations of electromagnetic perturbations with finite elements, Physics of Plasmas 11 (2004) 5480–5486. doi:10.1063/1.1812275.

[91] A. Di Siena, T. Görler, H. Doerk, E. Poli, R. Bilato, Fast-ion stabilization of tokamak plasma turbulence, Nucl. Fusion 58 (2018) 054002. doi:10.1088/1741-4326/aaaf26.

[92] I. Novikau, A. Biancalani, A. Bottino, P. Lauber, E. Poli, P. Manz, G. D. Conway, A. Di Siena, N. Ohana, E. Lanti, L. Villard, ASDEX Upgrade Team, Nonlinear dynamics of energetic-particle driven geodesic acoustic modes in ASDEX Upgrade, Physics of Plasmas 27 (2020) 042512. doi:10.1063/1.5142802.

[93] M. Sasaki, K. Itoh, S.-I. Itoh, Energy channeling from energetic particles to bulk ions via beam-driven geodesic acoustic modes—GAM channeling, Plasma Physics and Controlled Fusion 53 (2011) 085017. doi:10.1088/0741-3335/53/8/085017.

[94] K. Toi, K. Ogawa, T. Ido, S. Morito, S. Ohdachi, N.A. Pablant, K. Tanaka, H. Funaba, T. Oishi, M. Osakabe, A. Shmizu, H. Tsuchiya, K.Y. Watanabe, LHD Experiment Group, Observation of non-collisional bulk ion heating by energetic ion driven geodesic acoustic modes in lhd, in: Proc. 16th IAEA Technical Meeting on Energetic Particles in Magnetic Confinement Systems — Theory of Plasma Instabilities, Shizuoka, Japan, 2019. URL: https://nucleus.iaea.org/sites/fusionportal/Shared%20Documents/EPPI%202019%20Material.pdf.

[95] H. Wang, Y. Todo, M. Oasakabe, T. Ido, Y. Suzuki, Simulation of energetic particle driven geodesic acoustic modes and the energy channeling in the large helical device plasmas, Nuclear Fusion 59 (2019) 096041. doi:10.1088/1741-4326/ab26e5.

[96] D. Zarzoso, P. Migliano, V. Grandgirard, G. Latu, C. Passeron, Nonlinear interaction between energetic particles and turbulence in gyro-kinetic simulations and impact on turbulence properties, Nuclear Fusion 57 (2017) 072011. doi:10.1088/1741-4326/aa7351.

[97] M. Sasaki, K. Itoh, K. Hallatschek, N. Kasuya, M. Lesur, Y. Kosuga, S.-I. Itoh, Enhancement and suppression of turbulence by energetic-particle-driven geodesic acoustic modes, Scientific Reports 7 (2017) 16767. doi:10.1038/s41598-017-17011-y.

[98] Z. Qiu, I. Chavdarovski, A. Biancalani, J. Cao, On zero frequency zonal flow and second harmonic generation by finite amplitude energetic particle induced geodesic acoustic mode, Physics of Plasmas 24 (2017) 072509. doi:10.1063/1.4993053.

[99] L. Chen, Z. Qiu, F. Zonca, Short wavelength geodesic acoustic mode excitation by energetic particles, Physics of Plasmas 25 (2018) 014505. doi:10.1063/1.5003142.

[100] A. Biancalani, I. Chavdarovski, Z. Qiu, A. Bottino, D. Del Sarto, A. Ghizzo, Ö. D. Gürcan, P. Morel, I. Novikau, Saturation of energetic-particle-driven geodesic acoustic modes due to wave–particle nonlinearity, Journal of Plasma Physics 83 (2017) 725830602. doi:10.1017/S0022377817000976.

[101] A. Biancalani, N. Carlevaro, A. Bottino, G. Montani, Z. Qiu, Nonlinear velocity redistribution caused by energetic-particle-driven geodesic acoustic modes, mapped with the beam-plasma system, Journal of Plasma Physics 84 (2018) 725840602. doi:10.1017/S002237781800123X.

[102] D. Zarzoso, D. del Castillo-Negrete, D. Escande, Y. Sarazin, X. Garbet, V. Grandgirard, C. Passeron, G. Latu, S. Benkadda, Particle transport due to energetic-particle-driven geodesic acoustic modes, Nuclear Fusion 58 (2018) 106030. doi:10.1088/1741-4326/aad785.

[103] F. Vannini, A. Biancalani, A. Bottino, T. Hayward-Schneider, P. Lauber, A. Mishchenko, I. Novikau, E. Poli, the ASDEX Upgrade team, Gyrokinetic investigation of the damping channels of alfvén modes in asdex upgrade, Physics of Plasmas 27 (2020) 042501. doi:10.1063/1.5134979.

[104] P. Lauber, B. Geiger, G. Papp, G. Por, L. Guimarais, P.ZS. Poloskei, V. Igochine, M. Maraschek, G. Pokol, T. Hayward-Schneider, Z. Lu, X. Wang, A. Bottino, F. Palermo, I. Novikau, A. Biancalani, G. Conway, the ASDEX UPGRADE team, the EUROFUSION enabling research 'NAT' and 'NLED' teams, Strongly non-linear energetic particle dynamics in asdex upgrade scenarios with core impurity accumulation, in: Proc. 27th IAEA Fusion Energy Conference - IAEA, Gandhinagar, India, 2018. URL: https://conferences.iaea.org/indico/event/151/papers/6094/files/5080-IAEA_proceedings_Lauber_v3.pdf.

[105] J.-B. Girardo, D. Zarzoso, R. Dumont, X. Garbet, Y. Sarazin, S. Sharapov, Relation between energetic and standard geodesic acoustic modes, Physics of Plasmas 21 (2014) 092507. doi:10.1063/1.4895479.

[106] R. S. Hemsworth, D. Boilson, P. Blatchford, M. D. Palma, G. Chitarin, H. P. L. de Esch, F. Geli, M. Dremel, J. Graceffa, D. Marcuzzi, G. Serianni, D. Shah, M. Singh, M. Urbani, P. Zaccaria, Overview of the design of the ITER heating neutral beam injectors, New Journal of Physics 19 (2017) 025005. doi:10.1088/1367-2630/19/2/025005.

[107] T. H. Stix, Heating of toroidal plasmas by neutral injection, Plasma Physics 14 (1972) 367–384. doi:10.1088/0032-1028/14/4/002.

[108] K. Itoh, S.-I. Itoh, P. H. Diamond, A. Fujisawa, M. Yagi, T. Watari, Y. Nagashima, A. Fukuyama, Geodesic acoustic eigenmodes, Plasma and Fusion Research 1 (2006) 037–037. doi:10.1585/pfr.1.037.

[109] C. A. de Meijere, S. Coda, Z. Huang, L. Vermare, T. Vernay, V. Vuille, S. Brunner, J. Dominski, P. Hennequin, A. Krämer-Flecken, G. Merlo, L. Porte, L. Villard, Complete multi-field characterization of the geodesic acoustic mode in the TCV tokamak, Plasma Physics and Controlled Fusion 56 (2014) 072001. doi:10.1088/0741-3335/56/7/072001.

[110] Z. Huang, S. Coda, G. Merlo, S. Brunner, L. Villard, B. Labit, C. Theiler, the TCV team, Experimental observations of modes with geodesic acoustic

character from the core to the edge in the TCV tokamak, Plasma Physics and Controlled Fusion 60 (2018) 034007. doi:10.1088/1361-6587/aaa71d.

[111] V. I. Ilgisonis, L. V. Konoval'tseva, V. P. Lakhin, E. A. Sorokina, Analytical solutions for global geodesic acoustic modes in tokamak plasmas, Plasma Physics Reports 40 (2014) 843–854. doi:10.1134/S1063780X14110038.

[112] E. Lanti, Global Flux-Driven Simulations of Ion Temperature-Gradient and Trapped-Electron Modes Driven Turbulence With an Improved Multithreaded Gyrokinetic PIC Code, Phd thesis, Ecole Polytechnique Fédérale de Lausanne, Switzerland. Thesis number 9575., 2019. doi:10.5075/epfl-thesis-9575.

[113] N. Ohana, Using an antenna as a tool for studying microturbulence and zonal structures in tokamaks with a global gyrokinetic gpu-enabled particle-in-cell code (2020) 150. doi:10.5075/epfl-thesis-10127.

[114] N. Ohana, L. Villard, E. Lanti, S. Brunner, B. F. McMillan, N. Tronko, A. Bottino, A. Biancalani, I. Novikau, A. Mishchenko, Mode excitation by an antenna in global gyrokinetic simulations, Journal of Physics: Conference Series 1125 (2018) 012017. doi:10.1088/1742-6596/1125/1/012017.

[115] T. C. Li, G. G. Howes, K. G. Klein, J. M. TenBarge, Energy dissipation and landau damping in two- and three- dimensional plasma turbulence, The Astrophysical Journal 832 (2016) L24. doi:10.3847/2041-8205/832/2/124.

[116] S. Du, F. Guo, G. P. Zank, X. Li, A. Stanier, Plasma energization in colliding magnetic flux ropes, The Astrophysical Journal 867 (2018) 16. doi:10.3847/1538-4357/aae30e.

[117] F. W. King, Hilbert Transforms, Vol. 2, p. 465, Cambridge Cambridge University Press, 2009, 2009. URL: https://doi.org/10.1017/CBO9780511735271.

Acknowledgement

I would like to express my acknowledgements to those who have helped me during the four years of my PhD studies. First of all, I would like to thank my supervisors, Alessandro Biancalani and Emanuele Poli, for their help, for encouraging me and having always been supportive. I am thankful to Alessandro for guiding my scientific work and for giving me answers, no matter what the questions were. He has always been available for advice and consultation regardless of his workload. Alessandro and Emanuele have been following the progress of my work and allowed me to extend my knowledge in different domains of plasma physics. I am extremely grateful to Emanuele for great assistance while I was writing my thesis, for his corrections and suggestions that have significantly improved the quality of my thesis, and for proof-reading of every section of this work. I am also deeply indebted to Alberto Bottino for his particular help in work with the code ORB5, and our long discussions of the gyrokinetic theory. I want to express my gratitude to Natalia Tronko, whose lectures significantly improved my understanding of the gyrokinetics. Many thanks to Peter Manz, Garrard Conway and Philipp Lauber for their collaboration and comments that made my thesis more informative and readable, and to Alessandro Di Siena from the GENE group for providing me data for inter-code benchmarks, and for our every week group meetings during several months.

I also acknowledge the collaboration with Dr. Özgür Gürcan and Dr. Pierre Morel at the beginning of my thesis. They helped me to visit Paris and to prepare material for my first paper. I want to express my particular gratitude to Prof. Dr. Laurent Villard and his group in Lausanne, especially, to Noé Ohana and Emmanuel Lanti, for the opportunity to visit Swiss Plasma Center and for our close collaboration that had a significant impact on my work. Also, I am very thankful to Dr. Daniele Del Sarto and Dr. Etienne Gravier. They recommended me this PhD position and helped me to get in contact with Alessandro Biancalani.

I warmly thank all my office mates and young scientists with whom I had a great pleasure to work together: Karl Stimmel and Maurice Maurer for discussion of our scientific (sometimes crazy) ideas, and Maurice Maurer deserves special thanks for

proofreading of my abstract; Aleksander Mustonen, Wladimir Zholobenko and Jonas Graw for our conversations about social and scientific events; Paul Crandall and Francesco Vannini for their countless jokes that helped to keep a relaxed atmosphere in our office; Karen Pommois, Nathan de Oliveira and Mathias Bösl for our evening meetings in our attempt to understand gyrokinetics; Thomas Hayward-Schneider for helping me with ORB5 and numerics. I have really learned a lot from all of you. I am also grateful to Julia Anthea Gessner and Thomas Body for our bike trip to Nürnberg and for waiting for me every 20 kilometres. This little journey showed me how beautiful the area around Munich is.

I wish to thank also my flatmates Lisa, Benno and Nick for always been nice to me, for our rare (which is my fault) evenings where we were discussing everything from local social and political events to promising ideas in artificial intelligence. Moreover, I would like to acknowledge Lisa and Benno for proofreading of my German translation of the thesis abstract.

Finally, I am deeply thankful to my parents and grandparents for their full support, for always encouraging and motivating me throughout all these years. If I manage to accomplish whatever, I owe it to them.

Declaration

I declare that the work presented in this thesis is my own except where stated otherwise, and was carried out at the Max Planck Institute of Plasma Physics in Garching near Munich under the supervision of Prof. Dr. Emanuele Poli and Dr. Alessandro Biancalani. Parts of the work reported in this thesis have been published in peer reviewed journals, as listed below:

1. I. Novikau, A. Biancalani, A. Bottino, G. D. Conway, Ö. D. Gürcan, P. Manz, P. Morel, E. Poli, A. Di Siena, ASDEX Upgrade Team, Linear gyrokinetic investigation of the geodesic acoustic modes in realistic tokamak configurations, Physics of Plasmas **24**, 12 (2017).

2. I. Novikau, A. Biancalani, A. Bottino, A. Di Siena, Ph. Lauber, E. Poli, E. Lanti, L. Villard, N. Ohana, S. Briguglio, Implementation of energy transfer technique in ORB5 to study collisionless wave-particle interactions in phase-space, Computer Physics Communications 107032 (2019).

3. I. Novikau, A. Biancalani, A. Bottino, Ph. Lauber, E. Poli, P. Manz, G. D. Conway, A. Di Siena, N. Ohana, E. Lanti, L. Villard, and ASDEX Upgrade Team, Nonlinear dynamics of energetic-particle driven geodesic acoustic modes in ASDEX Upgrade, Physics of Plasmas **27**, 042512 (2020).

Publication 1 in the above list is the basis of Chapter 4 of this thesis. Publication 2 is the basis of Chapters 5 and 6. Publication 3 is the basis of Chapter 7.

List of publications

Publications in peer-reviewed journals:

1. I. Novikau, A. Biancalani, A. Bottino, G. D. Conway, Ö. D. Gürcan, P. Manz, P. Morel, E. Poli, A. Di Siena, ASDEX Upgrade Team, Linear gyrokinetic investigation of the geodesic acoustic modes in realistic tokamak configurations, Physics of Plasmas **24**, 12 (2017).

2. I. Novikau, A. Biancalani, A. Bottino, A. Di Siena, Ph. Lauber, E. Poli, E. Lanti, L. Villard, N. Ohana, S. Briguglio, Implementation of energy transfer technique in ORB5 to study collisionless wave-particle interactions in phase-space, Computer Physics Communications 107032 (2019).

3. I. Novikau, A. Biancalani, A. Bottino, Ph. Lauber, E. Poli, P. Manz, G. D. Conway, A. Di Siena, N. Ohana, E. Lanti, L. Villard, and ASDEX Upgrade Team, Nonlinear dynamics of energetic-particle driven geodesic acoustic modes in ASDEX Upgrade, Physics of Plasmas **27**, 042512 (2020).

4. A. Biancalani, A. Bottino, C. Ehrlacher, V. Grandgirard, G. Merlo, I. Novikau, Z. Qiu, E. Sonnendrücker, X. Garbet, T. Görler, S. Leerink, F. Palermo, D. Zarzoso, Cross-code gyrokinetic verification and benchmark on the linear collisionless dynamics of the geodesic acoustic mode, Physics of Plasmas **24**, 062512 (2017).

5. A. Biancalani, I. Chavdarovski, Z. Qiu, A. Bottino, D. Del Sarto, A. Ghizzo, Ö. D. Gürcan, P. Morel, I. Novikau, Saturation of energetic-particle-driven geodesic acoustic modes due to wave–particle nonlinearity, Journal of Plasma Physics **83**, 725830602 (2017).

6. N. Ohana, L. Villard, E. Lanti, S. Brunner, B. F. McMillan, N. Tronko, A. Bottino, A. Biancalani, I. Novikau and A. Mishchenko, Mode excitation by an antenna in global gyrokinetic simulations, Journal of Physics: Conference Series **1125**, 012017 (2018).

7. A. Di Siena, A. Biancalani, T. Görler, H. Doerk, I. Novikau, P. Lauber, A. Bottino, E. Poli and The ASDEX Upgrade Team, Effect of elongation on energetic particle-induced geodesic acoustic mode, Nuclear Fusion **58**, 106014 (2018).

8. V. Grandgirard, X. Garbet, Ch. Ehrlacher, A. Biancalani, A. Bottino, I. Novikau, Y. Asahi, E. Caschera, G. Dif-Pradalier, P. Donnel, Ph. Ghendrih, C. Gillot, G. Latu, Ch. Passeron, Y. Sarazin, D. Zarzoso, Linear collisionless dynamics of the GAM with kinetic electrons: Comparison simulations/theory, Physics of Plasmas **26**, 122304 (2019).

9. L. Villard, B. F. McMillan, E. Lanti, N. Ohana, A. Bottino, A. Biancalani, I. Novikau, S. Brunner, O. Sauter, N. Tronko and A. Mishchenko, Global turbulence features across marginality and non-local pedestal-core interactions, Plasma Physics and Controlled Fusion **61**, 034003 (2019).

10. E. Lanti, N. Ohana, N. Tronko, T. Hayward-Schneider, A. Bottino, B.F. McMillan, A. Mishchenko, A. Scheinberg, A. Biancalani, P. Angelino, S. Brunner, J. Dominski, P. Donnel, C. Gheller, R. Hatzky, A. Jocksch, S. Jolliet, Z.X. Lu, J.P. Martin Collar, I. Novikau, E. Sonnendrücker, T. Vernay, L. Villard, A global electromagnetic gyrokinetic code using the PIC approach in toroidal geometry, Computer Physics Communications **251**, 107072 (2020).

11. F. Vannini, A. Biancalani, A. Bottino, T. Hayward-Schneider, P. Lauber, A. Mishchenko, I. Novikau, E. Poli, and ASDEX Upgrade Team, Gyrokinetic investigation of the damping channels of Alfvén modes in ASDEX Upgrade, Physics of Plasmas **27**, 042501 (2020).

Invited talks and oral conference contributions:

1. I. Novikau, A. Biancalani, A. Bottino, P. Manz, G. D. Conway, A. Di Siena, Ph. Lauber, E. Poli, E. Lanti, L. Villard, N. Ohana, and ASDEX Upgrade Team, Linear and nonlinear dynamics of GAMs and EGAMs, DPG-Frühjahrstagung der Sektion Materie und Kosmos (SMuK), Munich (Germany), 2019 (oral presentation).

2. I. Novikau, A. Biancalani, A. Bottino, P. Manz, G. D. Conway, A. Di Siena, Ph. Lauber, E. Poli, E. Lanti, L. Villard, N. Ohana, and ASDEX Upgrade Team, Nonlinear dynamics of energetic-particle driven geodesic acoustic modes in ASDEX Upgrade, 3rd Asia-Pacific Conference on Plasma Physics (AAPPS-DPP), Hefei (China), 2019 (invited presentation).